University of Applied Sciences Wiener Neustadt
Faculty of Mechatronics and Microsystems Engineering

www.fhwn.ac.at

Research Paper

Dynamic Analysis of a Refiner-Rotating-Unit employing ADAMS Bearing AT with Test Stand Validation

Harald Ott

Author

October, 2011

Date

Research conducted at:

Wichita State University

Sponsored by:

AUSTRIAN MARSHALL PLAN FOUNDATION
VIENNA | AUSTRIA

Fachhochschule Wiener Neustadt
> Technische Studiengänge

Title of Research Paper:

Dynamic Analysis of a Refiner-Rotating-Unit employing ADAMS Bearing AT with Test Stand Validation

Submitted by: Harald Ott BSc.

Enrollment number: 0910275025

at the: **UAS Wiener Neustadt & Wichita State University**

Specialization: Mechatronics

Supervisor: DI(FH) Roman Eichinger

Wiener Neustadt: October, 2011

Affidavit

I hereby declare that,

I have written this paper myself, independently and without the aid of unfair or unauthorized resources. Whenever content has been taken directly or indirectly from other sources, this has been indicated and the source referenced.

Signature

Abstract:

This research paper presents a rotordynamic analysis of a refiner-rotating-unit, used in the paper and fiberboard industry. Due to the very stiff refiner rotor and the short bearing spacing of the rotating unit, the bearing dynamics has a significant influence on the critical speeds of the system. Previously, linear substitute stiffnesses were used for the modeling of the roller bearings and the computation of the systems' natural frequencies, which led to conflicting data results between simulation and measurement. By substituting the bearing system with this simplified modeling, the complex contact mechanics is generally modeled insufficiently and the bearing clearance as well as the nonlinear load distribution are not considered. In the scope of this paper the dynamic analysis and consequently the computation of critical speeds of an overhung refiner rotor is carried out under consideration of the bearing nonlinearities. Therefore a multibody simulation model of the machine, which considers the flexural characteristics of the refiner shaft, is built up in ADAMS and the newly developed roller bearing plug-in 'Bearing AT' is deployed. The obtained results are compared to analysis results of the model using linear stiffness and verified by a detailed test run on the refiner test stand of the Andritz AG.

Contents

1 Introduction

Studies on rotating machinery date back to the second half of the nineteenth century, when the increase of the operating speed made it necessary to include rotation into the analysis of the machines' dynamic behavior. Since then, steadily increasing requirements regarding power, speed and productivity have led to a variety of more or less complex rotating systems in almost every industry. Rotordynamics has become its own field of studies and is considered a special field within machine dynamics. Its studies are basically concerned with analysis of rotating structures as well as their interaction with their environment. These structures range from turbines and turbomachinery to pumps, fans, hard disks and refiners in the pulp and paper industry.

A rotating machine usually consists of several components, including rotor, bearings, support frame and drive systems, which are all influencing the dynamic behavior of the system. Traditional rotor dynamic research deals mainly with the stability and natural frequencies of such rotor-bearing systems. W. Rankine correctly states in his paper, "*On the centrifugal force on rotating shafts*", published on "*The Engineer*" in 1869 that a flexible rotating system has a speed, at which very large vibration amplitudes are encountered. In modern rotordynamic literature the common understanding is that when the rotational speed of a machine increases, the vibration amplitude often passes through maxima which are defined as critical speeds. These vibration maxima can be excited by the rotor's unbalance or other non-idealities in the rotor-bearing system. The non-idealities may also cause critical resonances that occur when the speed of rotation is a fraction of the natural frequency of the system. Resonances can influence the quality of the final product when they are within the operating speed range of a machine. Further, an operation in resonance condition can

lead to excessive wear or even irreparable damage. In order to study the natural frequencies of a rotor system it is necessary to take the entire dynamic system into consideration. In practice, this can be achieved by studying the physical machine through modal analysis or by the use of computer simulation. If the simulation approach is used, it must be assured that the simulation model is precise enough so that the non-idealities of the rotor and bearings as well as the coupling between these elements are captured correctly. The powerful application of the finite element analysis (FEA) has also deeply influenced the field of rotordynamics. Thus, specialized FEA codes are necessary which capture the gyroscopic effects. Nowadays, commercial FE-Software providers like ANSYS or NASTRAN have added rotordynamics to their tool. Their implemented numeric algorithms solve the linearized equations of motion of the rotor system. Although linearity is only an idealization of the actual behavior of any system, and real-world rotors always deviate, rotors can often be considered linear in their nominal conditions, at least if the displacements remain within the allowable limits in operation. Other components like bearings or dampers can have a significant nonlinear behavior. If they are neglected or linearized, the obtained results show an unsatisfactory harmonization in many cases.

A good example is the nonlinear stiffness characteristic of roller bearings, which is often approximated with substitute stiffness. If the rotor-bearing system is a combination of stiff refiner rotor and short bearing spacing, substantial displacements occur within the bearing when the shaft is bending. Hence, the system's dynamic behavior is strongly influenced by the bearing characteristic; specifically the bearing stiffnesses have a major impact on systems' natural frequencies. The strong abstraction of these highly nonlinear impacts with linear substitute stiffness causes simulation and measurement results to diverge.

The engineering department of the pulp and paper division of Andritz AG is currently facing this problem when designing high consistency (HC) refiners. HC refiners are machines rotating at speeds of 1500 rpm and above, used for reducing a variety of feedstocks to pulp or fiber in the paper and fiberboard industry. The material is refined between two sets of refiner plates, one fixed set and one set mounted on a rotating refiner disc. The rotating refiner disc is attached to a shaft and supported by roller bearings. The goal at Andritz AG is now to develop a computational method where the Refiner's natural frequencies and consequently the critical speeds of the machine can be confidently determined during the design phase.

1.1 Scope of Work

The goal of this paper is now to look at the dynamic analysis of a refiner-rotating unit, including the Andritz bearing concept for overhung rotors by combining a detailed rotor and bearing model in a new multibody simulation approach. Therefore an applicable simulation model of the refiner has to be generated in MSC/ADAMS using the newly developed roller bearing subroutine. The natural frequencies of the rotor-bearing system are calculated and compared with results generated by a FE-Simulation. Further, the simulation results should be also evaluated against the measurement results obtained by a refiner test run.

1.2 Outline of the Paper

The accomplishment of the described scope of work requires a broad understanding of rotordynamic effects and the available simulation techniques to compute them. Therefore the first part of the paper is aimed towards the dynamics of rotating machinery and the thereby occurring effects.

Currently, Andritz uses the finite element analysis to simulate the dynamic behavior of refiners. In order to compare the additional benefits of a nonlinear multibody simulation with the existing FE results, the differences in both approaches have to be analyzed by evaluating a simple rotor-bearing model and comparing it to an analytical solution. To do so, the theoretical backgrounds of both computation methods will be reviewed in chapter 3 before the actual assessment of the FEA and MBS with the analytical solution is carried out in chapter 4. In the course of comparing the results of the simple rotordynamic system, the effect of isotropic and anisotropic bearings stiffness will be also analyzed.

As mentioned in the introduction, the implementation of linear stiffnesses to substitute the dynamic behavior of rolling element bearings creates insufficient simulation results. Hence, the nonlinearities of roller bearings will be described in chapter 5, as well as the modeling approaches of roller bearing dynamics, especially the one of the newly developed roller bearing toolkit for ADAMS.

Simulation results have to be verified with testing results in order to justify their quality. Therefore, the techniques to measure vibrations on rotating machinery and the interpretation of the acquired data are addressed in chapter 6.

The actual computation and measuring of the refiner is carried out in chapter 7. All the previously described work is necessary to ensure a correct understanding of the applied concepts on the Andritz machinery.

2 Dynamics of Rotating Machinery

A multitude of books and papers are dedicated to describe methods for analyzing rotordynamic phenomena (e.g. [**1**], [**2**] & [**3**]). Most of them are focused on the calculation of critical speeds and stability regions, balance, vibration analysis and the steady state response due to unbalance excitation. The simplest way to study and analyze the flexural characteristics of a rotor-bearings system is by using the Laval-Jeffcott model, in the following referred to as Jeffcott rotor. It is a model of a flexible rotor consisting of a rigid disc mounted on an elastic, massless shaft and supported by two rigid bearings (Figure 2.1).

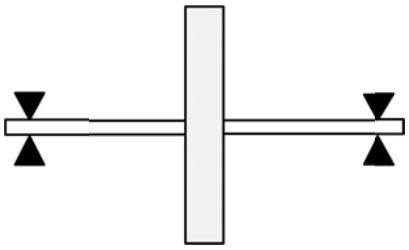

Figure 2.1: Jeffcott rotor

Based on this oversimplification of real-world rotors, the dynamic behavior of rotor systems such as mode shapes, the dependence of critical speeds on the rotational speed and gyroscopic effects can be analyzed. However, for a better approximation of a physical rotor, a modified rotor model with more degrees of freedom will be used in the following sections.

The goal of this chapter is primarily to introduce dynamic effects of rotating machinery from a less mathematical perspective. Instead a detailed analytical solution of an overhung rotor can be found in chapter 4. The used information and images are basically all retrieved from [**4**], [**5**] and [**6**].

2.1 Natural Frequencies and Mode Shapes

The fundamental basis to understand vibration analysis is the simple spring-mass-damper system shown in Figure 2.2. Such a system can be easily analyzed in the time domain as well as in the frequency domain.

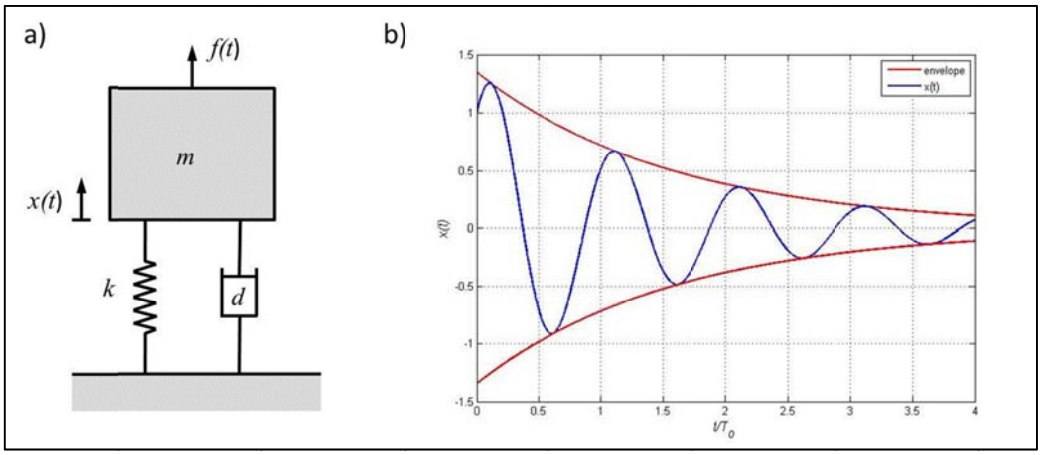

Figure 2.2: Spring-Mass-Damper System (a) with displacement vs. time diagram (b)

The equation of motion can be compiled by the examination of the system's equilibrium. It is assumed that a spring force according to $f_k = k\,x$ and a viscous damping force $f_d = k\,\dot{x}$ are acting on the rigid mass. Through the application of the dynamic law the differential equation of motion is:

$$m\,\ddot{x} + d\,\dot{x} + k\,x = f_{(t)} \tag{2.1}$$

This equation is often written in the standard format for damped vibrations

$$\ddot{x} + 2\zeta\omega_0\dot{x} + {\omega_0}^2 x = \frac{f_{(t)}}{m} \tag{2.2}$$

in which ω_0 is the free vibration frequency of the undamped system,

$$\omega_0 = \sqrt{\frac{k}{m}} \tag{2.3}$$

and ζ is the damping factor.

$$\zeta = \frac{\mathrm{d}}{2m\omega_0} \tag{2.4}$$

If damping is considered, the displacement versus time diagram is a sinusoidal function which decreases exponentially as shown in Figure 2.2b.

When *f(t)* in Figure 2.2a is a sinusoidal force with a constant amplitude and its frequency is slowly increased, the exciting frequency will pass the natural frequency of the system. Thus, the appearing peak response frequency is approximately the damped natural frequency (see Figure 2.3).

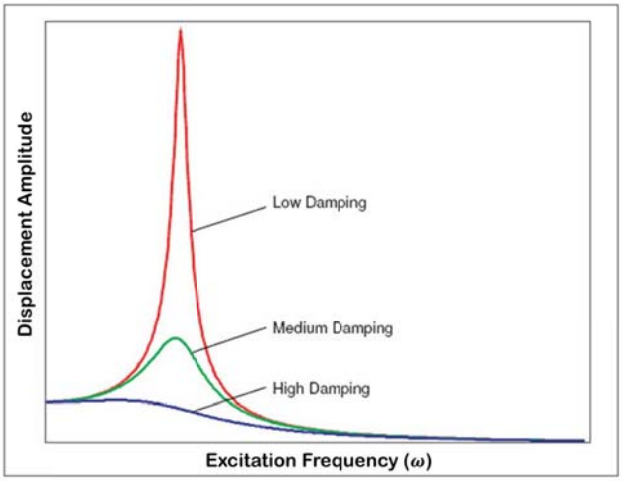

Figure 2.3: Frequency response of spring-mass-damper system[1]

Going from the single mass system to systems with more degrees of freedom, they basics do not change. For each DOF an own natural frequency and unique mode shape exist which are both still primarily related to mass and stiffness, with some changes due to damping. Consequently different parts of the structure are vibrating at different amplitudes and differing phases relative to one another.

Hence, a mass continuum can be treated as a system with an infinite number of single spring-mass-damper systems. Considering a simple beam structure supported by pin joints at each end, a closed-form solution to the natural frequencies and mode shapes is possible. The first three mode shapes are shown in Figure 2.4 and are basically of the same shape as those of a non-spinning Jeffcott rotor.

[1] [**4**], p. 11

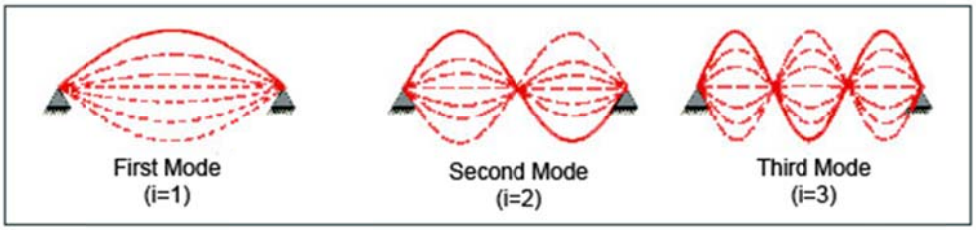

Figure 2.4: First three mode shapes of pinned-pinned beam[2]

2.2 Rotating Mode Shapes and Whirling

For the introduction of rotordynamic phenomena a simple rotor model (Figure 2.5) with a rigid central steel disc, a shaft with stiffness and mass and two bearings with isotropic stiffness is used. Isotropic stiffness means equal stiffness in horizontal and vertical direction.

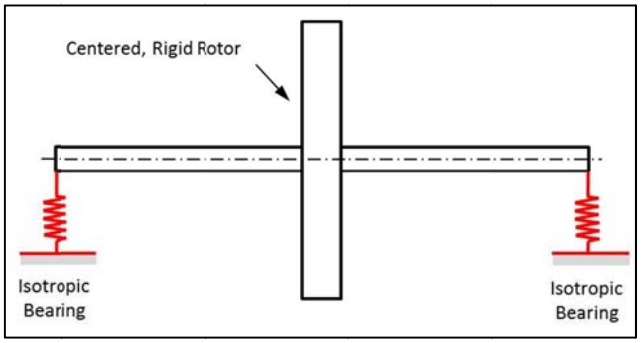

Figure 2.5: Basic rotor model[3]

At first the non-spinning rotor will be reviewed with three different degrees of bearing stiffness. The comparison in Figure 2.6 reflects the significant impact of the bearing stiffness on the mode shapes. Further, they are also influenced through the ratio of bearing stiffness to shaft stiffness. An increase in bearing stiffness or a decrease in shaft stiffness leads to higher bending.

[2] [**4**], p.11
[3] cf. ibid., p.11

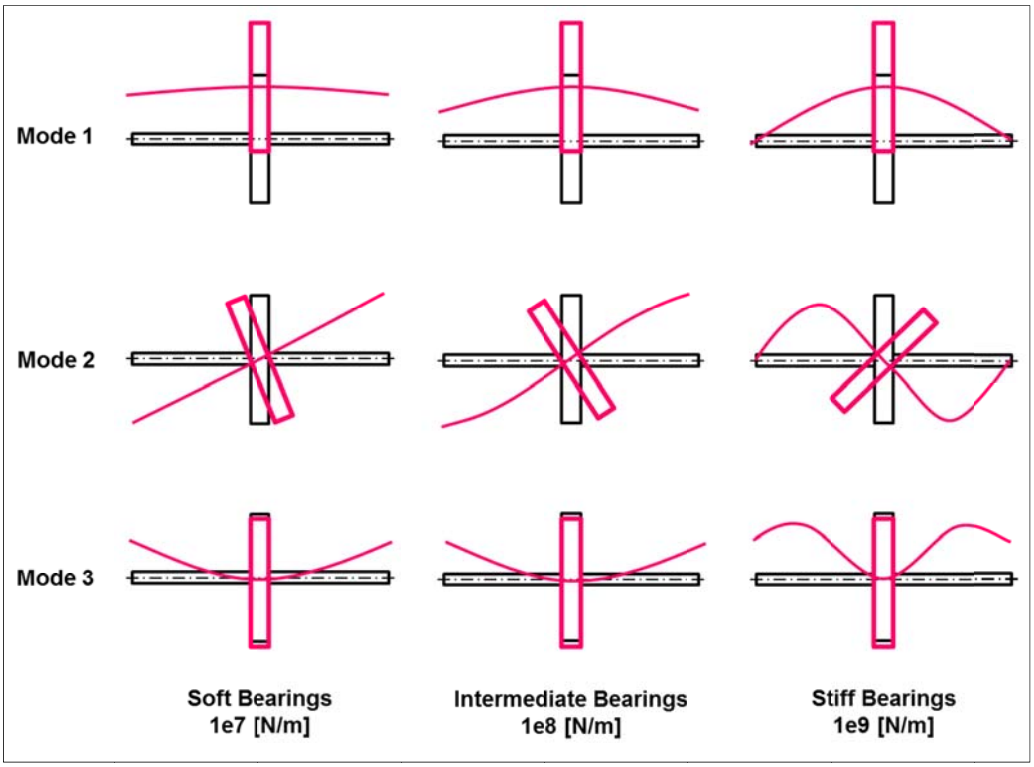

Figure 2.6: Mode shapes versus bearing stiffness, shaft not rotating[4]

Another interesting characteristic of the mode shapes is the movement of the centered disc. When oscillating in the first mode, the disc is translated without tilting, in the second it tilts without translation. This general characteristic repeats itself as the frequency increases. If the disc is moved off center, the motion is a mixture between tilting and translation.

Next, rotation is added to the rotor model. The resulting modes are similar to the nonrotating ones, but have now a circular motion rather than a planar. The mode shapes for the first vibration form related to bearing stiffness are displayed in Figure 2.7.

[4] cf. [**4**], p. 12

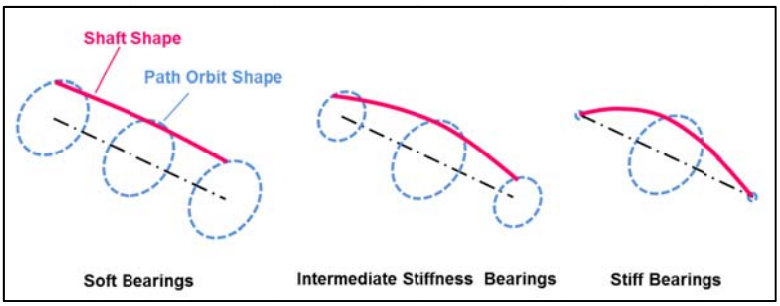

Figure 2.7: 1st mode shapes when shaft rotates[5]

For a better visualization of the spinning rotor's motion it is helpful to imagine a rope while skipping. Thereby the rope traces the outline of a bulging cylinder. If viewed from the side, the rope appears to be rocking up and down around the center.

In contrast to skipping, the rotor is spinning during the whirling motion. Generally two cases can be differentiated:

1. Whirling motion and shaft rotation occur in the same direction
   → "forward whirl" (FW)
2. Whirling motion and shaft rotation occur in the opposite direction
   → "backward whirl" (BW)

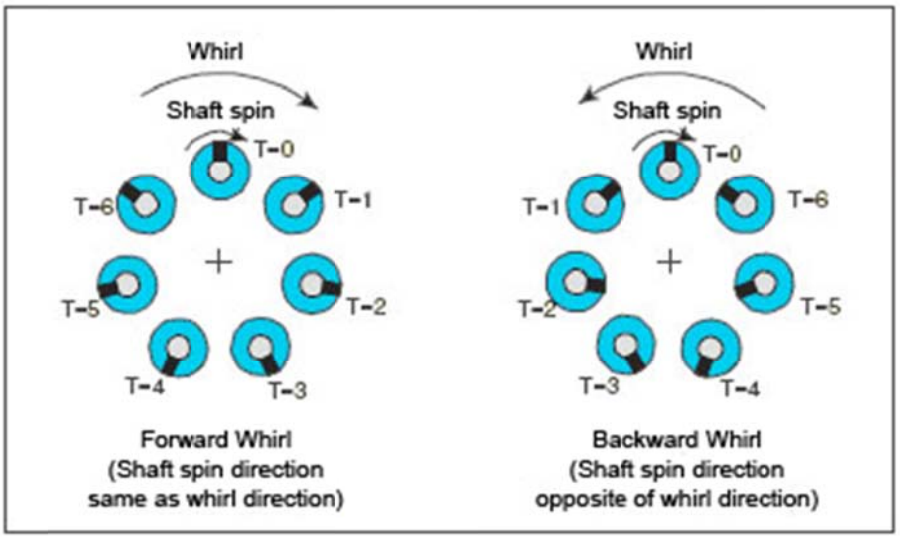

Figure 2.8: Forward- und Backward-Whirl[6]

[5] cf. [**4**], p. 12
[6] ibid., p. 12

Figure 2.8 indicates the rotor's cross section over the course of time for forward and backward whirl. Depending on the bearing stiffness, the excitation of both mode shapes can result from unbalance. To get an idea how the rotor speed effects the whirling motion of the first mode, the result of a modal analysis from standstill to high-speed is presented as damped natural frequency vs. speed plot (or Campbell Diagram) in Figure 2.9.

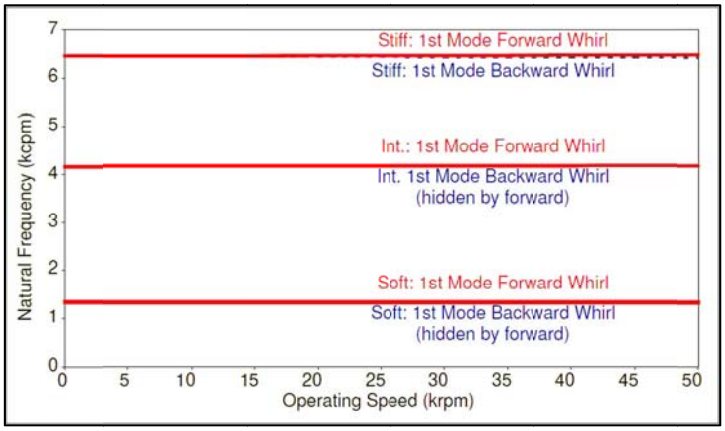

Figure 2.9: Effect of operating speed on 1st mode of Jeffcott and basic rotor (centered disc)[7]

It can be recognized that the rotor's speed has no significant influence on the natural frequencies of the first vibration mode.

After the detailed analysis of the first mode, the following section explores the influence of rotation on the 2nd mode. This vibration form is sometimes referred to as "conical" or "rocking" mode.

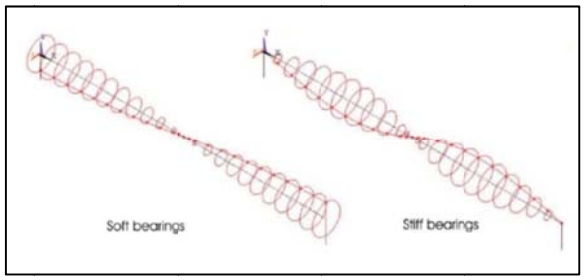

Figure 2.10: Second mode when shaft is rotating[8]

[7] [**4**], p. 12
[8] [**6**], p. 19

Reusing a modal analysis from standstill to high speed, Figure 2.11 shows a clear change of eigenfrequencies with increasing speed and the occurring forward and backward whirls.

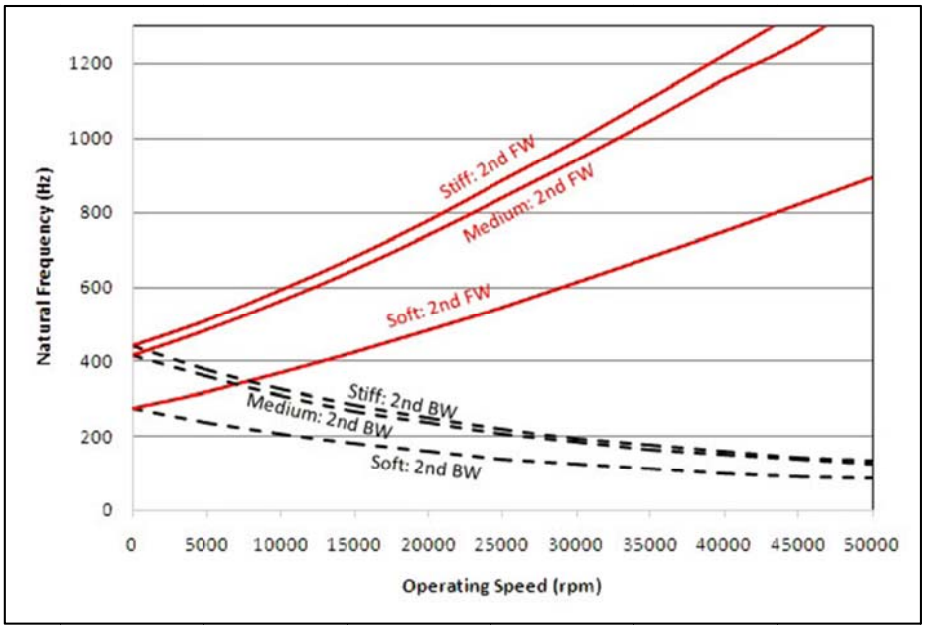

Figure 2.11: Effect of operating speed on 2nd mode[9]

The explanations for the strong change of natural frequencies over speed are gyroscopic effects that occur whenever the mode shape has an angular component.

Considering the forward whirl, these effects act through the increasing speed like a stiff spring on the disc and raise the natural frequency. The backward whirl causes a softening in return.

[9] [**6**], p. 20

2.3 Gyroscopic and Mass Effects

While the previous section explored the implications of gyroscopic effects on the rotor's eigenfrequencies, the upcoming chapter will address the impact on rotors with different disc alignment and different disc masses.

2.3.1 The symmetric Rotor

For a rotor with centered disc (Figure 2.12) the following conclusions can be drawn:

- An increased mass reduces the natural frequencies of the first mode.
- An increased mass doesn't change the second mode.
- A reduced moment of inertia doesn't change the first mode.
- A reduced moment of inertia increases the eigenfrequencies of the second mode and decreases the impact of the gyroscopic effect.

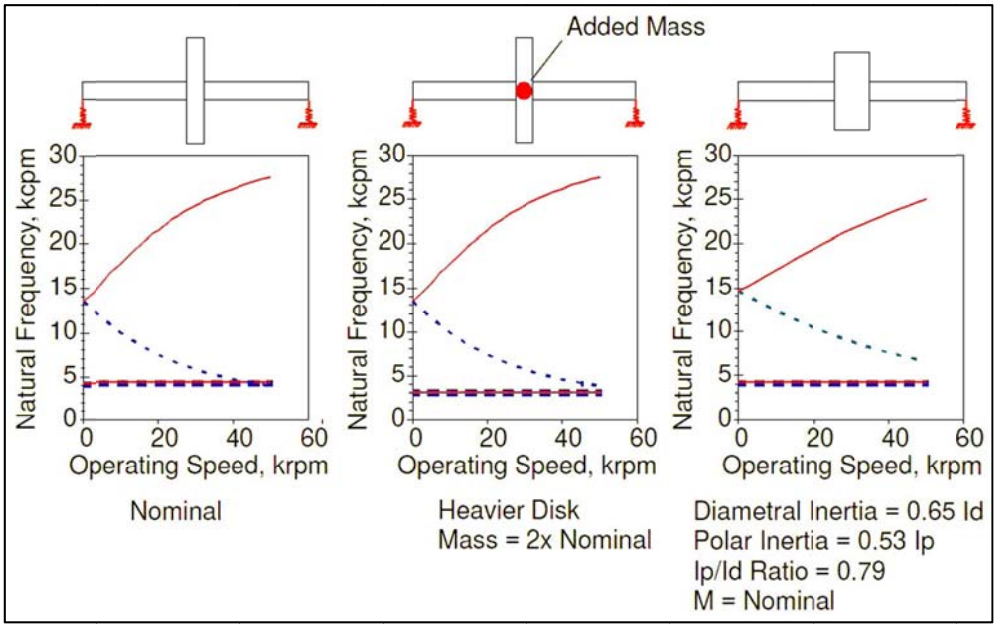

Figure 2.12: Comparison of different disc properties, center disc configuration[10]

[10] [**4**], p.13

2.3.2 Overhung Rotor

For the overhung configuration (Figure 2.13), the disc is moved to one end of the shaft and the bearing moves in exchanged towards the center. A comparison of the different disc configuration results in the below mentioned conclusions:

- An increased mass reduces the eigenfrequencies of the 1st and 2nd mode.
- A reduced moment of inertia increases the eigenfrequencies of both modes and decreases the impact of the gyroscopic effects.

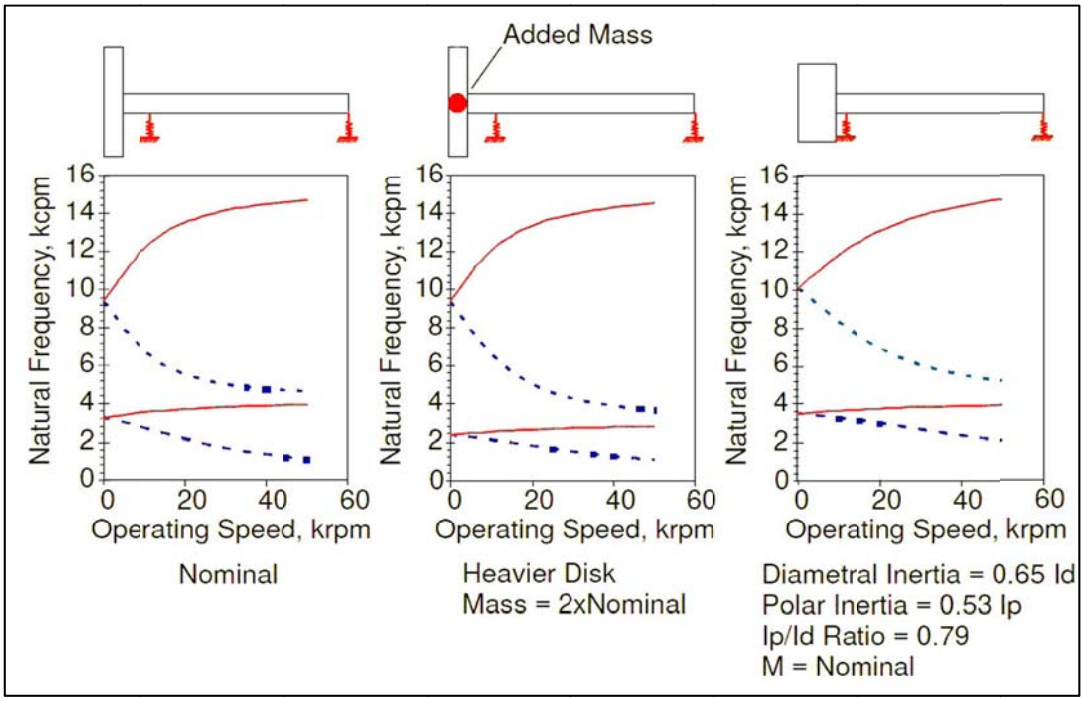

Figure 2.13: Comparison of different disc properties, overhung configuration[11]

[11] [**4**], p. 13

2.4 Orthogonal Anisotropic Bearings

Rotating machines with horizontal shafts generally have unequal bearing stiffness in vertical and horizontal direction due to the use of roller bearings and the layout of the supporting frame. Different bearing stiffness leads to varying natural frequencies in the particular directions and to a separation of the mode pairs (Figure 2.14 and Figure 2.15).

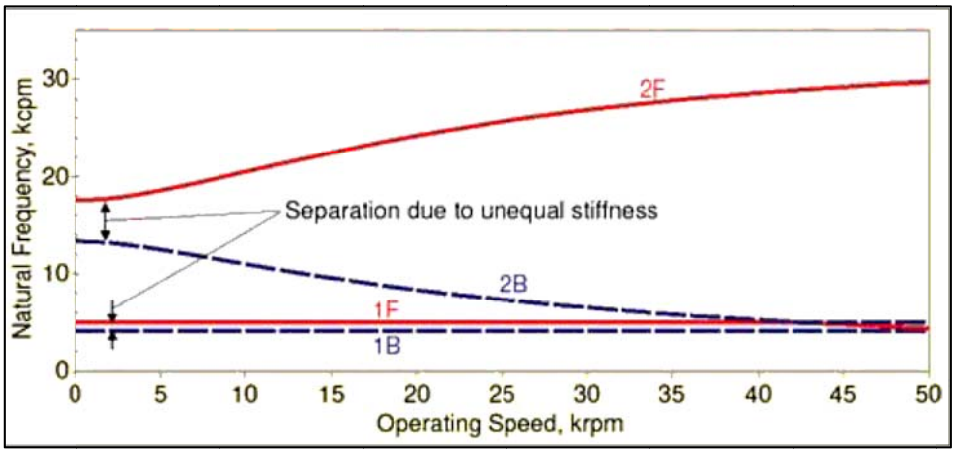

Figure 2.14: Natural frequencies vs. speed, basic model, vertical stiffness = 2x horizontal stiffness[12]

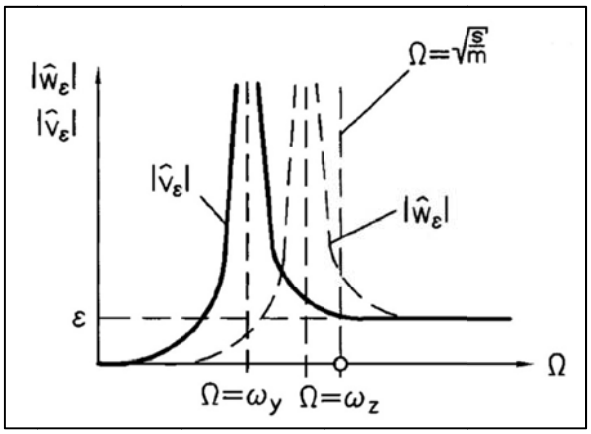

Figure 2.15: Unbalance Response for anisotropic bearings[13]

[12] [**4**], p. 15
[13] [**1**], p. 105

Furthermore the circular orbits will become elliptical through the anisotropic support and the yielding whirling motion is a superposition of forward and backward whirls. This means that forward and backward mode can no longer be considered as strictly separate and the mode shapes have forward as well as backward fractions. Rotordynamic theory often concludes that unbalance can only excite forward modes, but as the whirling is a superposition, also backward modes can become resonant.

Figure 2.16 shows the orbit motion and the whirling senses for different rotor speeds, in which ω_y and ω_z characterize the first two natural frequencies of the system, Ω is the rotational speed and η expresses the ratio of speed to eigenfrequency ω for isotropic bearing stiffness. In terms of critical speed is ω_y defining the horizontal critical speed and ω_z the vertical critical speed.

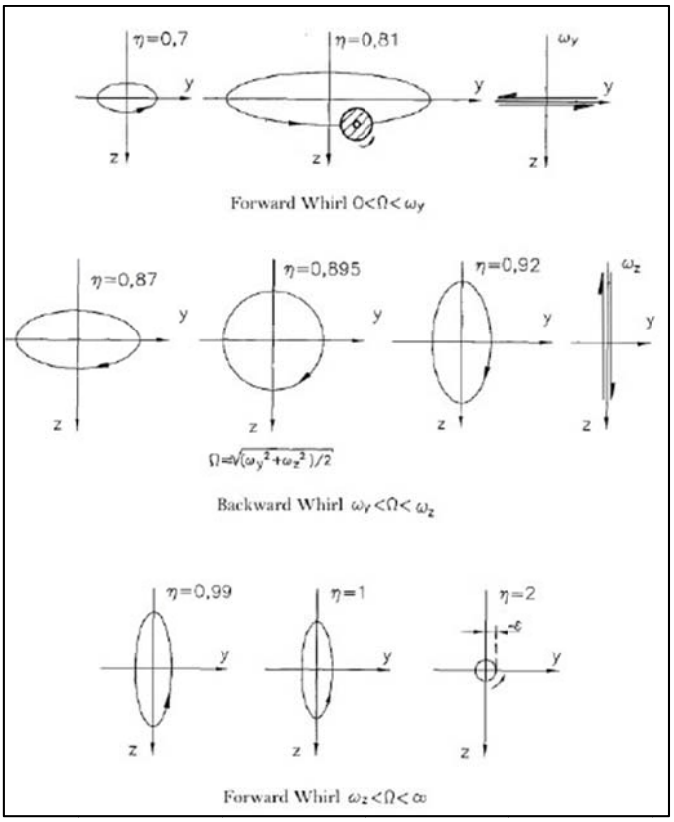

Figure 2.16: Forward and backward modes with orbit motion
$\omega = \sqrt{s/m}$, $\eta = \Omega/\omega$ ($\omega_y = 0.85\omega$; $\omega_z = 0.95\omega$)[14]

[14] [**1**], p. 107

2.5 Critical Speeds

When the phrase "critical speed" is applied, it usually refers to the speed at which a bending mode of the rotor is excited. As commonly defined, critical speeds occur through excitation of a systems natural frequency triggered by the shaft's unbalance. The obvious consequences are very large amplitudes, controlled only by the system damping. For the visual explanation in Figure 2.17 a simplified Campbell Diagram of an overhung rotor (compared to Figure 2.13) with isotropic bearings (no separation of FW and BW at *0 rpm*) will be used.

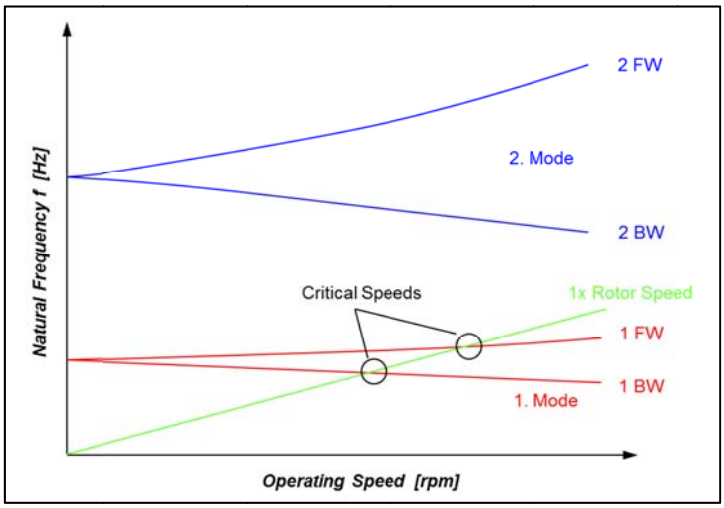

Figure 2.17: Campbell Diagram showing critical speeds

The displayed diagram shows the rotors' eigenfrequencies of the first and second mode with the distinct whirling motions. Assuming the rotor speed passes both natural frequencies of the first mode pair during run up from standstill to operating speed, its intersections with the natural frequencies are defined as critical speeds. In this manner the critical speeds could also be seen as "peak response" speeds.

Thus, the goal of machinery design is to avoid speeds which cause high vibration amplitudes. Most machine specifications require a minimum separation between operating speed and any critical speed.

3 Simulation of Dynamic Systems

Through the application of computational tools it has become possible to investigate the dynamics of complex mechanical systems. For the numeric simulation of those systems basically the finite element analysis (FEA) and the multibody simulation (MBS) have established themselves as effective ways to convert and solve real world problems with mathematical models.

3.1 Finite Element Analysis (FEA)

The finite element analysis is based on the principle of virtual work and represents a powerful technique for the calculation of boundary value problems [7]. The basic idea of the method is to divide an examined flexible structure into a finite number of small segments with established properties. Thus, the continuums' infinite number of degrees of freedom is reduced to a finite number of DOF on the connection points of the elements. Each small segment gets an applicable displacement formulation assigned, which has to meet the kinematic boundary conditions. The arising algebraic equations are then assembled to a global system of equations. The final result of the assembly process for linear elastostatic problems is the master stiffness equation

$$\mathbf{K}\,\mathbf{u} = \mathbf{f} \tag{3.1}$$

where $\mathbf{K}$ is the stiffness matrix, $\mathbf{u}$ the vector of node displacements and $\mathbf{f}$ is the vector of node forces. By imposing the displacement and force boundary conditions, the system is solved for the unknown node displacements.

3.1.1 Dynamic Analysis[15]

All parameters of the static analysis in the previous section are independent of time. This kind of analysis is also applied to quasi-static scenarios, where the state varies so slowly with time that inertial and damping effects can be ignored. When these effects cannot be neglected a dynamic analysis has to be performed.

The essence of the computation of dynamic problems caused by dynamic loads is the increasing importance of the node displacements. Embedding inertial and damping effects means including acceleration and velocity in the force balance statement and those are temporal derivatives of displacements.

The analysis of dynamic problems may be performed in the time domain or in the frequency domain. Whereby, the latter is limited in its application due to the modal transformation. It applies only to linear structural models, or to linearized fluctuations about an equilibrium state (i.e. small vibration amplitudes). The frequency domain is usually used to study vibrations. Solving dynamic FE models in the time domain requires much more computational effort than in the frequency domain. Therefore a frequency domain solution is preferred when the damping effect of the system is from lower significance. Either way the initial equation for the structural dynamic FEA based on Newton's second law is

$$\mathbf{M}\,\ddot{\mathbf{u}}_{(t)} + \mathbf{C}\,\dot{\mathbf{u}}_{(t)} + \mathbf{K}\,\mathbf{u}_{(t)} = \mathbf{f}_{(t)} \tag{3.2}$$

where $\mathbf{M}$, $\mathbf{C}$ and $\mathbf{K}$ are the mass, damping and stiffness matrices which are constant with time. Whereas, the unknown nodal displacements and rotations $\mathbf{u}_{(t)}$ vary with time. The underlying concept is again the principle of virtual displacements, which is

[15] cf. [**21**], chapter 30, p. 3ff.

also valid for structural dynamics. Through the time dependence of the system a discretization of the time is required.

If the second order differential algebraic equation (3.2) is solved with the FEA, the corresponding system of equation can get capacious. Unfortunately only a few methods for an efficient computation exist. These methods use either implicit or explicit time integration. Generally the continuous function of time has to be calculated for certain points of time what implicates a loss of information. Therefore requirements regarding stability, efficiency and accuracy have to be met.

One of the commonly used implicit integration procedures is the Newmark procedure which assumes that all system variables ($\mathbf{u}, \dot{\mathbf{u}}, \ddot{\mathbf{u}}$) are known for the starting point 0 and the value of these variables for discrete points of time after the time period Δt is searched for. In between those intervals the ability of a linear interpolation is assumed. The most important explicit time integration procedure is the Central Difference Method (CDM). It basically computes the equation 3.2 at the current time t and extrapolates it to $t+\Delta t$.

3.1.2 Modal Analysis[16]

Before performing a transient dynamic analysis in the time domain it is advantageous to run a modal analysis because a structure's vibration characteristics determine how it responds to any type of dynamic load. When computed in the frequency domain, the dynamic responses of the structure are defined as eigenmodes and eigenfrequencies.

[16] cf. [**20**], chapter 3

The modal analysis distinguishes between free and forced vibrations. As described in Chapter 2.1 there is no external force acting on the elastic structure when free vibration is analyzed. The response $\mathbf{u}_{(t)}$ is only determined by initial conditions.

For undamped free vibrations

$$\mathbf{M}\,\ddot{\mathbf{u}}_{(t)} + \mathbf{K}\,\mathbf{u}_{(t)} = \mathbf{0} \tag{3.3}$$

the general solution is obtained by using an exponential initial condition, which assumes harmonic motion:

$$\mathbf{u}_{(t)} = \mathbf{X}\,e^{j\omega t} \tag{3.4}$$

Here $\mathbf{X}$ is a time independent, complex column vector which has to be adjusted to the initial conditions. Replacing $\ddot{\mathbf{u}}_{(t)}$ in equation 3.3 with $-\omega^2\mathbf{X}\,e^{j\omega t}$ leads to

$$(-\omega^2\,\mathbf{M} + \mathbf{K})\,\mathbf{X}\,e^{j\omega t} = 0 \tag{3.5}$$

Because $\mathbf{X}$ cannot be a null vector and $e^{j\omega t} \neq 0$, this equation is an algebraic eigenvalue problem in ω. The eigenvalues $\lambda_i = \omega_i^2$ are the roots of the characteristic polynomial indexed by i:

$$det(-\omega^2\,\mathbf{M} + \mathbf{K}) = 0 \tag{3.6}$$

Each eigenfrequency ω_i has its corresponding eigenmode Ψ^i, which can be found by inserting the eigenfrequencies in equation 3.5. All eigenfrequencies are defined exactly for the eigenproblem, whereas the eigenmodes have to be found with an under-determined equation system, i.e. if the vector of eigenmodes $\mathbf{\Psi}^{(i)}$ fulfills the eigenproblem, also the multiples of $\mathbf{\Psi}^{(i)}$ do. The number N of resulting solutions indicates that a system with N degrees of freedom has also N solutions for the free vibration. Therefore, the resulting vibration response can be found by superposition of the N free vibrations,

$$u_{(t)} = \sum_{i=1}^{N} \alpha_i\,\mathbf{\Psi}^{(i)}\,e^{j\omega_i t}. \tag{3.7}$$

The second scenario which is of interest in practice is the forced vibration. The system is then subjected to a time dependent force $\mathbf{f}_{(t)}$. The response $\mathbf{u}_{(t)}$ is determined from the linear dynamics equation 3.2. Of particular interest in resonance studies is when $\mathbf{f}_{(t)}$ is periodic in time

$$\mathbf{f}_{(t)} = \mathbf{F}\, e^{j\omega t}. \tag{3.8}$$

Due to the periodicity of the force this kind of analysis is called harmonic analysis. It generates a response transfer function, i.e. for a specified load amplitude and location a response at another location is found over a specified frequency range. Hence, it also assumes periodic displacements $\mathbf{u}_{(t)} = \mathbf{X}\, e^{j\omega t}$ and if damping is not considered equation 3.5 for forced vibrations can be rewritten as

$$(-\omega^2\, \mathbf{M} + \mathbf{K})\, \mathbf{X}\, e^{j\omega t} = \mathbf{F}\, e^{j\omega t} \tag{3.9}$$

with $\mathbf{X}$ and $\mathbf{F}$ as complex vectors of amplitudes. The transfer function $\mathrm{H}_{(\omega)}$ is defined as the ratio of displacement to force

$$\mathrm{H}_{(\omega)} = \frac{\mathbf{X}}{\mathbf{F}} = (-\omega^2\, \mathbf{M} + \mathbf{K})^{-1} \tag{3.10}$$

and requires a matrix inversion for every eigenfrequency. Because this is a very inefficient and time consuming computation, a formulation based on modal segmentation is used. When a modal transformation is applied, the transformed mass and stiffness matrix will show a diagonal form.

$$\mathbf{\Psi}^{\mathbf{T}}\, \mathbf{M}\, \mathbf{\Psi} = \mathrm{diag}(m_i) \tag{3.11}$$

$$\mathbf{\Psi}^{\mathbf{T}}\, \mathbf{K}\, \mathbf{\Psi} = \mathrm{diag}(k_i) \tag{3.12}$$

Because the mode shape matrix is not exactly defined, it is possible to normalize the matrix of eigenvectors related to the mass matrix.

The resulting normalized matrix is defined as

$$\mathbf{\Phi} = \left[\Phi^{(1)}, \cdots, \Phi^{(N)}\right] \tag{3.13}$$

and complies the relationship

$$\mathbf{\Phi^T M\, \Phi = I} \tag{3.14}$$

as well as the equation

$$\mathbf{\Phi^T K\, \Phi} = \mathrm{diag}(\omega_i{}^2)\ . \tag{3.15}$$

The undamped equation of motion for forced vibration can be transformed to modal coordinates by using $\mathbf{u = \Phi\, q}$ resulting in

$$\mathbf{M\, \Phi\, \ddot{q} + K\, \Phi\, q = f}\ . \tag{3.16}$$

In order to make use of the orthogonal characteristics (3.14 and 3.15) the equation 3.16 has to be multiplied with $\mathbf{\Phi^T}$ from the left side

$$\mathbf{\Phi^T M\, \Phi\, \ddot{q} + \Phi^T K\, \Phi\, q = \Phi^T f}. \tag{3.17}$$

The consequential equation

$$\mathbf{\ddot{q} + \Omega\, q = f_q} \tag{3.18}$$

is totally decoupled and provides in its rows the independent modal equations of motion

$$\ddot{q}_i + \omega_i{}^2\, q_i = f_{q,i}\ . \tag{3.19}$$

These N independent equations can be solved with the methods of the simple spring-mass-damper system. Matrix $\mathbf{\Omega} = \mathrm{diag}(\omega_1{}^2, \cdots, \omega_N{}^2)$ contains the necessary eigenfrequencies and $\mathbf{f_q = \Phi^T\, f}$ is the vector of the modal forces. The external loads emerge through the projection of the load vector on the matrix of mode shapes $\mathbf{\Phi^T}$. If the external load can be divided in a constant distribution function $\mathbf{f_0}$ and a common time function $g(t)$ the modal load is

$$\mathbf{f_q = \Phi^T\, f_0}\ \ g(t) = \mathbf{\overline{f}}\ g(t)\,. \tag{3.20}$$

The components of the participation vector $\overline{\mathbf{f}}$ determine the excitation of the system, while the time function *g(t)* is responsible for the time course of the excitation.

In the harmonic analysis the computed modal displacements q are converted back into geometric displacements u (the system response to the loading). The actual dynamic response is obtained by the superposition of all individual modal responses.

3.1.3 Rotordynamic Analysis[17]

The initial equation for rotordynamic systems is again equation 3.2. The mass matrix **M** is a combination of the element matrices and single mass matrices. Hereby, the element mass matrices $\mathbf{M^B}$ contain the continuous distribution of mass over the particular shaft part. The diagonal mass matrix $\mathbf{M^S}$ includes the masses and inertias of the fitted discs. The total mass matrix is a positive definite matrix with speed independent elements.

$$\mathbf{M} = \mathbf{M^B} + \mathbf{M^S} \tag{3.21}$$

The matrix of the speed proportional forces **C** is composed of the damping matrix and the gyroscopic matrix:

$$\mathbf{C} = \mathbf{G}(\Omega_\mathrm{R}) + \mathbf{D}(\Omega_\mathrm{R}) \tag{3.22}$$

The matrix **G** considers the gyroscopic effect of the elements and is anisometric and speed dependent.

$$\mathbf{G} = \mathbf{G}(\Omega_\mathrm{R}) \qquad \text{with } g_{ij} = -g_{ij} \text{ and } g_{ii} = 0 \tag{3.23}$$

The damping matrix **D** would be positive definite for a system with viscous damping. Due to the rotor support, nonsymmetrical and speed dependent damping terms are added.

$$\mathbf{D} = \mathbf{D}(\Omega_\mathrm{R}) \qquad \text{with } d_{ij} \neq -d_{ij} \tag{3.24}$$

[17] cf. [**22**]

The stiffness matrix is assembled with the speed independent stiffness matrix $\mathbf{K^B}$ of the elements, as well as the speed dependent stress stiffening matrix $\mathbf{K^S}$ and the speed dependent bearing stiffness matrix $\mathbf{K^L}$. If the rigid body motions are suppressed, the stiffness matrix $\mathbf{K^B}$ is defined positive:

$$\mathbf{K} = \mathbf{K^B} + \mathbf{K^S}(\Omega_R) + \mathbf{K^L}(\Omega_R) \qquad \text{with } k_{ij}^B = k_{ji}^B \text{ and } k_{ij}^L \neq k_{ji}^L \tag{3.25}$$

For the rotor system the general dynamic system is generated using the described system matrices. The computation can be carried out in the time or frequency domain using the methods described in Chapter 3.1.1 and 3.1.2.

3.2 Multibody Simulation

The computation of multibody systems is very different to those of the FEA. While the FE-model is solved by predefined border conditions holding the system in a certain position, the multibody simulation codes are based on the principles of Eulerian and Lagrangian dynamics. Although there are several important approaches to solve those equations, this chapter will introduce the solution techniques implemented in the MSC/ADAMS Software. The following descriptions and derivations are basically based on [**8**] and [**9**].

In principle, a multibody system consists of a finite number of rigid or elastic bodies which are coupled through passive or active elements (Figure 3.1). At the same time kinematic constraints appear through supports, guides or joints. On all bodies external forces or moments can be applied. For the dynamic analysis of such a multibody system, the inertial forces, the constraining forces and any externally applied forces must be kept in equilibrium. This property provides the foundation for the equation of motion which is formulated in terms of expressions for the kinetic and potential energy of the mechanical system.

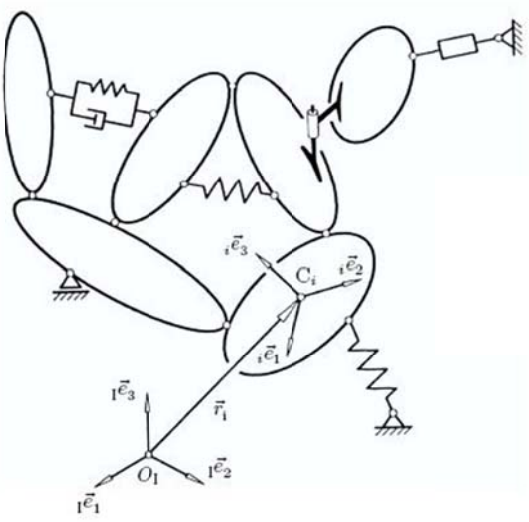

Figure 3.1: Multibody System

3.2.1 The Equations of Motion

For motion in space, the kinetic energy of a rigid body system is given by

$$K = \frac{1}{2}\sum_{i=1}^{N} m\, \dot{\mathbf{r}}_S^{(i)}\, \dot{\mathbf{r}}_S^{(i)} + \boldsymbol{\omega}^{(i)T}\, \boldsymbol{\Theta}_{Si}\, \boldsymbol{\omega}^{(i)} \tag{3.26}$$

where N is the number of bodies, $\boldsymbol{\Theta}_{Si}$ is the rotational inertia matrix around their centers of gravity, $\dot{\mathbf{r}}_S^{(i)}$ are the vectors of the translational center velocities and $\boldsymbol{\omega}^{(i)}$ are the vectors of rotational center velocities. Usually, some of the externally forces which are acting on the dynamic system (e.g. gravity) cause a potential energy V.

The difference between the kinetic and potential energy

$$L = K - V \tag{3.27}$$

is called the Lagrangian of the dynamical system. For multibody dynamics the Lagrangian becomes

$$L = \sum_{i=1}^{N} K^{(i)} - V^{(i)}. \tag{3.28}$$

Where $K^{(i)}$ and $V^{(i)}$ are the kinetic and potential energy for each of the N parts which comprise the system. In the following discussion, the derivation of the equations of motion in terms of the Lagrangian will be explained for the case *N=1*.

According to the laws of Lagrangian dynamics, the motion of a multibody system is governed by

$$\frac{d}{dt}\left(\frac{\partial L}{\partial \dot{\boldsymbol{\xi}}}\right) - \frac{\partial L}{\partial \boldsymbol{\xi}} + \mathbf{C}_{\boldsymbol{\xi}}{}^{T}\boldsymbol{\lambda} = \mathbf{Q} \tag{3.29}$$

where $\boldsymbol{\xi}$ is the column matrix of generalized coordinates. These generalized coordinates need to definitely describe the position of a body for every point of time but are not fixed to a distinct coordinate system. Though, it can be a lot easier to describe the equation of motion in a suitable coordinate system.

More generally, $\boldsymbol{\xi}$ contains all of the n coordinates of the bodies which make up a mechanical system. The value is $n = 6\,N$ in the three dimensional case if the model consists of N rigid bodies. The Lagrangian L is a scalar and $\boldsymbol{\xi}$ is an array. Hence,

$$\frac{\partial L}{\partial \boldsymbol{\xi}} = \begin{pmatrix} \dfrac{\partial L}{\partial \xi_1} \\ \dfrac{\partial L}{\partial \xi_2} \\ \vdots \\ \dfrac{\partial L}{\partial \xi_n} \end{pmatrix} \tag{3.30}$$

is also an array of length n. Similarly, $\frac{\partial L}{\partial \dot{\boldsymbol{\xi}}}$ is an n by 1 array. Each element of $\frac{\partial L}{\partial \boldsymbol{\xi}}$ indicates the sensitivity of the Lagrangian for the mechanical system to one of the coordinates which define its motion.

The column matrix $\mathbf{Q}$ contains the externally applied, non-potential forces in the model. It is balanced against the three terms on the left-hand side of equation 3.29.

The expression $\frac{d}{dt}\left(\frac{\partial L}{\partial \dot{\xi}}\right)$ represents the acceleration of the mechanical components. The potential forces are contained in $\frac{\partial L}{\partial \xi}$.[18]

Due to the coupling of the N bodies within the multibody system, the motion is constrained by kinematical constraints. For example, if the system's motion is constrained by p kinematical constraints of the form

$$\Phi_j(\xi_1, \cdots, \xi_r; t) = 0 \qquad j = 1, \cdots, p \tag{3.31}$$

it possesses $f = 6N - p$ DOF. Figure 3.2 illustrates two examples for kinematic constraints. Assuming that the x and y direction are both generalized coordinates, the constraint equations comply with equation 3.31.

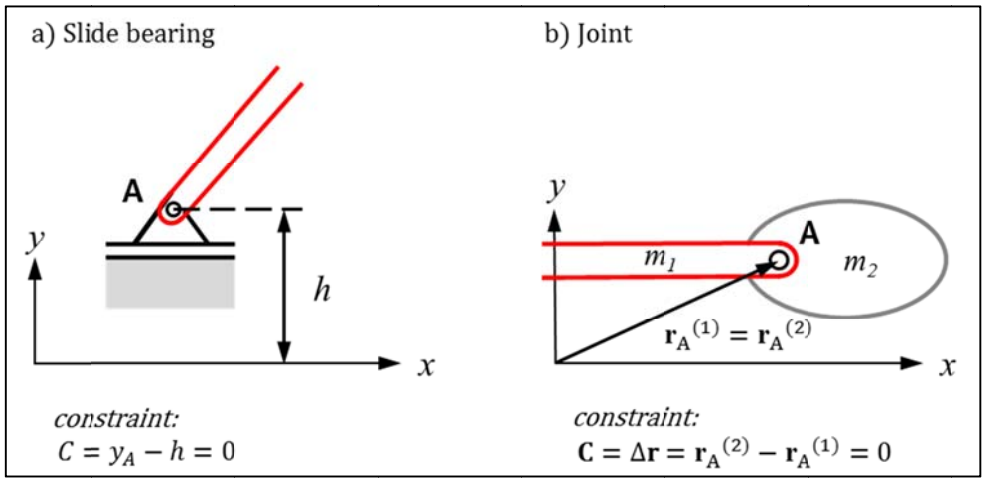

Figure 3.2: Kinematic constraints for a slide bearing (a) and a joint (b)

The Jacobian matrix

$$\mathbf{C}_\xi = \frac{\partial \mathbf{C}}{\partial \boldsymbol{\xi}} \tag{3.32}$$

of the constraint equations is made up of the partial derivatives of the expressions for the constraints with respect to the generalized coordinates. In Lagrangian mechanics,

[18] In MSC/ADAMS/Solver the force of gravity is the only component of $\frac{\partial L}{\partial \xi}$.

$\mathbf{C}_{\boldsymbol{\xi}}{}^{T}$ is the n by m rectangular array which couples the constraint conditions into the force-balance equations. The constraint forces are supplied by $\mathbf{C}_{\boldsymbol{\xi}}{}^{T}\boldsymbol{\lambda}$ where $\boldsymbol{\lambda}$ is the column matrix of m (<n) Lagrange multipliers. $\mathbf{C}_{\boldsymbol{\xi}}{}^{T}$ can be interpreted as the directions of the constraint forces while $\boldsymbol{\lambda}$ contains the amplitudes. Using the Lagrange's multiplier method the system of equations forms a completely defined second order initial value problem.

In the general case, the system of equations becomes

$$\mathbf{M}\,\ddot{\boldsymbol{\xi}} + \dot{\mathbf{M}}\,\dot{\boldsymbol{\xi}} - \frac{1}{2}\,\dot{\boldsymbol{\xi}}^{\mathrm{T}}\,\frac{\partial \mathbf{M}}{\partial \boldsymbol{\xi}}\,\dot{\boldsymbol{\xi}} + \frac{\partial \mathrm{V}}{\partial \boldsymbol{\xi}} + \mathbf{C}_{\boldsymbol{\xi}}{}^{\mathrm{T}}\,\boldsymbol{\lambda} = \mathbf{Q} \tag{3.33}$$

where, if there are n second order differential equations and m constraint equations,

- $\mathbf{M}$ is the n by n mass matrix,
- $\frac{1}{2}\,\dot{\boldsymbol{\xi}}^{T}\,\frac{\partial \mathbf{M}}{\partial \mathbf{q}}\,\dot{\boldsymbol{\xi}}$ is the total kinetic energy,
- V is the potential energy in the system,
- $\mathbf{C}_{\boldsymbol{\xi}}$ is the n by m Jacobian matrix of the constraints and
- $\mathbf{Q}$ represents the applied forces in a column matrix of length n.

Note that the expression $\dot{\mathbf{M}}\,\dot{\boldsymbol{\xi}} - \frac{1}{2}\,\dot{\boldsymbol{\xi}}^{T}\,\frac{\partial \mathbf{M}}{\partial \boldsymbol{\xi}}\,\dot{\boldsymbol{\xi}}$ is needed because the mass matrix $\mathbf{M}$ is not necessarily constant and can also depend on the coordinates $\boldsymbol{\xi}$ and/or the time.

The system of equations (3.23) contains second order differential equations. The ADAMS simulation code makes use of the standard order reduction method by introducing a new dependent variable for each higher derivative and hence, formulates all equations as first order DAE's. These DAE's can be rewritten in an implicit form as

$$\mathbf{G}\left(Y, \dot{Y}, t\right) = 0 \tag{3.34}$$

where $\mathbf{G}$ represents the column matrix of function of the unknowns.

The system as a whole is nonlinear. The implicit system of DAE's is not easily transformable into an explicit system of ordinary differential equations in the form

$$\dot{Y} = f(Y, t) \tag{3.35}$$

to which standard solvers such as Runge-Kutta or the ADAMS-Bashforth-Moulton integrators can be applied. Thus, ADAMS/Solver employs integrators which do accept systems of equations in the implicit form. For the implicit integration algorithm, the DAE's are transformed into a system of nonlinear equations by approximating each derivative in the column matrix $\dot{Y}$ with a backward differentiation formula (BDF). The explanation of the predictor-corrector integration techniques used in ADAMS/Solver to solve the implicit DAE's in the time domain would be beyond the scope of this research paper and is therefore referenced to [**8**].

3.2.2 Integration of Flexible Bodies

The mathematic principles explained in 3.2.1 are also applicable for flexible bodies. In that case the mass matrix dependents on the generalized coordinates $\boldsymbol{\xi}$ and on time. For the analysis of the flexible motion the floating frame of reference formulation is used, which separates the flexible body motion into a reference motion and deformation. Thereby, the deformation of the body is usually described by the superposition of the vibration modes that are obtained from a finite element solution. Thus, FEA software tools like ANSYS have their own interface which allows exporting the mode shapes to ADAMS. The following mathematical explanation of the floating frame of reference formulation is taken from [**10**] and [**11**].

The Kinematics of a Flexible Body

A flexible body consists of particles, the locations of which can be described using a local coordinate system. The local coordinate system is attached to the body, and the deformation of the body is defined with respect to the local, body fixed coordinate system. The local coordinate system can undergo large nonlinear translation and rotation to the fixed global coordinate system.

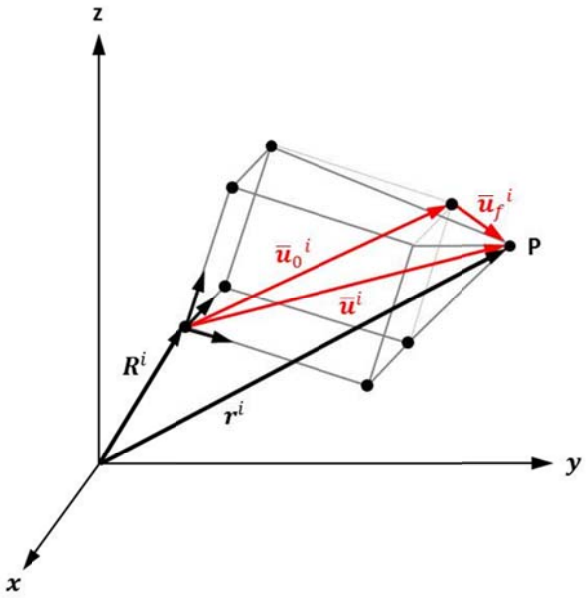

Figure 3.3: Global position of an arbitrary particle P

The global position of an arbitrary particle P, in the flexible body i can be expressed as:

$$\mathbf{r^i = R^i + A^i\,\bar{u}^i = R^i + A^i\left(\bar{u}_0{}^i + \bar{u}_f{}^i\right)} \tag{3.36}$$

where $\bar{\mathbf{u}}_\mathbf{0}{}^\mathbf{i}$ is the position vector that defines the undeformed position of the particle, $\bar{\mathbf{u}}_\mathbf{f}{}^\mathbf{i}$ is the position vector that defines the deformation of the particle and $\mathbf{A^i}$ is the transformation matrix which transforms the $\bar{\mathbf{u}}^\mathbf{i}$ from the local coordinate system to the global coordinate system.

Flexible bodies have an infinite number of degrees of freedom that define the position of every particle of a body. For computational reasons, the deformation vector must be defined using a finite number of coordinates. The approximation can be carried out using the FEA:

$$\bar{\mathbf{u}}_{\mathbf{f}}{}^{\mathbf{i}} = \boldsymbol{\Phi}^{\mathbf{i}}\, \mathbf{p}^{\mathbf{i}}, \tag{3.37}$$

where $\boldsymbol{\Phi}^{i}$ is a shape matrix and $\mathbf{p}^{\mathbf{i}}$ is the vector of elastic coordinates. In practice, the shape matrix can be most completely obtained using the methods described in chapter 3.1.2. Hence, the vector of generalized coordinates of the flexible body $\mathbf{q}$ can be written as follows:

$$\mathbf{q} = [\mathbf{R}^{\mathrm{iT}} \quad \mathbf{A}^{\mathrm{iT}} \quad \mathbf{p}^{\mathrm{iT}}], \tag{3.38}$$

with $\mathbf{R}^{i}$ representing the position vector of the origin of the local coordinate system and $\mathbf{A}^{i}$ is the transformation matrix as described earlier. $\mathbf{A}^{i}$ is determined in ADAMS through a 3-1-3 set of Euler-angles.

The velocity of an arbitrary particle P can be obtained by differentiating equation 3.36 with respect to time through

$$\dot{\mathbf{r}}^{\mathbf{i}} = \dot{\mathbf{R}}^{\mathbf{i}} + \dot{\mathbf{A}}^{\mathbf{i}}\, \bar{\mathbf{u}}^{\mathbf{i}} + \mathbf{A}^{\mathbf{i}}\, \dot{\bar{\mathbf{u}}}^{\mathbf{i}}, \tag{3.39}$$

and by using the time derivative of the position vector in the local coordinate system $\dot{\bar{\mathbf{u}}} = \boldsymbol{\Phi}\, \mathbf{p}$.

Solving The Shape Matrix Using FEA

The shape matrix $\mathbf{\Phi}^{i}$ in equation 3.37 can be constructed using the finite element shape function. However, in most engineering applications, the structure under analysis is rather complex and the finite element model of the entire structure may contain a large number of nodal variables. From a computational perspective, it is not practicable to perform a dynamic analysis based on the complete finite element model. As mentioned earlier, it is possible to exactly determine every arbitrary deformation by using the modal superposition of all eigenmodes of a system. Though, all modes must be Free Interface Normal Modes, which result from a modal analysis of the free, unconstraint flexible body. Due to the fact that mechanical vibrations are usually within a range of 1 to 1000 Hz, the first couple of resulting mode shapes and eigenfrequencies within this range are from higher significance than the occurring mode shapes at higher frequencies. As stated in chapter 3.1.2 the transformation matrix $\mathbf{\Phi}$ is not exactly defined and by applying information of the initial equation 3.3 to fill the matrix, the number of degrees of freedom can be reduced without diluting the first eigenmodes and eigenfrequencies of the system. In doing so problems with the modal superposition can erupt when complex constraints must be applied on the Free Interface Normal Modes. One method to solve this kind of problems is the Craig-Bampton method in which the structure is divided into interior and boundary degrees of freedom.

This method requires defined interface-nodes of the FE structure before the modal segmentation is carried out. Further, the defined nodes form the interface to other MBS substructures after the integration of the flexible body in the multibody system.

The transformation matrix $\mathbf{\Phi}$ is made up of two different kinds of modes. One part of the matrix is filled with the Fixed Interface Normal Modes, which are calculated through an eigenvalue analysis, in which all interface-nodes are fixed. The second part is built from Interface Constraint Modes. These actually cannot be considered as real modes because they do not possess an eigenfrequency. They are rather displacement conditions which occur when a unit displacement is separately applied to each DOF of one interface-node while all other interface DOF are fixed (e.g. 8 interface-nodes with 6 DOF will result in 48 Interface Constraint Modes). The combination of Interface Constraint Modes and Fixed Interface Normal Modes now allows describing every dynamic deformation of the flexible body. The prerequisite therefore is that all Interface Constraint Modes are conserved after the modal segmentation.

Because all interface-nodes must be defined before the modal segmentation, all DOF of the vector $\mathbf{u_f}$ (containing the elastic deformations of all nodes of the FE structure) can be separated into two groups, namely the Boundary DOF $\mathbf{u^B}$ and the Interior DOF $\mathbf{u^I}$.

$$\mathbf{u_f} = \begin{bmatrix} \mathbf{u^B} \\ \mathbf{u^I} \end{bmatrix} \tag{3.40}$$

In this context it is important that forces can be only applied to the Boundary DOF. This emphasis the necessity that the interface DOF are also available for the modal coordinates $\mathbf{q}$. Hence, the vector of modal coordinates can be divided in two subvectors $\mathbf{q^C}$ and $\mathbf{q^N}$, whereby the first is identic with $\mathbf{u^B}$. Accordingly, Equation 3.37 can be rewritten as:

$$\begin{bmatrix} \mathbf{u^B} \\ \mathbf{u^I} \end{bmatrix} = \begin{bmatrix} \mathbf{I} & \mathbf{0} \\ \mathbf{\Phi^{IC}} & \mathbf{\Phi^{IN}} \end{bmatrix} \begin{bmatrix} \mathbf{q^C\ (= u^B)} \\ \mathbf{q^N} \end{bmatrix} \tag{3.41}$$

$$\mathbf{u} = \mathbf{\Phi}\ \mathbf{q} \tag{3.42}$$

Now, the transformation matrix $\mathbf{\Phi}$ can be used to segment the mass matrix $\mathbf{M}$ and the stiffness matrix $\mathbf{K}$, resulting in the generalized mass matrix $\widehat{\mathbf{M}}$ and the generalized stiffness matrix $\widehat{\mathbf{K}}$ of the flexible body:

$$\widehat{\mathbf{M}} = \mathbf{\Phi}^{\mathbf{T}}\,\mathbf{M}\,\mathbf{\Phi} = \begin{bmatrix} \mathbf{I} & \mathbf{0} \\ \mathbf{\Phi}^{\mathbf{IC}} & \mathbf{\Phi}^{\mathbf{IN}} \end{bmatrix}^{\mathbf{T}} \begin{bmatrix} \mathbf{M}^{\mathbf{BB}} & \mathbf{M}^{\mathbf{BI}} \\ \mathbf{M}^{\mathbf{IB}} & \mathbf{M}^{\mathbf{II}} \end{bmatrix} \begin{bmatrix} \mathbf{I} & \mathbf{0} \\ \mathbf{\Phi}^{\mathbf{IC}} & \mathbf{\Phi}^{\mathbf{IN}} \end{bmatrix} = \begin{bmatrix} \widehat{\mathbf{M}}^{\mathbf{CC}} & \mathbf{M}^{\mathbf{NC}} \\ \mathbf{M}^{\mathbf{CN}} & \widehat{\mathbf{M}}^{\mathbf{NN}} \end{bmatrix} \tag{3.43}$$

$$\widehat{\mathbf{K}} = \mathbf{\Phi}^{\mathbf{T}}\,\mathbf{K}\,\mathbf{\Phi} = \begin{bmatrix} \mathbf{I} & \mathbf{0} \\ \mathbf{\Phi}^{\mathbf{IC}} & \mathbf{\Phi}^{\mathbf{IN}} \end{bmatrix}^{\mathbf{T}} \begin{bmatrix} \mathbf{K}^{\mathbf{BB}} & \mathbf{K}^{\mathbf{BI}} \\ \mathbf{K}^{\mathbf{IB}} & \mathbf{K}^{\mathbf{II}} \end{bmatrix} \begin{bmatrix} \mathbf{I} & \mathbf{0} \\ \mathbf{\Phi}^{\mathbf{IC}} & \mathbf{\Phi}^{\mathbf{IN}} \end{bmatrix} = \begin{bmatrix} \widehat{\mathbf{K}}^{\mathbf{CC}} & \mathbf{0} \\ \mathbf{0} & \widehat{\mathbf{K}}^{\mathbf{NN}} \end{bmatrix} \tag{3.44}$$

The indices I, B, N and C stand for the Interior DOF, the Boundary DOF, Fixed Interface Normal Mode and Interface Constraint Mode. Note that these generalized matrices are the Craig-Bampton representation of the original system. It is important to emphasize that the mode shapes in equation 3.41 are not orthogonal with respect to the mass and stiffness matrices. As a result the Craig-Bampton method cannot be directly used for the application in MBS software like ADAMS. One arising issue which limits its direct application is that the method also describes the rigid body motion as a linear combination of Interface Constraint Modes. Because ADAMS computes its own nonlinear motions of the body fixed coordinate system, the six rigid body DOF which are included in the set of Interface Constraint Modes have to be eliminated. However, all problems associated with the direct application of the Craig-Bampton method can be easily overcome through the orthogonalization of the modes by solving the eigenvalues from the Craig-Bampton representation of the structure as follows:

$$\left[\widehat{\mathbf{K}} - \widehat{\omega}_k{}^2\,\widehat{\mathbf{M}}\right]\mathbf{q} = \mathbf{0} \tag{3.45}$$

The new orthogonal mode shape can be summarized within a quadratic ($m\ x\ m$) matrix **N**, which works as a transformation matrix to describe the relationship between the modal coordinates **q** and the modified modal coordinates $\mathbf{q}^*$.

$$\mathbf{q} = \mathbf{N}\,\mathbf{q}^* \tag{3.46}$$

The modal superposition of the physical degrees of freedom $\boldsymbol{u}$ can be determined by applying equation 3.46 to the basic formula 3.37.

$$\mathbf{u} = \boldsymbol{\Phi}\,\mathbf{q} = \boldsymbol{\Phi}\,\mathbf{N}\,\mathbf{q}^* = \boldsymbol{\Phi}^*\mathbf{q}^* \tag{3.47}$$

where $\boldsymbol{\Phi}^*$ is the matrix of orthogonalized Craig-Bampton modes, which is needed when the modified modal coordinates $\mathbf{q}^*$ have to be converted back to the physical coordinates **q**.

As a result of the orthogonalization procedure, the modified, generalized mass and stiffness matrices become diagonal:

$$\mathbf{M}^* = \mathbf{N}^{\mathbf{T}}\,\widehat{\mathbf{M}}\,\mathbf{N} = \mathbf{I}\,, \tag{3.48}$$

$$\mathbf{K}^* = \mathbf{N}^{\mathbf{T}}\,\widehat{\mathbf{K}}\,\mathbf{N} = \mathrm{diag}(\hat{\omega}_1{}^2, \cdots, \hat{\omega}_{n_{CB}}{}^2) \tag{3.49}$$

A useful side effect is that all the modes have an associated frequency for their frequency contribution to the dynamic system. The orthogonalized Craig-Bampton modes are different to the eigenvectors of the original system and include approximate free-free modes and the vibration modes of the Boundary DOF.

The System's Equation of Motion

The Lagrangian Equation 3.33 can now be adjusted for the flexible multibody system:

$$\mathbf{M}\,\ddot{\boldsymbol{\xi}} + \dot{\mathbf{M}}\,\dot{\boldsymbol{\xi}} - \frac{1}{2}\boldsymbol{\xi}^{\mathrm{T}}\,\frac{\partial \mathbf{M}}{\partial \boldsymbol{\xi}}\,\dot{\boldsymbol{\xi}} + \frac{\partial V}{\partial \boldsymbol{\xi}} + \mathbf{K}\,\boldsymbol{\xi} + \mathbf{f_g} + \mathbf{D_d}\,\dot{\boldsymbol{\xi}} + \mathbf{C_\xi}^{\mathrm{T}}\,\boldsymbol{\lambda} = \mathbf{Q_e} \tag{3.50}$$

Where $\mathbf{f_g}$ is the gravitational force and $\mathbf{Q_e}$ is the vector of the generalized external forces. The stiffness matrix $\mathbf{K}$ and the damping matrix $\mathbf{D_d}$ can be written as

$$\mathbf{K} = \begin{bmatrix} \mathbf{0} & \mathbf{0} & \mathbf{0} \\ \mathbf{0} & \mathbf{0} & \mathbf{0} \\ \mathbf{0} & \mathbf{0} & \mathbf{K}^{*} \end{bmatrix}, \qquad \mathbf{D} = \begin{bmatrix} \mathbf{0} & \mathbf{0} & \mathbf{0} \\ \mathbf{0} & \mathbf{0} & \mathbf{0} \\ \mathbf{0} & \mathbf{0} & \mathbf{D}^{*} \end{bmatrix} \tag{3.51}$$

where $\mathbf{0}$ are null matrices and matrix $\mathbf{D}^{*}$ contains modal damping ratios. Using the expressions

$$\mathbf{Q_v} = -\dot{\mathbf{M}}\,\dot{\boldsymbol{\xi}} - \frac{1}{2}\,\dot{\boldsymbol{\xi}}^{\mathrm{T}}\,\frac{\partial \mathbf{M}}{\partial \boldsymbol{\xi}}\,\dot{\boldsymbol{\xi}} + \frac{\partial V}{\partial \boldsymbol{\xi}}, \tag{3.52}$$

$$\mathbf{Q_E} = \mathbf{Q_e} - \mathbf{K}\,\boldsymbol{\xi} - \mathbf{f_g} - \mathbf{D_d}\,\dot{\boldsymbol{\xi}}, \tag{3.53}$$

the equation of constrained motion takes the following form:

$$\mathbf{M}\ddot{\boldsymbol{\xi}} + \mathbf{C_\xi}^{\mathrm{T}}\boldsymbol{\lambda} = \mathbf{Q_E} + \mathbf{Q_v}\,, \tag{3.54}$$

where $\mathbf{Q_v}$ is a vector of quadratic velocity inertia forces that includes the gyroscopic and Coriolis forces. The vector of the quadratic velocity inertia forces is a nonlinear function of the system's generalized coordinates and velocities. The force vector $\mathbf{Q_E}$ includes the descriptions of both conservative and non-conservative forces.

4 Rotordynamic Analysis of a simple Overhung Rotor

As described in the previous chapter, the FE-Simulation and the MBS use different approaches to solve the equations of a dynamic system. The aim of this chapter is on the one hand the evaluation of the solutions of both methods regarding rotordynamics by analyzing the eigenfrequencies of a simple rotordynamic system and comparing it to the analytical solution and on the other hand the investigation of a change in the linear bearing stiffness. For the FEA the simulation environment ANSYS Classic will be used, while the MBS will be carried out in ADAMS.

The examined system is a simple overhung rotor with a massless shaft and a rigid rotor disc supported by two bearings (Figure 4.1). The assumed geometrical dimensions in respect of actual refiner dimensions are provided in Table 4-1.

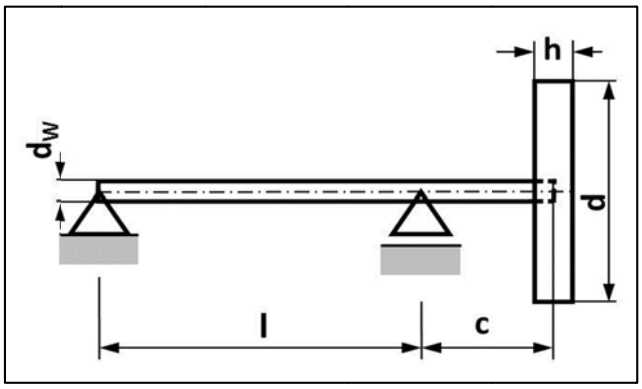

Figure 4.1: Model of overhung rotor

Parameter	Length
l	1 m
c	0.5 m
d	1 m
d_W	0.1 m
h	0.1 m

Table 4-1: Dimensions of the model

4.1 Analytical Solution

In order to formulate and to understand the dynamic system of equations for the overhung rotor, the first part of the analytical solution is dedicated to the general derivation of the motion equations by using a simple Jeffcott rotor. The following examination also considers the gyroscopic effects mentioned in chapter 2.3 and is established on the derivations of [**1**].

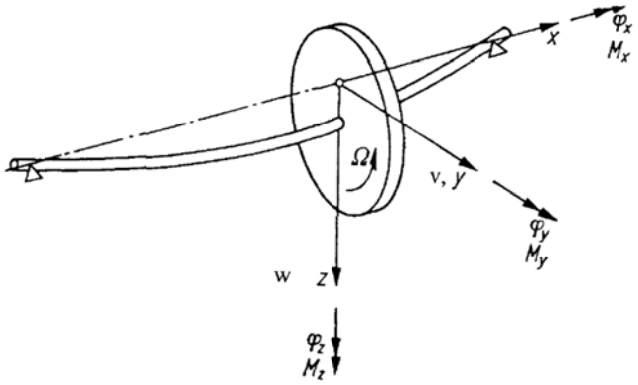

Figure 4.2: DOF of the rotating Jeffcott rotor[19]

For the formulation of the system's equation of motion, the relationship between the displacements and rotations at the disc fit and the resulting forces and moments are needed. This linear relationship can be described in matrix form as

$$\begin{bmatrix} F_z \\ M_y \\ F_y \\ M_z \end{bmatrix}_W = \begin{bmatrix} k_{11} & k_{12} & 0 & 0 \\ k_{21} & k_{22} & 0 & 0 \\ 0 & 0 & k_{11} & -k_{12} \\ 0 & 0 & -k_{21} & k_{22} \end{bmatrix} \begin{bmatrix} w \\ \varphi_y \\ v \\ \varphi_z \end{bmatrix} \tag{4.1}$$

$$\mathbf{f}_W = \mathbf{K}\,\mathbf{x}_W \tag{4.2}$$

Because the forces and moments in $\mathbf{f}_W$ only cause deformations in their acting plane, the coupling terms of the stiffness matrix **K** are blank and due to Betti's theorem, $k_{12} = k_{21}$ is applicable.

[19] [**1**], p. 160

The influence of the rotating motion and the gyroscopic effects can be determined by using the principle of the conservation of angular momentum[20]. It states that the resulting moment of all external acting forces and the temporal change of the angular momentum are in equilibrium. In order to establish the angular momentum equations, a body-fixed coordinate system (x', y', z') is introduced, which has its point of origin in the center of the disc. Though, the x'-axis matches the symmetry axis of the disc (Figure 4.3).

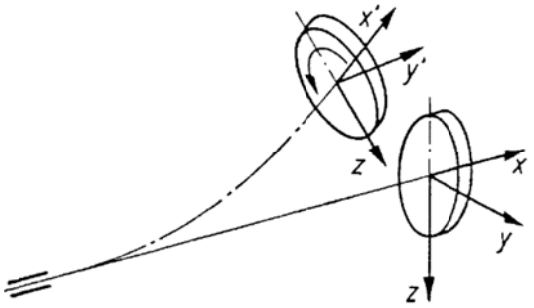

Figure 4.3: x', y', z'-principal coordinate system on the rotation-symmetric disc[21]

This coordinate system moves with the center of the disc in the translational directions w and v and pitches with the disc around the y and the z axis but without rotation around the x'-axis. Hence, the angular momentum is

$$\mathbf{L}' = \begin{bmatrix} L_{x'} \\ L_{y'} \\ L_{z'} \end{bmatrix} = \begin{bmatrix} \Theta_{\mathrm{P}}\dot{\varphi}_{\mathrm{x}} \\ \Theta_a\dot{\varphi}_{\mathrm{y}} \\ \Theta_a\dot{\varphi}_{\mathrm{z}} \end{bmatrix} \tag{4.3}$$

where Θ_P is the polar moment of inertia and Θ_a is the geometrical moment of inertia. Because the angular momentum is now described in a body-fixed coordinate system it is necessary to transform it back into the space-fixed coordinate system x, y, z.

[20] conservation of angular momentum ≙ deut. Drallsatz
[21] [**1**], p. 164

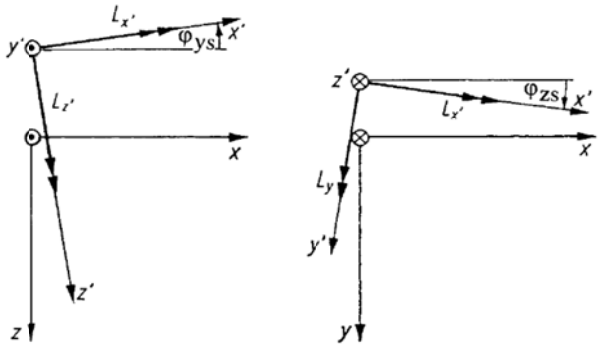

Figure 4.4: Components of the angular momentum in the space-fixed coordinate system[22]

Through the transformation with $\dot{\varphi}_x = -\Omega = const.$ equation 4.3 can be written as

$$\mathbf{L} = \begin{bmatrix} L_x \\ L_y \\ L_z \end{bmatrix} = \begin{bmatrix} -\Theta_P \Omega \\ L_{y'} \cos(\varphi_{zs}) + L_{z'} \sin(\varphi_{zs}) \\ L_{z'} \cos(\varphi_{ys}) - L_{x'} \sin(\varphi_{ys}) \end{bmatrix} \tag{4.4}$$

By assuming small angles, the angular momentum equation can be simplified through linearization of the trigonometric functions, i.e. $\sin\varphi \cong \varphi$ respectively $\cos\varphi \cong 1$.

$$\mathbf{L} = \begin{bmatrix} -\Theta_P \Omega \\ L_{y'} + L_{z'} \varphi_{zs} \\ L_{z'} + L_{x'} \varphi_{ys} \end{bmatrix} = \begin{bmatrix} -\Theta_P \Omega \\ \Theta_a \dot{\varphi}_{ys} - \Theta_P \Omega \varphi_{zs} \\ \Theta_a \dot{\varphi}_{zs} + \Theta_P \Omega \varphi_{ys} \end{bmatrix} \tag{4.5}$$

The principle of the conservation of angular momentum determines that the time derivative of the angular momentum is equal to the acting moment, hence

$$\dot{\mathbf{L}} = \begin{bmatrix} 0 \\ \Theta_a \ddot{\varphi}_{ys} - \Theta_P \Omega \dot{\varphi}_{zs} \\ \Theta_a \ddot{\varphi}_{zs} + \Theta_P \Omega \dot{\varphi}_{ys} \end{bmatrix} = \begin{bmatrix} M_x \\ M_y \\ M_z \end{bmatrix} \tag{4.6}$$

The terms $\Theta_a \ddot{\varphi}_{ys}$ and $\Theta_a \ddot{\varphi}_{zs}$ describe the moments resulting from the rotating inertia, which is acting against the inclination. They are also present if the shaft is not spinning ($\Omega = 0$). The terms $-\Omega\Theta_P \dot{\varphi}_{zs}$ and $\Omega\Theta_P \dot{\varphi}_{ys}$ reflect the gyroscopic influence.

[22] [**1**], p. 165

Not only the moments M_y and M_z are influencing the dynamic behavior of the disc, besides them also the external forces F_y and F_z are acting. Thus, the principle of linear momentum for the external forces F_y and F_z must be added to equation 4.6 in order to get a complete equation of motion. F_y and F_z can be formulated according to Newton's dynamic law as $F_y = m \cdot \ddot{v}_S$ and $F_z = m \cdot \ddot{w}_S$.

This relationship can be summarized in matrix form as

$$-\begin{bmatrix} F_z \\ M_y \\ F_y \\ M_z \end{bmatrix}_w = \begin{bmatrix} m & 0 & 0 & 0 \\ 0 & \theta_a & 0 & 0 \\ 0 & 0 & m & 0 \\ 0 & 0 & 0 & \theta_a \end{bmatrix} \begin{bmatrix} \ddot{w}_s \\ \ddot{\varphi}_{ys} \\ \ddot{v}_s \\ \ddot{\varphi}_{zs} \end{bmatrix} + \begin{bmatrix} 0 & 0 & 0 & 0 \\ 0 & 0 & 0 & -\Omega\theta_P \\ 0 & 0 & 0 & 0 \\ 0 & \Omega\theta_P & 0 & 0 \end{bmatrix} \begin{bmatrix} \dot{w}_s \\ \dot{\varphi}_{ys} \\ \dot{v}_s \\ \dot{\varphi}_{zs} \end{bmatrix} \tag{4.7}$$

$$\mathbf{f}_S = \mathbf{M} \ddot{\boldsymbol{x}}_s + \boldsymbol{G} \dot{\boldsymbol{x}}_s \tag{4.8}$$

The equation 4.8 contains all externally acting forces and moments within the column matrix $\boldsymbol{f}_S$. According to Newton's third postulate "actio=reactio", the complete dynamic system can now be expressed as a combination of equation 4.1 and 4.7

$$\begin{bmatrix} m & 0 & 0 & 0 \\ 0 & \theta_a & 0 & 0 \\ 0 & 0 & m & 0 \\ 0 & 0 & 0 & \theta_a \end{bmatrix} \begin{bmatrix} \ddot{w}_s \\ \ddot{\varphi}_{ys} \\ \ddot{v}_s \\ \ddot{\varphi}_{zs} \end{bmatrix} + \begin{bmatrix} 0 & 0 & 0 & 0 \\ 0 & 0 & 0 & -\Omega\theta_P \\ 0 & 0 & 0 & 0 \\ 0 & \Omega\theta_P & 0 & 0 \end{bmatrix} \begin{bmatrix} \dot{w}_s \\ \dot{\varphi}_{ys} \\ \dot{v}_s \\ \dot{\varphi}_{zs} \end{bmatrix} + \\ + \begin{bmatrix} k_{11} & k_{12} & 0 & 0 \\ k_{21} & k_{22} & 0 & 0 \\ 0 & 0 & k_{11} & -k_{12} \\ 0 & 0 & -k_{21} & k_{22} \end{bmatrix} \begin{bmatrix} w \\ \varphi_{ys} \\ v \\ \varphi_{zs} \end{bmatrix} = 0 \tag{4.9}$$

For further examination of the system of equations it is practicable to combine the translational and rotational component to a complex expression, because it will halve the number of unknowns.

$$r_s = w_s + jv_s \tag{4.10}$$

$$\varphi_s = \varphi_{zs} + j\varphi_{ys} \tag{4.11}$$

As a consequence equation 4.9 can be rewritten as

$$\begin{bmatrix} m & 0 \\ 0 & \Theta_a \end{bmatrix} \begin{bmatrix} \ddot{r}_s \\ \ddot{\varphi}_s \end{bmatrix} + \begin{bmatrix} 0 & 0 \\ 0 & -j\Theta_P\Omega \end{bmatrix} \begin{bmatrix} \dot{r}_s \\ \dot{\varphi}_s \end{bmatrix} + \begin{bmatrix} k_{11} & -jk_{12} \\ jk_{21} & k_{22} \end{bmatrix} \begin{bmatrix} r_s \\ \varphi_s \end{bmatrix} = 0. \tag{4.12}$$

Due to the disc's eccentricity ε, its center of gravity S and the point of intersection between the shaft and the disc W do not coincide and cause an unbalance $U = m\,\varepsilon$. Through the shaft's rotation the unbalance is leading to an unbalance force which forces the shaft to bend.

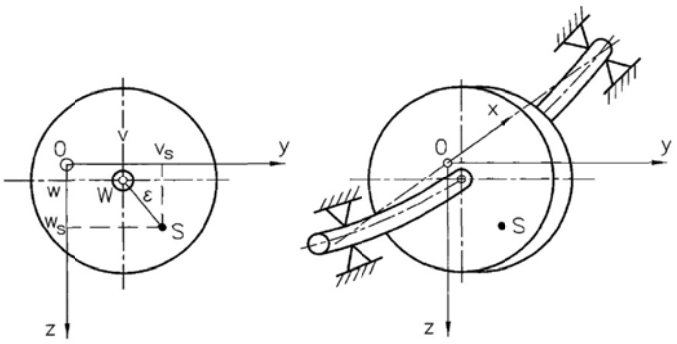

Figure 4.5: Shaft deflection due to unbalance force[23]

In case of a uniform shaft rotation, the deflection of the disc's center of gravity r_s and the bending of the shaft r can be combined by $r_s = r + \varepsilon\, e^{j(\Omega t+\beta)}$. If the disc is not exactly perpendicular to the shaft axis, also the angles of the shaft φ and the disc φ_s must be distinguished. When α is the inclination angle between the shaft and the disc, the completely analogue relation $\varphi_s = \varphi + \alpha e^{j(\Omega t+\gamma)}$ is valid.

Considering the eccentricity and the resulting unbalance force the motion equations for the Jeffcott rotor (4.12) are transformed to

$$\begin{bmatrix} m & 0 \\ 0 & \Theta_a \end{bmatrix} \begin{bmatrix} \ddot{r} \\ \ddot{\varphi} \end{bmatrix} + \begin{bmatrix} 0 & 0 \\ 0 & -j\Theta_P\Omega \end{bmatrix} \begin{bmatrix} \dot{r} \\ \dot{\varphi} \end{bmatrix} + \begin{bmatrix} k_{11} & -jk_{12} \\ jk_{21} & k_{22} \end{bmatrix} \begin{bmatrix} r \\ \varphi \end{bmatrix} = \\ = \Omega^2 \begin{bmatrix} m\varepsilon e^{j\beta} \\ (\Theta_a - \Theta_P)\alpha e^{j\gamma} \end{bmatrix} e^{j\Omega t}. \tag{4.13}$$

[23] [**1**], p. 40

4.1.1 Solving the DAE System

For the computation of the shaft's free vibrations the homogeneous solution of 4.13 has to be found. This can be achieved by using the exponential approach

$$\begin{bmatrix} r \\ \varphi \end{bmatrix} = \begin{bmatrix} \hat{r} \\ \hat{\varphi} \end{bmatrix} e^{j\omega t}. \tag{4.14}$$

Employing equation 4.14 to the linear homogenous equation system yields to

$$\begin{bmatrix} -m\omega^2 + k_{11} & -jk_{12} \\ jk_{21} & -\Theta_a\omega^2 + \Theta_P\Omega\omega + k_{22} \end{bmatrix} \begin{bmatrix} \hat{r} \\ \hat{\varphi} \end{bmatrix} e^{j\omega t} = 0. \tag{4.15}$$

This has only a nontrivial solution if the coefficient determinant dissolves.

$$det \begin{bmatrix} -m\omega^2 + k_{11} & -jk_{12} \\ jk_{21} & -\Theta_a\omega^2 + \Theta_P\Omega\omega + k_{22} \end{bmatrix} = 0. \tag{4.16}$$

Solving the determinant leads to the following characteristic equation

$$m\Theta_a\omega^4 - m\Theta_P\Omega\omega^3 - (mk_{22} + \Theta_a k_{11})\omega^2 + \Theta_P k_{11}\Omega\omega + k_{11}k_{22} - {k_{12}}^2 = 0, \tag{4.17}$$

which can now be easily implemented in MATLAB.

4.1.2 Computation of the free vibrations in MATLAB

Before the eigenfrequencies of the spinning rotor can be computed, the moments of inertia, stiffnesses and masses have to be calculated. Table 4-2 contains the assumed material properties.

Material Properties	
Young's modulus	$E = 210 \cdot 10^9$ Pa
Density	$\rho = 7850$ kg/m^3
Poisson's ratio	**0.3**

Table 4-2: Material properties of the overhung rotor

The geometrical moment of inertia of the shaft can be calculated with

$$I_W = \left(\frac{d_W}{2}\right)^4 \frac{\pi}{4}, \tag{4.18}$$

while for the moments of inertia of the disc

$$\Theta_p = \frac{1}{2}\, m\, R^2 \quad \text{and} \tag{4.19}$$

$$\Theta_a = \frac{1}{12}\, m\, (3R^2 + l^2) \tag{4.20}$$

are used.

Until now, all derived equations are valid for the Jeffcott rotor as well as for the overhung rotor shown in Figure 4.1. The difference between the centered rotor system, the Jeffcott rotor is representing, and the overhung rotor model lies in the stiffness matrix **K**. Bearing conditions and the position of the disc fit mainly influence the shaft's deflection. In order to solve the characteristic equation (4.17) the stiffness matrix of the shaft for the described overhung rotor model has to be derived. Therefore the analytical methods for analyzing beam systems will be used since the shaft can be considered as beam with constant bending stiffness *EI*.

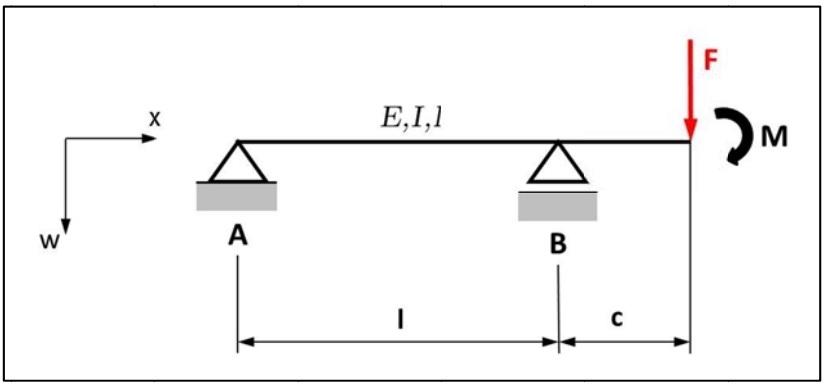

Figure 4.6: Equivalent statical system of overhung rotor model

Figure 4.6 shows the equivalent statical system of the overhung rotor model. The rotor disc is substituted with the acting force and moment caused by the weight of the disc.

The following DAE's show the general relationship between the derivatives of the deflection w and distributed load q, shear force Q, bending moment M and bending angle φ for a constant EI.

$$EI\, w''''_{(x)} = q_{(x)} \tag{4.21}$$

$$EI\, w'''_{(x)} = -Q_{(x)} \tag{4.22}$$

$$EI\, w''_{(x)} = -M_{(x)} \tag{4.23}$$

$$w'_{(x)} = -\varphi_{(x)} \tag{4.24}$$

Now, $w_{(x)}$ can be derived for a known $\mathrm{q}_{(x)}$ by integration. Due to the discontinuity generated by the bearing force B in the load distribution, the Föppl-symbol is used in the following equations.

$$EI_W\, \mathrm{w}''''_{(x)} = \mathrm{q}_{(x)} = -\mathrm{B}\,\langle x-l\rangle_{-1} \tag{4.25}$$

$$EI_W\, \mathrm{w}'''_{(x)} = -\mathrm{Q}_{(x)} = -\mathrm{B}\,\langle x-l\rangle^0 + C_1 \tag{4.26}$$

$$EI_W\, \mathrm{w}''_{(x)} = -\mathrm{M}_{(x)} = -\mathrm{B}\,\langle x-l\rangle^1 + C_1 x + C_2 \tag{4.27}$$

$$EI_W\, \mathrm{w}'_{(x)} = -EI\,\varphi_{(x)} = -\frac{\mathrm{B}}{2}\,\langle x-l\rangle^2 + \frac{C_1}{2}x^2 + C_2\mathrm{x} + C_3 \tag{4.28}$$

$$EI_W\, w_{(x)} = -\frac{\mathrm{B}}{6}\,\langle x-l\rangle^3 + \frac{C_1}{6}x^3 + \frac{C_2}{2}\mathrm{x}^2 + C_3 x + C_4 \tag{4.29}$$

The unknown integration constants C_1 to C_4 can be determined by establishing the system's border conditions and inserting them into the suitable equations:

1. $x = 0$: $\quad w_{(0)} = 0 \;\rightarrow\; C_4 = 0$

$\quad M_{(0)} = 0 \;\rightarrow\; C_2 = 0$

2. $x = \mathrm{l}$: $\quad w_{(l)} = 0 \;\rightarrow\; C_3 = -\frac{C_1}{6}\,l^2$

3. $x = \mathrm{l} + \mathrm{c}$: $\quad Q_{(l+c)} = F \;\rightarrow\; C_1 = B - F$

$\rightarrow\; M_{(l+c)} = -B\,c + (B-F)(l+c) \;\rightarrow\; B = \frac{F\,(l+c)-M}{l}$

$\rightarrow\; C_1 = \frac{F\,c-M}{l}$

$\rightarrow\; C_3 = \frac{(M-F\,c)l}{6}$

After all integration constants and the bearing force B are expressed in terms of M and F, equation 4.28 and 4.29 can be stated as

$$EI_W\,\bar{w} = F\left[\frac{1}{3}c^2(l+c)\right] + M\left[-\frac{1}{6}c(2l+3c)\right] \text{ and} \tag{4.30}$$

$$EI_W\,\bar{\varphi} = F\left[-\frac{1}{6}c(2l+3c)\right] + M\left[\frac{1}{3}c(l+3c)\right], \tag{4.31}$$

resulting in the matrix formulation

$$\begin{bmatrix}\bar{w}\\ \bar{\varphi}\end{bmatrix} = \frac{1}{EI_W}\underbrace{\begin{bmatrix}\frac{1}{3}c^2(l+c) & -\frac{1}{6}c(2l+3c)\\ -\frac{1}{6}c(2l+3c) & \frac{1}{3}c(l+3c)\end{bmatrix}}_{\mathbf{N}}\begin{bmatrix}F\\ M\end{bmatrix}. \tag{4.32}$$

The stiffness matrix $\mathbf{K}$ equals the inverse matrix of the compliance matrix $\mathbf{N}^{-1}$

$$\mathbf{K} = \mathbf{N}^{-1} = EI_W\begin{bmatrix}\frac{12\,(l+3c)}{c^3\,(4l+3c)} & \frac{6\,(2l+3c)}{c^2\,(4l+3c)}\\ \frac{6\cdot(2l+3c)}{c^2\,(4l+3c)} & \frac{12\,(l+c)}{c\,(4l+3c)}\end{bmatrix}, \tag{4.33}$$

containing the stiffness coefficients summarized in Table 4-3.

Stiffness Matrix Coefficients	
$\mathbf{k_{11}}$	$\frac{12\,(l+3c)}{c^3\,(4l+3c)}$
$\mathbf{k_{12}} = \mathbf{k_{21}}$	$-\frac{6\,(2l+3c)}{c^2\,(4l+3c)}$
$\mathbf{k_{22}}$	$\frac{12\,(l+c)}{c\,(4l+3c)}$

Table 4-3: Stiffness matrix coefficients

All constants necessary to solve the free vibration problem of the overhung rotor can now be calculated in MATLAB (see Appendix).

Next, the four eigenfrequencies of the system are computed for a speed range from $\Omega = 0$ rpm to $\Omega = 3000$ rpm by solving equation 4.17. The resulting Campbell-Diagram is shown in Figure 4.7.

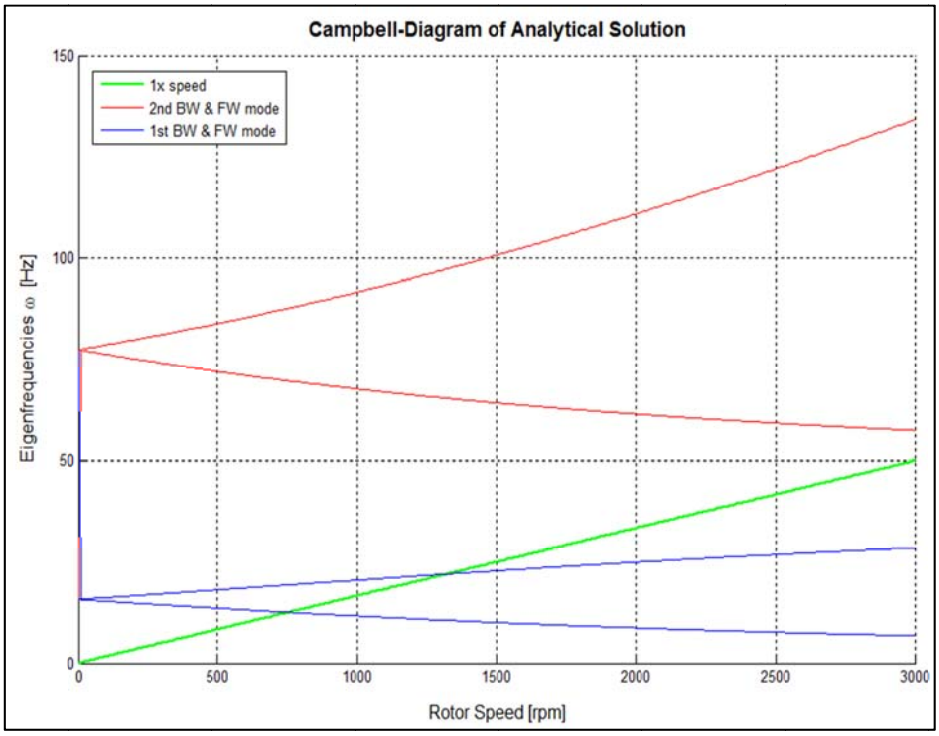

Figure 4.7: Campbell-Diagram of Analytical Solution

The critical speeds occur at 750 rpm and 1300 rpm, when the speed of the rotor passes the first horizontal and vertical mode.

4.2 FE-Calculation in ANSYS Classic

For the modeling of the simple overhung rotor in ANSYS Classic, the geometry of the rotor's disc and shaft are discretized with beam elements. A line model is used as basic geometry, while the cross-section information of shaft and disc is defined by using two different sections. This cross-section information is assigned to the beam189 elements before the actual meshing procedure. Through the meshing, all the information is applied to the line structure. Note that the density defined for the shaft is almost zero in order to realize the massless shaft. The support conditions can be

implemented by constraining the nodes where the bearings are acting. After doing so, the modal rotordynamic analysis can be started. Therefore commands have to be added to the modal analysis for the computation of eigenfrequencies for different rotational speeds and the Stationary Reference Frame has to be activated (see Appendix). The ANSYS model and the resulting Campbell-Diagram are summarized in Figure 4.8.

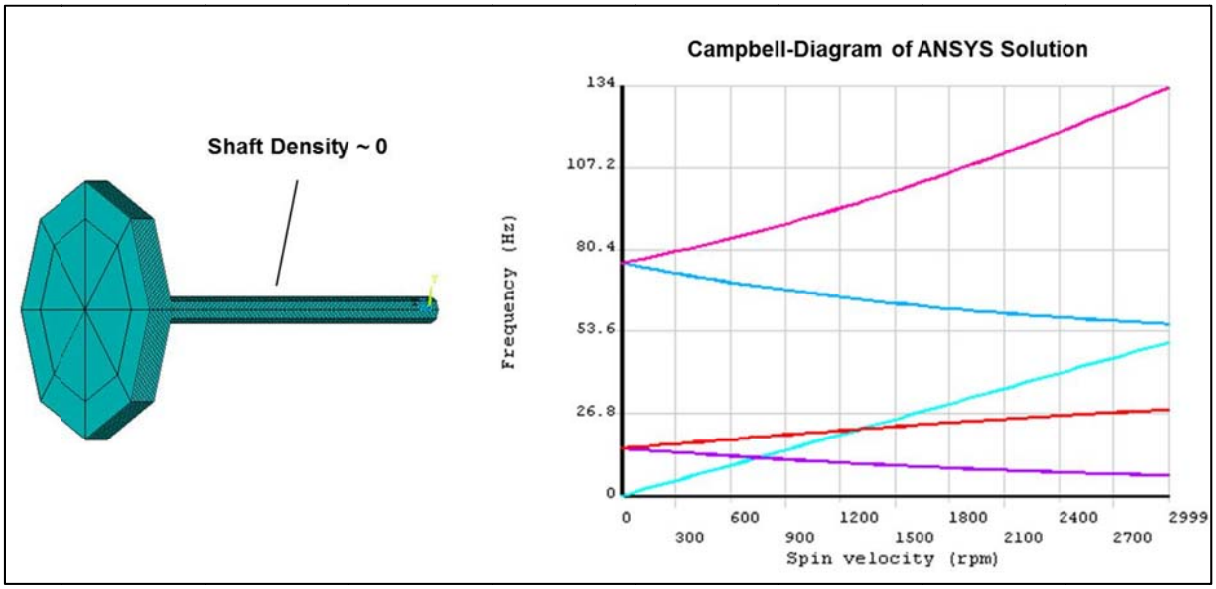

Figure 4.8: ANSYS model and Campbell-Diagram of ANSYS Solution

4.3 Multibody Simulation in ADAMS

The multibody analysis of the flexible rotor in ADAMS requires the orthogonalized Craig-Bampton modes of the flexible structure. Because the rotor disc can be considered rigid, only the mode shapes of the flexible shaft are needed. Therefore the ANSYS-ADAMS interface is used. Before the modal analysis of the massless shaft is performed, the interface nodes and the number of modes to extract must be defined, and all forces and constraints on the model must be removed. In the case of the overhung rotor both nodes where the bearing forces are acting and the node where the disc center is connected to the shaft are defined as interface nodes. The

resulting modal neutral file (.mnf) of the structure can then be easily imported in ADAMS and is automatically aligned in the x-y-z global coordinate system as it was modeled in ANSYS.

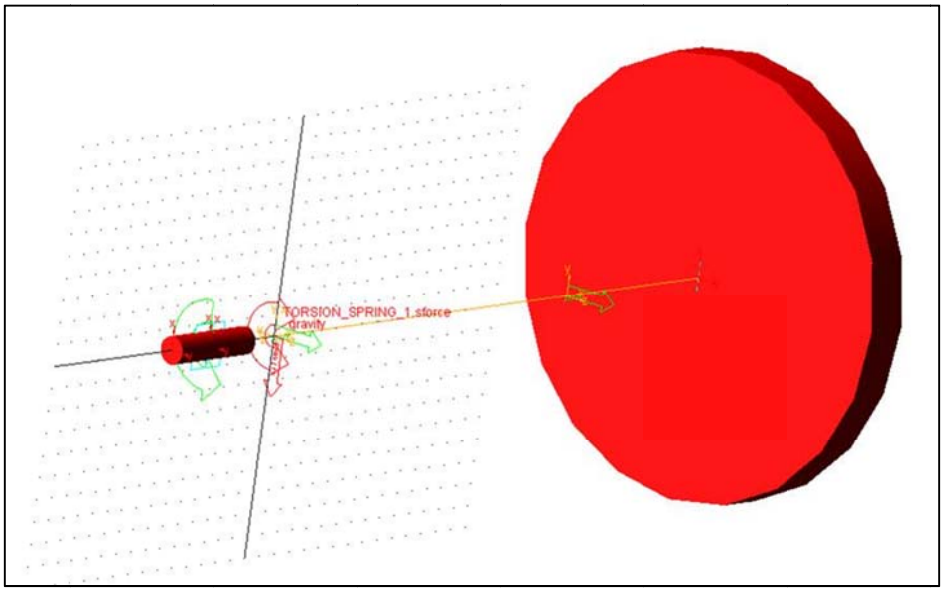

Figure 4.9: ADAMS model with flexible shaft and rigid rotor

Next, the rigid disc is modeled according the assumed geometric data, and connected through a fixed joint to the interface point of the flexible shaft. The bearing constraints are realized via point motions which block the translational DOF. The actuator for the rotating motion and the flexible shaft are connected by a very stiff torsion spring and the rotational speed is defined through a general variable. Despite the coupling between the actuator and the flexible shaft, the rotational speed of the flexible body must be defined separately to assure that the rotating motion of the shaft follows the motion of the actuator. For the acquisition of the MBS Campbell-Diagram eleven simulations are computed with an increasing rotational speed starting from 0 Hz in 5 Hz steps until 50 Hz. Each simulation runs for 5 seconds followed by an eigenvalue calculation in order to get the eigenfrequencies of the system. Figure 4.10 shows the resulting diagram.

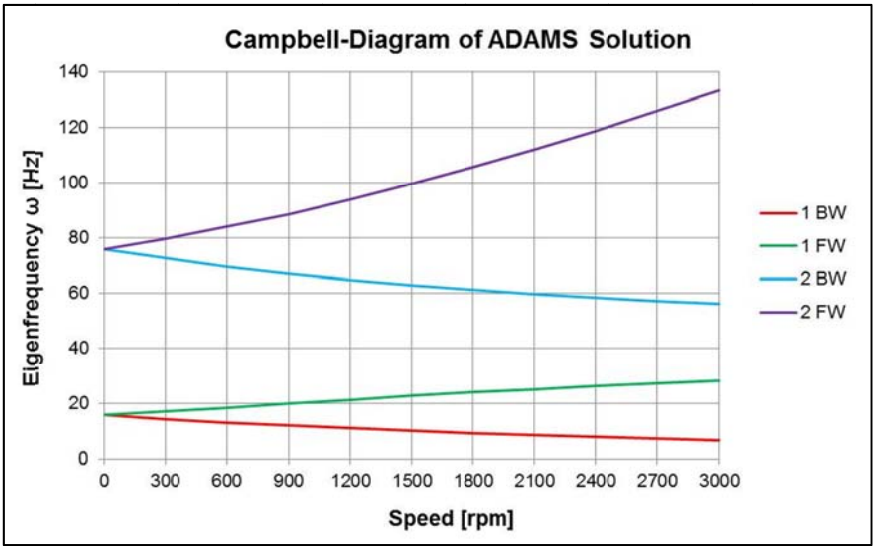

Figure 4.10: Campbell-Diagram of ADAMS solution

4.4 Comparison of Analyses

After all eigenfrequency analyses have been carried out the results of the FE-simulation, the MBS-simulation and the analytical solution are plotted.

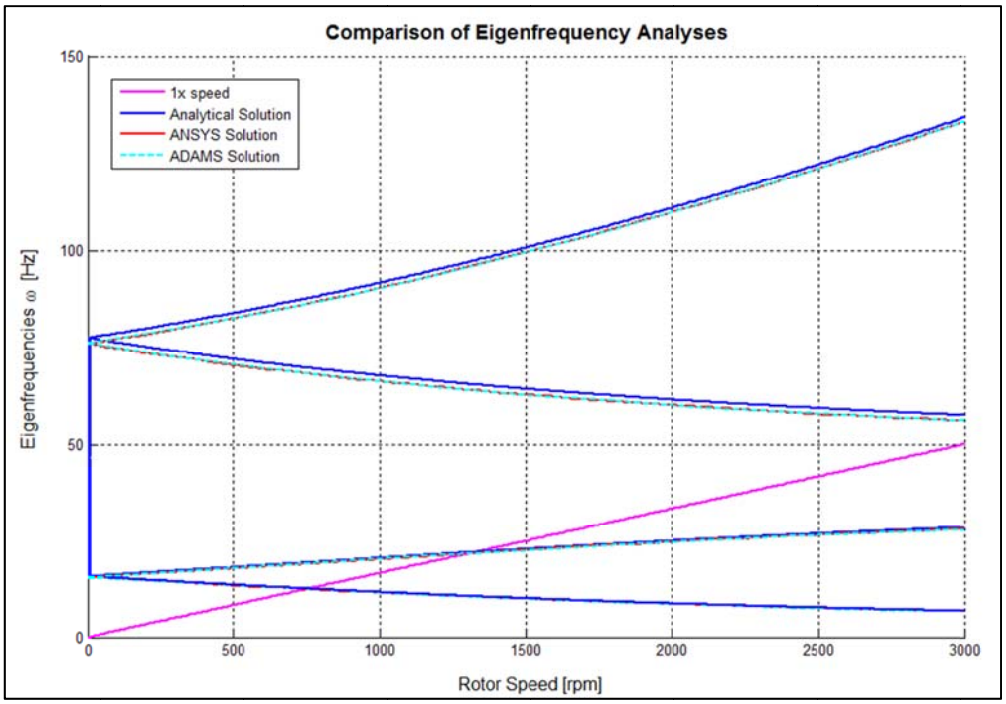

Figure 4.11: Comparison of eigenfrequency analyses

Figure 4.11 shows clearly that all first backward (BW) and forward (FW) modes are identical. The second BW and FW mode shapes of the ADAMS and ANSYS solution are also identical but deviate slightly from the analytical solution (error ratio ≅ 2%).
In the next step, mass is added to the flexible shaft. Obviously the resulting eigenfrequency change a little but the MBS and FE solution are alike again.

4.5 Eigenfrequency Analyses with Isotropic Bearing Stiffness

In this section an eigenfrequency analysis will be performed on the overhung rotor model with isotropic bearings. The fixed bearing and the floating bearing of Figure 4.1 are exchanged for bearings with isotropic stiffness (Figure 4.12).

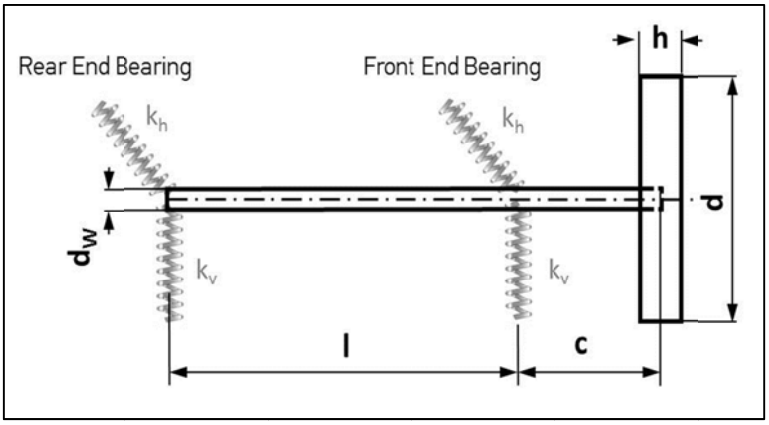

Figure 4.12: Overhung rotor model with isotropic bearings

The geometrical parameters are the same as noted in Table 4-1, while the added horizontal and vertical bearing stiffnesses are assumed with $1e^9$ N/m. For the realization of the linear bearing stiffness in ANSYS the COMBI214 element is applied. It has longitudinal as well as cross-coupling capability in 2-D applications.

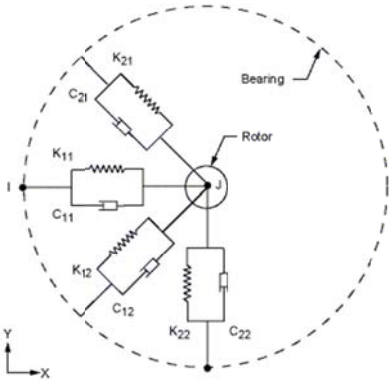

Figure 4.13: Function principle of the COMBI214 element[24]

The COMBI214 element is a tension-compression element with up to two degrees of freedom at each node: translations in any two nodal directions (x, y, or z). There is no bending or torsion considered. The stiffnesses k_{11} and k_{22} can be defined through "real constants". Unfortunately the element is not available in the ANSYS Classic GUI and must be entered in code form.

The COMBI214 element has to be defined between two nodes. In case of the overhung rotor FE-model two Keypoints are defined at the bearing positions on the shaft center line, and 2 additional Keypoints are offset in z-direction to them. Note that the Keypoints on the shaft center line have to be used also by the BEAM189 elements because otherwise no connection between them and the COMBI214 is established (Figure 4.14).

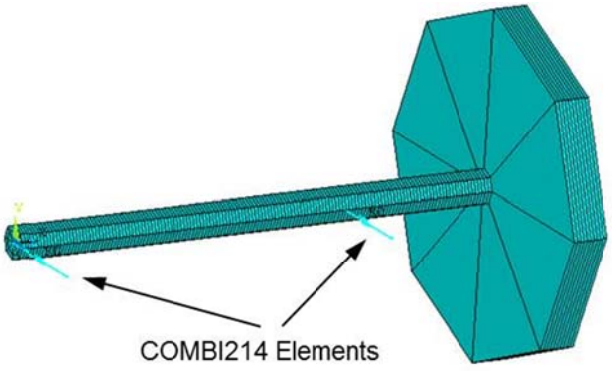

Figure 4.14: ANSYS model with COMBI214 elements

[24] ANSYS Help

In ADAMS, the isotropic bearings are implemented by removing the point motions and constraining the interface points of the flexible shaft with linear springs (Figure 4.15). The linear spring stiffness can be assigned by modifying the stiffness coefficient of the spring element.

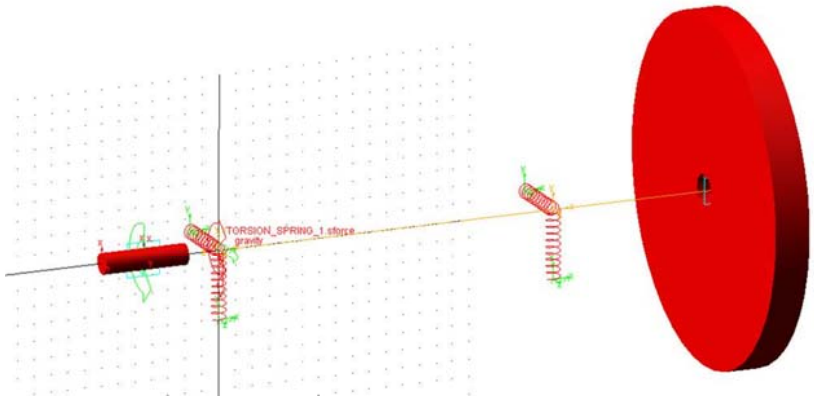

Figure 4.15: ADAMS model with linear springs

It has to be noted that in both, the ANSYS and the ADAMS model, the translational movement in the direction of the rotation axis is also constrained.

After performing the same modal analyses as described in chapter 4.2 and 4.3 the resulting Campbell-Diagrams are compared again.

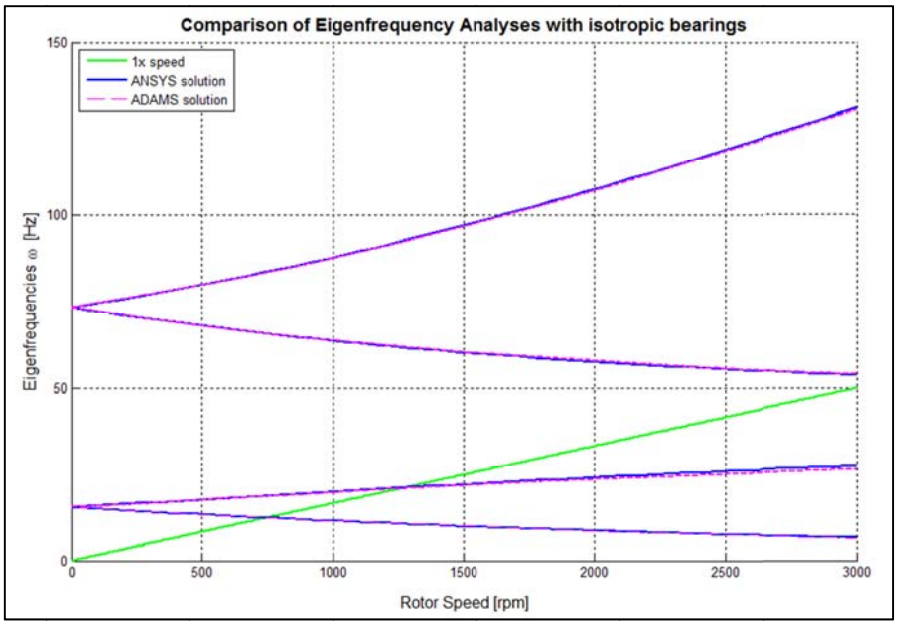

Figure 4.16: Comparison of eigenfrequency analyses with isotropic bearings

Figure 4.16 indicates that the change of eigenfrequencies over increasing rotor speed is the same in ANSYS and in ADAMS. The critical speeds can be identified at 735 rpm (12.25 Hz) and 1280 rpm (21.3 Hz). In order to support the results obtained with the eigenfrequency analyses, an unbalance response plot will be calculated in both applications.

Comparison of Unbalance Response

Possible vibration excitations of a rotating structure caused by the rotating velocity ω are most likely from the rotor's unbalance or coupling misalignment. While the unbalance excites a frequency spectrum from 1x the rotational speed, the coupling misalignment excites a spectrum of 2x the rotational speed. Because the maximum admissible unbalance force of rotating machinery is usually specified in design rules, it is common to do an unbalance response study during the design phase of a machine.

Due to the periodicity of the unbalance force, a harmonic analysis can be carried out in ANSYS. As stated in chapter 3.1.2 a harmonic analysis is a resonance study when the system is subject to cyclical loads ($\mathbf{f}_{(t)} = \mathbf{F}\, e^{j\omega t}$). This analysis technique calculates only the steady-state, forced vibrations of a structure. The transient vibrations, which occur at the beginning of the excitation, are not accounted for in a harmonic response analysis. Generally, all loads as well as the structure's response vary sinusoidal at the same frequency.

A rotational unbalance is defined as:

$$U = m_e\, e \tag{4.34}$$

where m_e is the eccentric mass and e is the distance between the eccentric mass and the rotation axis (Figure 4.17).

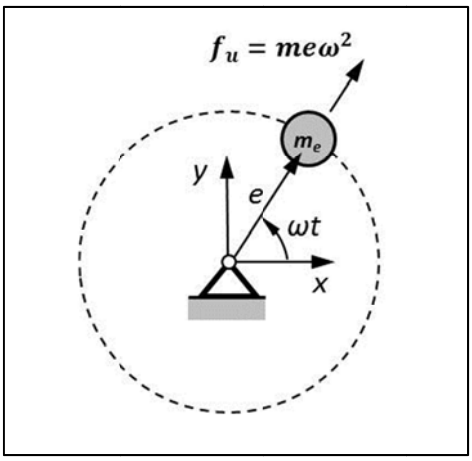

Figure 4.17: Unbalance force

Due to the rotating motion, the resulting unbalance force can be described in a x-y-coordinate system.

$$\mathbf{f}_{(t)} = m\, e\, \omega^2 \begin{pmatrix} \cos \omega t \\ \sin \omega t \end{pmatrix} \tag{4.35}$$

The unbalance for the analysis will be assumed with U=0.018 **k**gm. In ANSYS the complex rotating force is defined by applying U to the node at the disc's center point in x- and y-direction. After doing so, the harmonic analysis can be started (see Appendix).

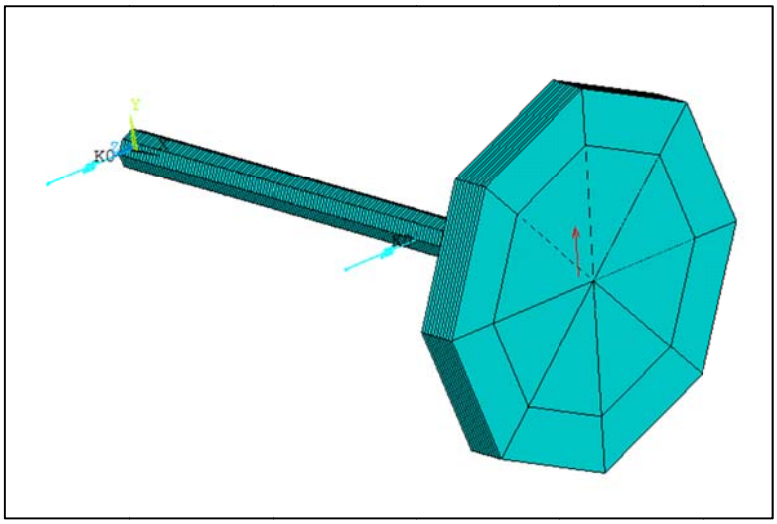

Figure 4.18: Overhung rotor model with applied unbalance force

In order to obtain the unbalance response in ADAMS with a transient analysis, an eccentric mass will be added to the disc. The eccentricity is assumed with e=0.25 m. Together with the given unbalance used in ANSYS of U=0.018 kgm, the unbalance mass results in m=0.072 kg. This mass is modeled as point mass, which is attached to the rotating system through a rigid joint on the interface node at the disc center (Figure 4.19).

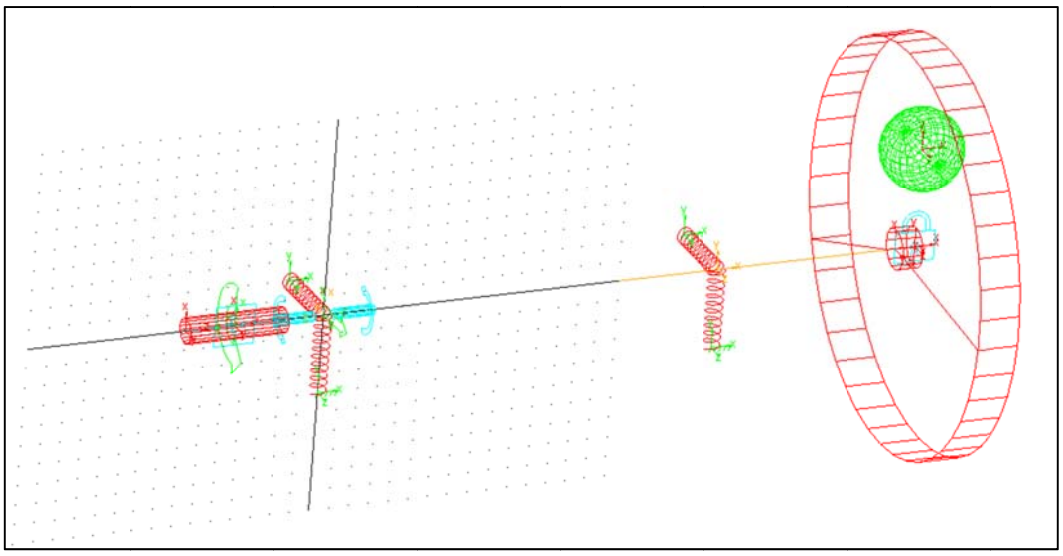

Figure 4.19: ADAMS model of overhung rotor with unbalance mass

As mentioned before, the harmonic analysis in ANSYS doesn't consider the transient vibrations, which occur at the beginning of the excitation. Thus, the transient run-up in ADAMS is performed stationary. This means the rotor gets a particular speed between 0 and 50 Hz assigned and its dynamic response due to the assigned rotational speed is simulated for 5s until a steady-state is reached. The resulting peak values of the cyclical displacements in the radial directions are measured at the front end bearing and can be evaluated. The step width for increasing the rotational speed is 0.5 Hz. After all displacement values are gathered, the results of the simulations in the time domain can be compared to the harmonic analysis.

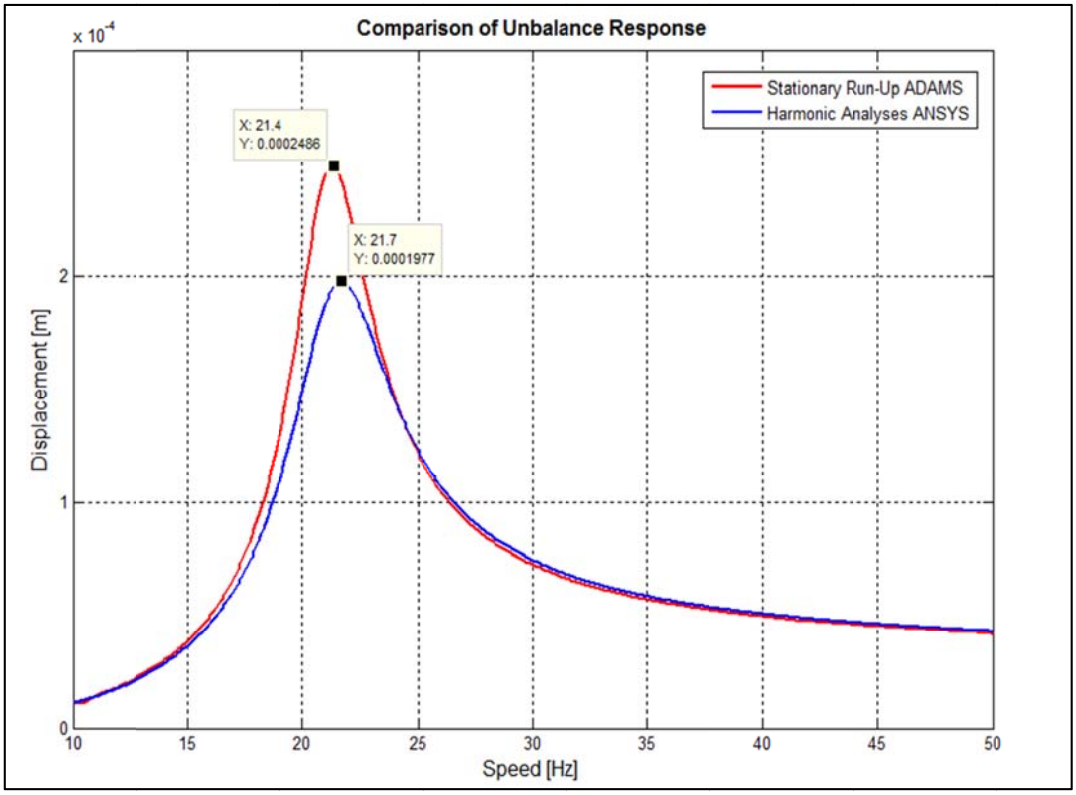

Figure 4.20: Comparison of unbalance response

The unbalance response function in ADAMS and ANSYS slightly diverge in the resonance region in terms of amplitude and frequency due to different damping principles in the computation methods. Further, the unbalance response computed in ADAMS shows its peak at 21.4 Hz, exactly where it was identified in Figure 4.16. An unbalance force cannot excite a backward mode when the system contains isotropic bearing stiffness. Consequently, the unbalance response plot (Figure 4.20) solely shows a resonance peak when the forward mode is excited. Overall, both calculations show similar results and converge before and after the resonance region very good.

4.6 Eigenfrequency Analyses with Anisotropic Bearing Stiffness

Regarding the examination of the influence of anisotropic bearing stiffness on the dynamic behavior of the rotor-bearing system, the horizontal stiffness of the front end bearing (Figure 4.12) is changed from 1e^9 N/m to 3e^7 N/m. All other bearing stiffnesses are held constant. The following diagrams show the comparison of the eigenfrequency analyses in ADAMS and ANSYS, as well the evaluation of the identified critical speeds with the harmonic analysis in ANSYS.

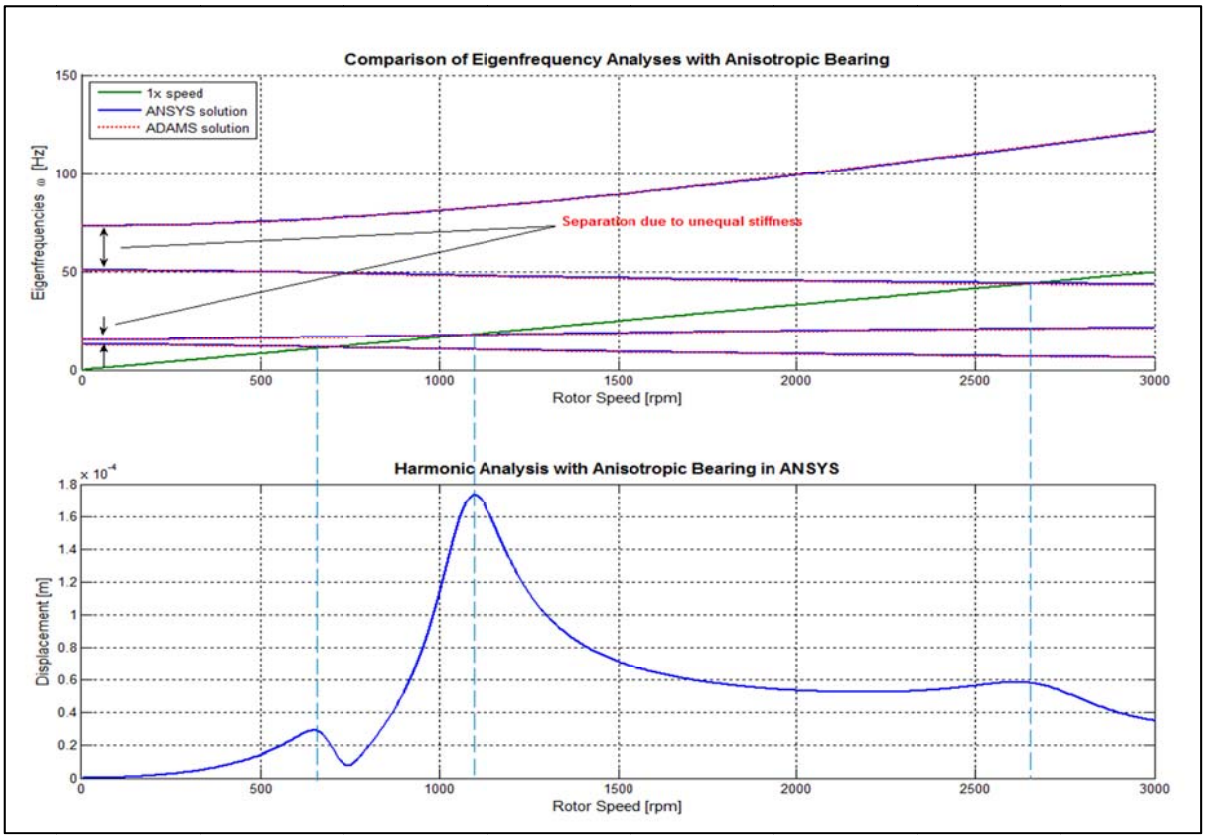

Figure 4.21: Eigenfrequency analyses with anisotropic bearings

The Campbell-plot of both, the FE and the MBS computation, show identical results and the same characteristics. The separation of the mode pairs due to the unequal stiffness of the front end bearing is reflected correctly in both simulations. Because the

backward mode of the second mode pair has shifted downwards, three critical speeds occur. The unbalance response plot of harmonic analyses in ANSYS shows peak amplitudes exactly at the critical speeds. Apparently, an intersection of the rotor speed with a forward mode leads to higher vibration amplitudes as opposed to the backward modes.

5 Simulation of Roller Bearings

The highly non-linear load distribution and the internal clearance in roller bearings have a significant impact on the dynamic behavior of the rotor-bearing system. Thus, the representation of the bearings as linear or non-linear springs or bushings is a strong abstraction of reality. By substituting the bearing system with this simplified modeling, the complex contact mechanics is generally modeled insufficiently, which often leads to conflicting data results between simulation and measurement. The first part of this chapter aimes to examine the internal load distribution of a roller bearing before conventional and new dynamic simulation approaches will be reviewed.

5.1 Static Load Distribution in Roller Bearings

The internal load distribution in roller bearings will be examined by assuming a pure radial load R applied on an ideal single-row bearing. Under the assumption of a zero clearance bearing with elastic rollers, the load distribution on the individual roller elements results from their elastic properties. As illustrated in Figure 5.1, the highest load acting on the rolling elements is in plane with the applied external force. Considering a static loading, the sum of all vertical load components of the stressed rollers equals the radial force ($R = \sum F_R^{(i)}$).

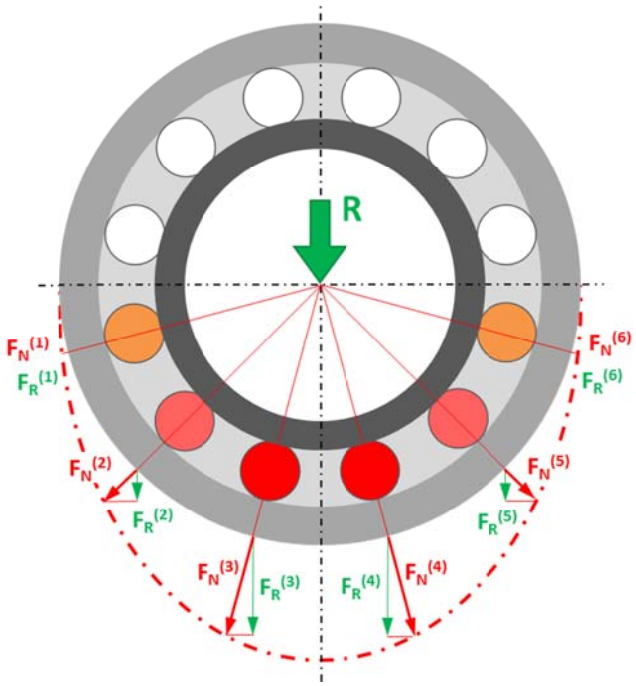

Figure 5.1: Internal load distribution in an ideal radial bearing

The loads carried by rolling-element bearings are transmitted through the rolling element from one race to the other. Apparently, the magnitude of the load carried by an individual rolling element depends on the internal geometry of the bearing and the location of the element at any instant.

The complex contact mechanics of elastic bodies was first described by Heinrich Hertz in 1882. He defined analytical expressions for stress maxima in terms of load for elastic bodies. The Hertzian law states that the shape and size of a developing contact area depends on the applied load, the elastic properties of the materials and the curvatures of the surfaces. The latter causes either a point or a line contact. Generally, the contact between two spheres will start with a point contact and through increasing load an elliptical contact area will develop, while the contact between two cylinders with parallel axes (Figure 5.2a) will result in a line contact and transform into an rectangular contact patch.

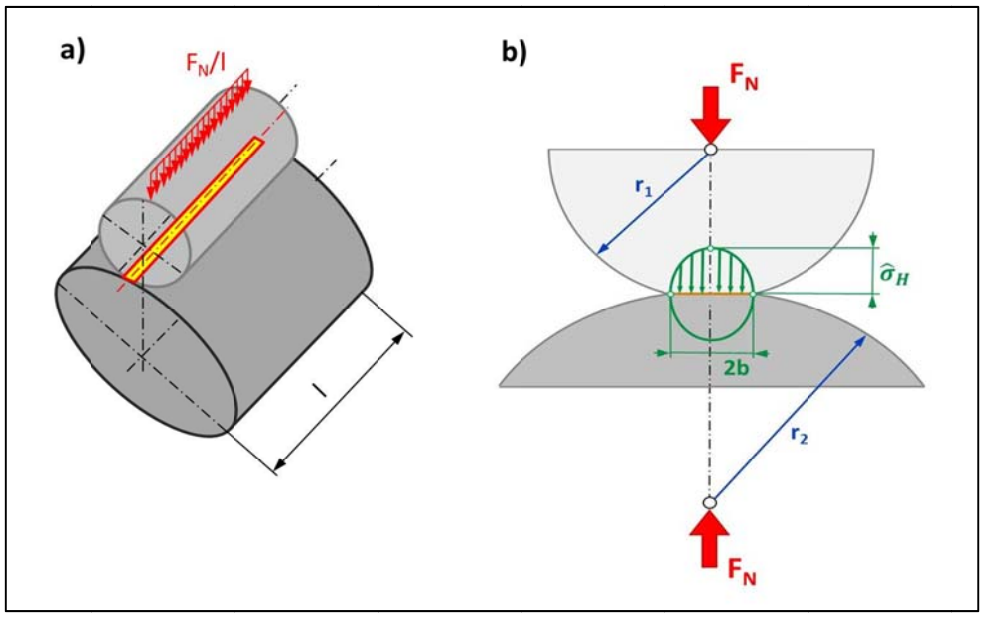

Figure 5.2: Contact between two cylinders with parallel axes (a) and resulting Hertzian stress (b)

For the example of the two cylinders pressed together in Figure 5.2b, the maximum Hertzian stress is defined as:

$$\hat{\sigma}_H = \sqrt{\frac{E'\,F_N}{2\pi\,R\,l\,(1-\upsilon^2)}} \tag{5.1}$$

where υ is the Poisson's ratio, the combined young's modulus is

$$E' = \frac{2E_1E_2}{E_1+E_2} \tag{5.2}$$

and

$$\frac{1}{R} = \frac{1}{r_1} + \frac{1}{r_2}\,. \tag{5.3}$$

By definition, the Hertzian stress is a compression stress on the contact area, with a resulting force equal to the acting normal force. Because the compression stress disappears at the edges of the contact patch and the stress maxima appears at the acting line of external force, an elliptical compression stress distribution over the width

of the contact area can be assumed. In general it is correct to conclude, that the bigger the contact area is due to the curvature, the less Hertzian stress occurs.

In addition to Hertz, Lundberg and Sjövall determined the contact deformation for an ideal line contact condition (Equation 5.4), while Palmgren developed a contact deformation equation (Equation 5.5), which also takes the crown of the roller into consideration [**12**].

$$\delta = \frac{2F_N(1-\upsilon^2)}{\pi E' l} \ln\left[\frac{\pi E' l^2}{F_N(1-\upsilon^2)(1 \mp \gamma)}\right] \tag{5.4}$$

$$\delta = 3.84 \times 10^{-5} \frac{{F_N}^{0.9}}{l^{0.8}} \tag{5.5}$$

Having an equation for the elastic deformation, a load-deflection relationship can be formed. In the general form it can be written as

$$F = K_j \delta^j \tag{5.6}$$

in which j=1.5 for ball bearings and 1.0 for roller bearings. By reforming this relationship the bearing stiffness can be calculated for any assumed radial load.

Radially loaded Roller Bearings with Radial Clearance[25]

In reality, rolling element bearings are not as ideal as assumed in the previous case. Virtually all of them are designed with a specific internal clearance in order to provide free rotation of the rolling elements, a compensation for thermal expansion and an optimum load distribution. Clearance, no matter how large, adds more non-linearity to the load-deflection relationship. A radially loaded roller bearing with a diametral clearance of $2 \times c_r$ is illustrated in Figure 5.3. In the concentric position shown in Figure 5.3a. a uniform radial clearance between the rolling elements and the races of c_r is evident.

[25] cf. [**18**] p.21ff

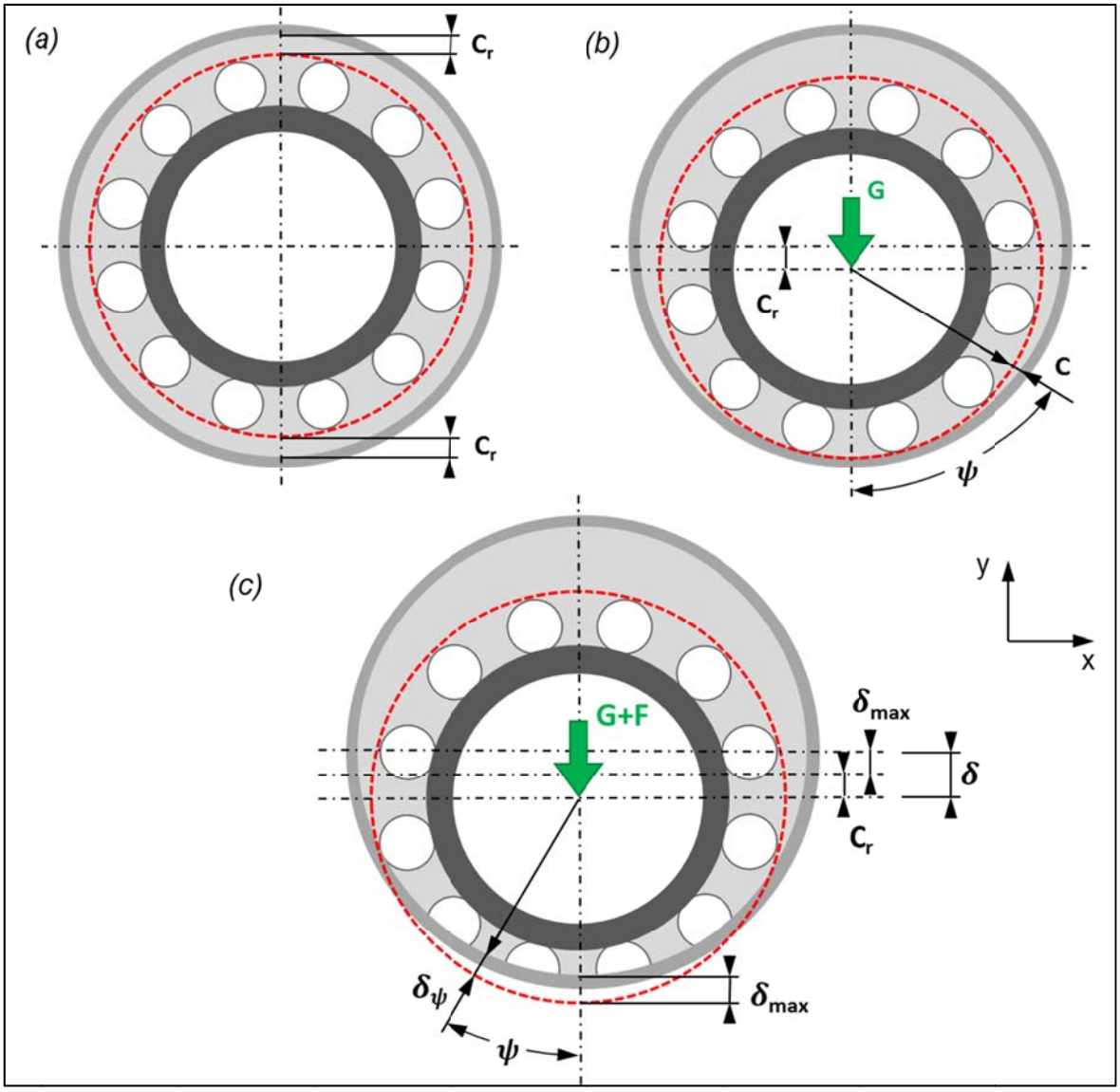

Figure 5.3: Radially loaded rolling-element bearing. (a) Concentric arrangement. (b) Initial contact. (c) Interference.

The application of a small radial load (G) to the shaft (or the shafts weight) causes the inner ring to move a distance c_r before contact is made between a rolling element located on the load line and the inner and outer races. At any angle, there will still be a radial clearance c that, if $2 \times c_r$ is small as compared with the radius of the tracks, it can be expressed with adequate accuracy by:

$$c = (1 - \cos\psi)\, c_r \tag{5.7}$$

On the load line where $\psi = 0$, the clearance is zero, but when $\psi = 90°$ the clearance retains its initial value of c_r. The application of further load (F) will cause elastic deformation of the rolling elements and the elimination of clearance around an arc of 2ψ. If the interference or total elastic compression on the load line is $\delta_{\max}$, the corresponding elastic compression of the roller δ_ψ along a radius at angle ψ to the load line will be given by:

$$\delta_\psi = (\delta_{\max} \cos\psi - c) = (\delta_{\max} + c_r) \cos\psi - c_r \tag{5.8}$$

This assumes that the races are rigid. Now, it is clear from Figure 5.3c that$(\delta_{\max} + c_r)$ represents the total relative radial displacement of the inner and outer races. Hence:

$$\delta_\psi = \delta \cos\psi - c_r \tag{5.9}$$

The relationship between load and elastic compression along the radius at angle ψ to the load is given by equation 5.6 as:

$$F_\psi = K_j {\delta_\psi}^j = K_j(\delta \cos\psi - c_r)^j \tag{5.10}$$

For static equilibrium, the applied load ($F_r = G + F$) must equal the sum of the components of the rolling-element loads parallel to the direction of the applied load.

$$F_r = \sum F_\psi \cos\psi = K_j \sum (\delta \cos\psi - c_r)^j \cos\psi \tag{5.11}$$

Through the analysis of the static load distribution under consideration of the radial bearing clearance, it becomes apparent that the load-deflection relationship shows strong non-linear behavior. Different stiffness diagrams in x- and y-direction must be taken into account when horizontal and vertical forces are acting. For example, if the shaft's weight already eliminates the radial clearance in y-direction due to gravity, the stiffness in y-direction will be much higher than in x-direction, where the load has to overcome the existing clearance first.

5.2 Modeling Approaches for Roller Bearing Dynamics

Rolling element bearings are systems in which various parts are interacting with each other. The past section introduced the complexity of load-deflection relationship without considering dynamics. In order to examine the dynamics of mechanical systems containing rolling element bearings and further the influence of these on the system, it is necessary to have a model which additionally takes the kinematics of the elements as well as dynamic loading into account. Increasing scientific research addressing the dynamics of roller bearings, especially ball bearings has been carried out since the Lundberg-Palmgren life prediction theory, published in 1947. An extensive amount of information and data on the performance of roller bearings is provided in manufacturers' catalogs. Most of these data is empirical in nature, obtained from the testing of products or from information in various standards publications (ANSI, DIN, ISO, etc.). Unfortunately, these information pertain only to bearing applications involving slow-to-moderate speed, simple loading, and nominal operating temperatures. Tedric A. Harris [**12**], a former managing director of the Engineering & Research Center at SKF and professor of mechanical engineering at the Pennsylvania State University, published in his book "*Rolling Bearing Analysis*" the principles of roller bearing design and operation. It provides the basic knowledge of roller bearings and contains also information for complex bearing applications and bearing performance analysis.

By reviewing scientific papers addressing the modeling of roller bearing dynamics it can be observed that the majority of them rely on the formulas presented by Harris and the Hertzian contact theory. Furthermore, the papers referring to nonlinearities in bearings can be basically grouped into the three major causes of

nonlinearity. These are the contact between the elements, the bearing clearance and the waviness or defects of the rings. The latter is the source for bearing induced vibrations which occur at a fraction of the nominal speed of the rotor. A detailed analysis of the waviness effects would go beyond the scope of the paper and is therefore assumed to be ideal for the bearing application in the refiner simulation.

The main emphasis of this work lies on adding bearing nonlinearities to the flexible multibody model through consideration of clearance and complex element contacts. Tiwari *et. al.* [**13**], [**14**] studied the effect of the ball bearing clearance on the dynamic response of a rigid rotor with a theoretical simulation model based on the Hertzian contact formulation and the ball bearing kinematics described by Harris. In [**13**], the varying compliance effect was the only excitation in the simulation model, whereas, in [**14**], unbalance was also included. The authors concluded that the radial internal clearance is an important parameter for determining the dynamic response, as they observed that with increase in clearance the regions of unstable and chaotic response become wider. Furthermore, the peaks developed from their simulation and experimental results shift down with the increase in clearance, which points to a decrease in the dynamic stiffness of the bearing. They also noted that the decrease in clearance increases the linear characteristics of the system.

Kappaganthu and Nataraj [**15**] analyzed a theoretical deep groove ball bearing model similar to Tiwari *et al.* and concluded that clearance is a practically important source of nonlinearity and has to be modeled accurately and in detail.

Mourad *et al.* [**16**] performed a theoretical and an experimental nonlinear stiffness ball bearing study in static and dynamic mode. Their theoretical study was also built up on the Hertzian contact theory. By comparing their analytical results with the ones from the simulation, they observed strong similarities but they also draw the attention to difficulties related to mechanical bearing testing devices.

In recent years the study of roller bearings became more and more influenced by the FEA. Though, the dynamic FE-simulation presents itself as computation intensive due the multitude of elements a roller bearing consists of. Combined with a rotor numerous of nonlinear contacts exist which rise the computation time more significantly. As a result, there is no procedure right now, how to simulate a high spinning dynamic system containing roller bearings to a satisfying extend with the FEA.

Scientific approaches to simulate roller bearing dynamics were also made by applying multibody simulation techniques in MSC/ADAMS. Fritz, Basler and Seemann [**17**] developed a ball bearing subroutine in ADAMS which allows to attach other parts to it. They modeled the bearing with several rigid elements (balls, races and cage), and connected them by constraints and forces. On basis of [**18**] they approximated the contact by a Hertzian contact. Unfortunately their model was only validated against a quasi-static model and not with measurements.

The first major commercial software provider which has recently developed an add-on plugin for its application is MSC. The new roller bearing plug-in for ADAMS is made to support the application engineer when it comes to the consideration of the bearing nonlinearities in a multibody simulation model. The next section will examine the necessary background in order to apply it to the multibody model of a refiner's rotating unit.

5.3 MSC/ADAMS Roller Bearing Plug-in

The ADAMS Bearing AT (**A**dded **T**oolbox) is designed to enable fast and accurate modeling of rolling element bearings. Fast modeling is possible by automated design, whereas accuracy is achieved by fine FE-meshes for deriving the compliances between ring and rolling element. Thus, the Bearing AT needs to access NASTRAN (FEA software by MSC) which means that an application of the Bearing AT automatically requires an installation of NASTRAN.

Upon completion of the installation of NASTRAN and the Bearing AT, the plug-in has to be activated in ADAMS under the main tab tools → plugin manager. After doing so, Bearing AT should be a fixed tab in the menu bar. Currently ball, roller and needle bearings are implemented in the plug-in. All input data for the bearings is in units of newton, millimeter, kilogram and seconds. However, the user can work with different units in ADAMS.

The modeling process consists of several steps as illustrated in Figure 5.4.

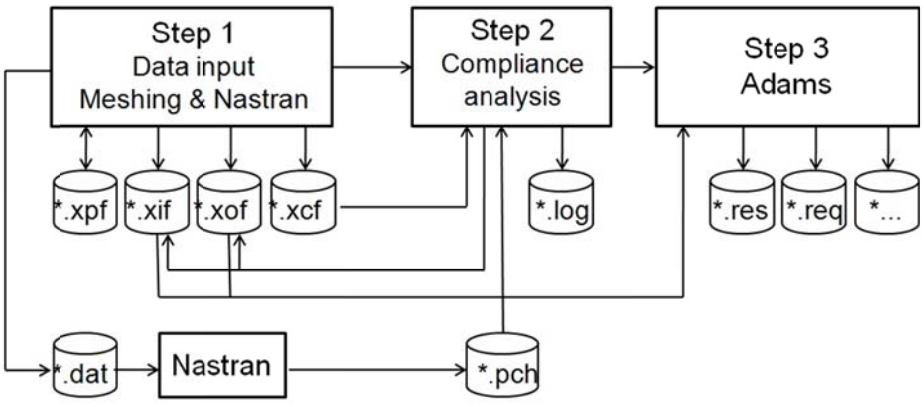

Figure 5.4: Bearing modeling process

In the first step the geometric and material data which defines the rolling element bearing can be inserted through particular masks for roller, rings and material, and are stored in the roller property file (*.xpf). Depending on the bearing type, 'x' will be

replaced by 'b' for a deep groove ball bearing, 'r' for cylindrical roller bearing and 'n' for needle bearing. After completion of all inputs, the user can proceed with the meshing. The built-in mesher of ADAMS Bearing AT reads the roller property file and creates NASTRAN input files (*.dat). Thereby, it utilizes symmetry in modeling the contact problem and creates only a quarter model of the rolling element and a section of the ring for inner and outer race. In a normal application, these NASTRAN input files are automatically submitted to a Nastran SOL101 analysis. The results of these analyses are stored under NASTRAN punch files (*.pch).

In step two the compliances of the rolling element against the ring are computed by a high performance contact algorithm. The contact processor takes the stiffnesses calculated in step 1 into account and builds up contact maps between the roller and the rings, which are used for interpolation in ADAMS. The user defines a maximum penetration for inner and outer ring, which represents the overlap between the rigid roller and the rigid ring. The user inputs are stored in the *.xcf file and as soon as the processing is started, a .log file will be created. The roller is than pushed in 20 steps into the ring to the maximum value of penetration (Figure 5.5).

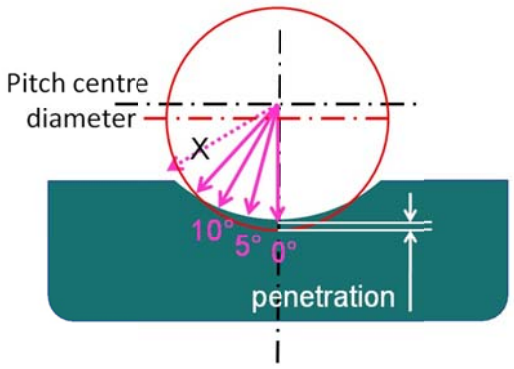

Figure 5.5: Compliance analysis

For ball bearings, the first compliance analysis starts in pure radial direction; subsequent analyses are rotated by 5 degrees till the direction of motion falls outside the race.

The compliance analysis for the outer and inner ring is in principle identical. The resulting compliance forces are stored in the *.xif file for the inner race and the *.xof file for the outer race.

After step 1 and 2 are completed successfully, the preprocessing is finished and the bearing can be implemented. The Bearing AT allows the user now to adjust the number of rollers compared to the input for the preprocessing and to add the total radial clearance. It has to be noted that the reference frame is coincident with the bearing coordinate system. The z-axis of this coordinate system represents the rotational axis.

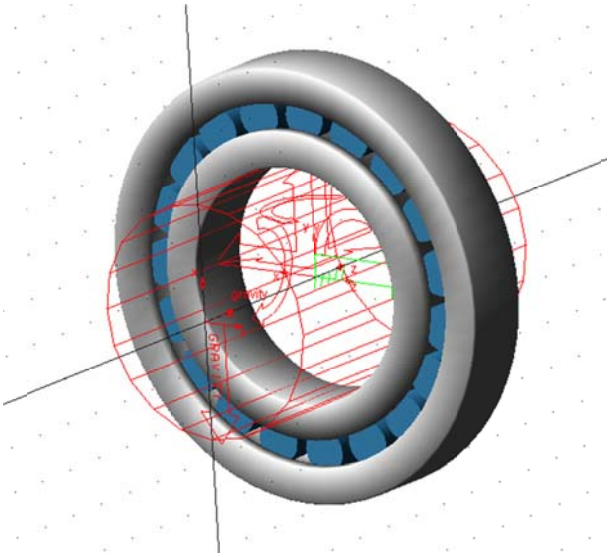

Figure 5.6: Roller bearing created with Bearing AT

Damping is also considered in the model. It is applied per ball, when the compression of the ball is increasing. The damping force is defined according to Equation 5.12.

$$Damping\ Force = Ball\ Load \times Compression\ Velocity \times Damping\ Factor \tag{5.12}$$

After the simulation a results file (*.res) of the bearing is created, which contains the acting forces and torques on the shaft as well as the movements of shaft. The request file (*.req) in contrast, contains the roller positions and loads.

6 Vibration Analysis of Rotating Machinery

In general a run-up or coastdown analysis is performed in order to analyze the vibration behavior of a rotating machine where vibration levels are changing with speed or time. The analysis of run-up or coastdown processes focuses on critical speeds, speed orders, instabilities of the rotor-bearing system and the detection of large speed ranges. The data acquisition is carried out by measuring accelerations in respect to the rotating speed of the machine.

The data analysis is usually attained by using the Fast Fourier Transformation (FFT) to transform the acquired acceleration signal from the time domain into the frequency domain. In general, the FFT assumes a stationary condition regarding amplitude and frequency and contains no time information of the signal. In case of a non-stationary signal, like the vibration change due to a speed change within the examined timeframe, the original spectral component will be diluted over multiple spectral lines. Instead of one intense spectral line, a number of lines with less intensity will emerge and be distributed over the frequency band. However, to overcome this problem a few analyzing methods have been established. In the following the two most suitable methods for the vibration analysis of the Andritz refiner will be introduced.

6.1 Cascade Analysis

A cascade analysis can be used to observe frequency changes versus rotational speed. The result is a cascade plot which consists of a series of spectra acquired at consecutive speeds, either increasing or decreasing (Figure 6.1). The rotational speed functions as the reference input of each, single acquired spectrum.

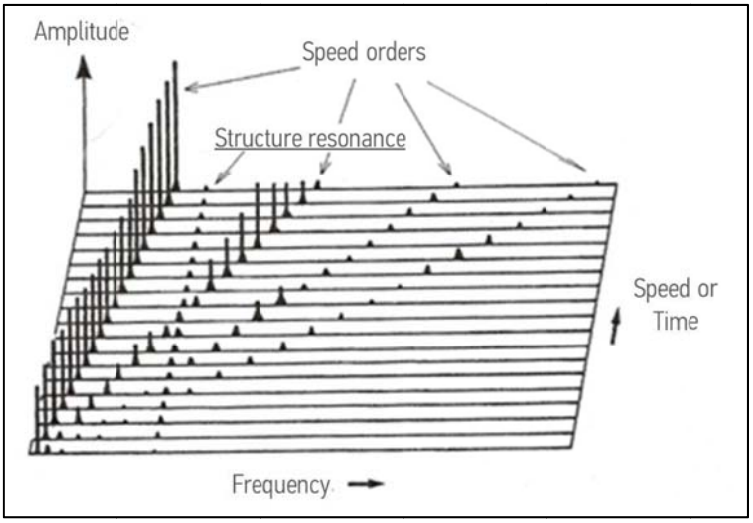

Figure 6.1: Cascade plot of a spectral range

Figure 6.1 shows that the speed independent structure resonances will occur within the same frequency channel when a speed dependent data acquisition is carried out. The speed orders run angular to them as they change for each speed. Order is defined as the normalization of the rotational speed. The first order is the rotational speed and order n is n times the rotational speed. In most cases the first order will be the most distinctive one. The first order and its subsequent harmonics are excited by different non-idealities of the dynamic system. For instance, first order components are excited through the unbalance of rotating parts and second order components are mostly excited by the shaft's misalignment. When a speed order crosses a structure resonance a resonance peak appears which indicates a critical speed of the machine.

Cascade plots can be acquired either manually or automatically. If the rotor speed of the machine can be manually held at specific speeds for sufficient time to acquire spectrum data, a cascade plot can be constructed consisting of spectrum plots in a multiple or stacked spectra format. Special software programs are available that provide the capability to record spectra during coastdown and display the data in a cascade plot format. Since significant time may be required to obtain a large number of spectra, the coastdown time of the machine must allow for data acquisition.

Another way to identify speed dependent vibrations is the spectrogram. It can be interpreted as the top view of the cascade plot, whereas the value of the amplitude is indicated with different color shades. The spectrogram represents a complete, two dimensional display of the course of spectra over time.

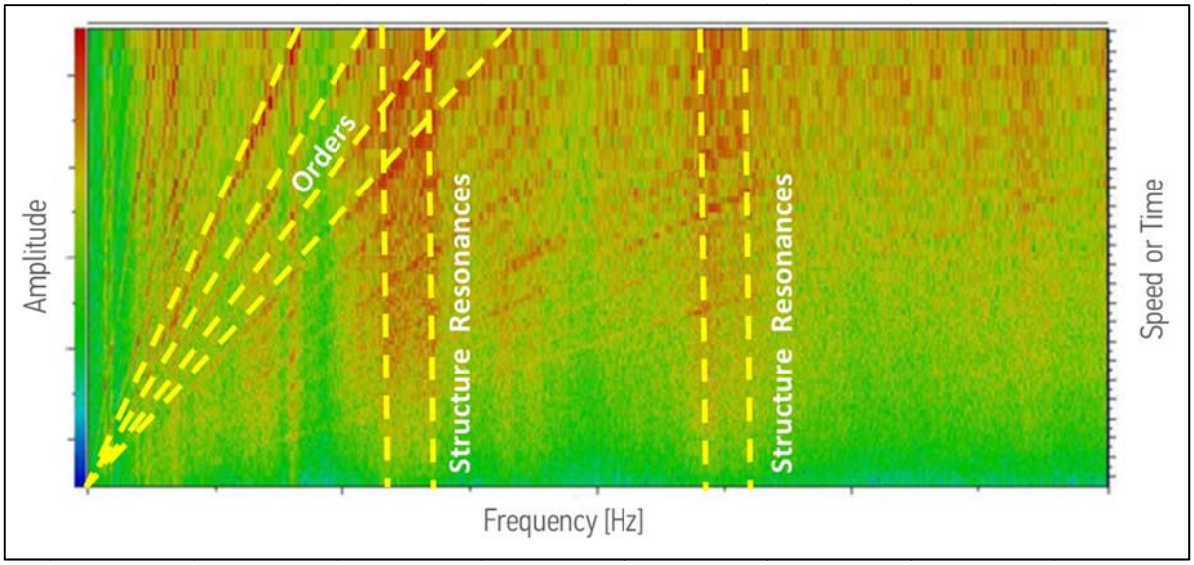

Figure 6.2: Spectrogram

Overall, cascade plots and spectrograms can reveal a resonant frequency too close to running speed, capture transient process disturbances, and record vibration magnitudes in relation to varying running speeds.

6.2 Order Analysis

Order analysis is a further powerful tool to study, design and monitor rotating or reciprocating machinery for which the rotational speed changes over time. Thereby, the time signal is provided digitally from independent, equidistant momentary values which are proportional to the rotation angle. The result of an applied FFT on this signal is a spectrum in dependence to an equidistant order axis. Therefore, the accrued spectrum is referred to as order spectrum. In most cases the speed reference is the rotational speed of the rotor.

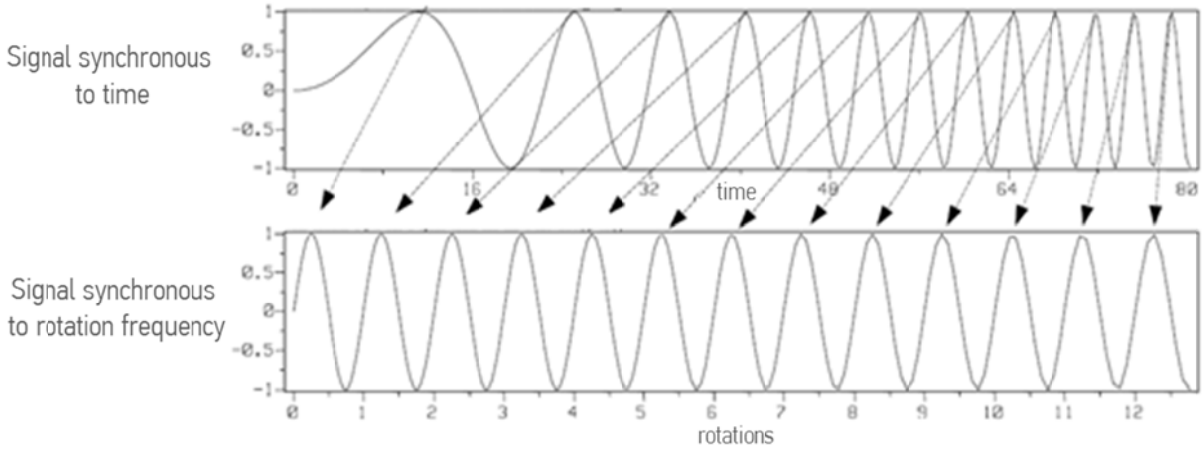

Figure 6.3: Rotating sampling rate[26]

Basically two methods have established for order analysis:

1. The data acquisition is triggered externally. This means, that the sampling points are controlled for instance by an incremental encoder, which delivers a constant number of impulses per rotation. This method raises particular requirements to the data acquisition hardware but results in a relative easy way to develop the spectra. A regular FFT can be used, which uses the sample points correlating to the rotor's rotation instead of the time (Figure 6.4).

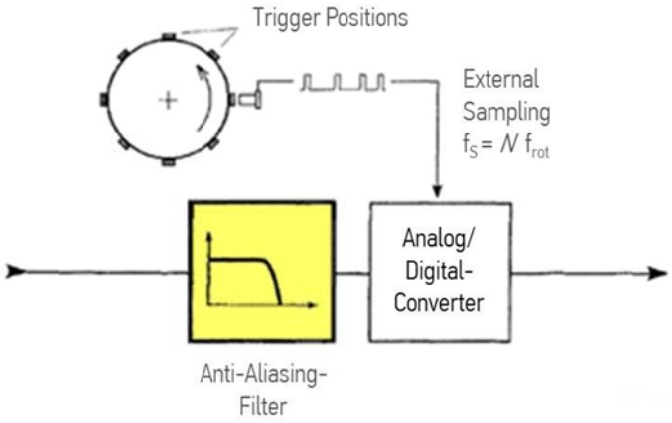

Figure 6.4: Synchronous sampling[27]

[26] c.f. [**23**]
[27] [**19**], p. 270

2. A time triggered data acquisition is executed with a high frequency rate, while the speed information is recorded simultaneously. Subsequently, the time signal is manipulated computationally by using the independent speed channel for the interpolation of a new speed dependent signal.

An order analysis can also be displayed with a cascade plot. As shown in Figure 6.5, the individual speed orders are the straight running peak rows, whereas the structure resonances are running elliptical.

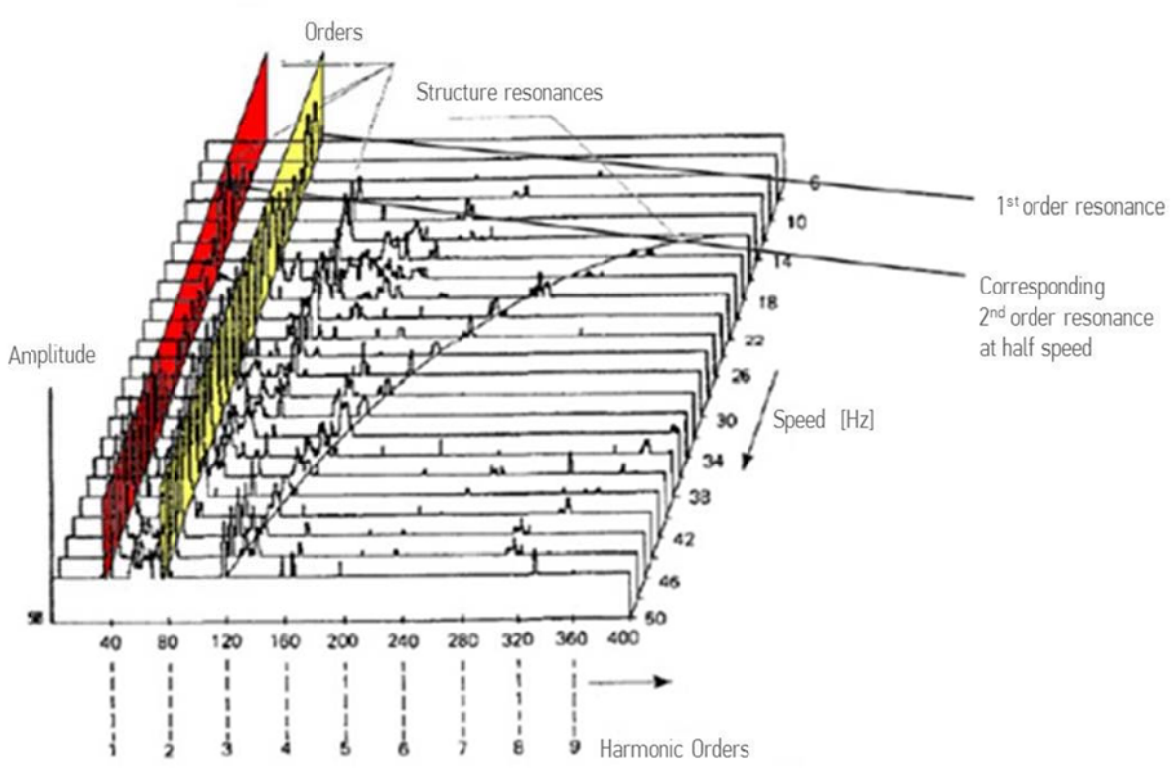

Figure 6.5: Cascade plot of a FFT order analysis[28]

[28] [**19**], p. 274

7 Study Structure Overhung Refiner

The examined refiner is a typical single disc (SD) refiner used in thermo-mechanical pulping processes. In refiner mechanical pulping, the raw material – usually in form of wood chips – is ground in the narrow gap between two metal discs with a grooved pattern. At least one of the discs is rotating with high speed. Figure 7.1 illustrates the principle involved.

The core components of a SD-refiner are the rigid and the rotating disc, both equipped with grinding plates on the face side. One of the discs can be axially adjusted in order to control the gap between the two discs. The gap is a key parameter within the refining process and is in the range of 0.1 – 2 mm, depending on pressure and type of wood. The axial movement is usually realized through hydraulic pistons or an electric motor with worm gear. Concurrently, the required axial grinding pressure is generated.

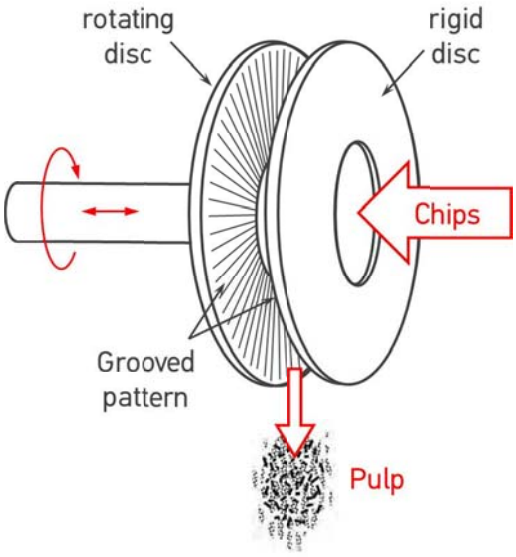

Figure 7.1: Principle of mechanical pulping with SD refiners

When entering into the refiner through the opening in the right disc in the picture, the chips are accelerated by the large bars near the center of the fast-spinning opposite disc. The chips start to rotate with the revolving disc and are simultaneously broken up to smaller fragments and fibers due to the heavy mixing and the abrasive action of the bars of the opposite disc. When these wood particles start to rotate with high speed, a considerable centrifugal force starts to act on them. Because of this centrifugal force, the wood raw material is pressed outward through the narrowing gap between the discs and is refined between the finer and finer structure of the grinding plates to a pulp of desired fineness. The residence time in the refining zone is less than a second.

7.1 Rotordynamic Analysis with linear substitute stiffness

The information about the rotordynamic behavior of the refiner is from significant importance for the machine's design. Especially critical speeds can have a negative impact on the operation when they are within the range of the operational speed. This chapter concentrates on the transformation of the ANSYS model to ADAMS, where the implementation of the newly developed subroutine for rolling element bearings (see chapter 5.3) can be realized with little modeling effort.

7.1.1 Analysis in ANSYS Workbench

First the refiner is modeled with ANSYS Workbench, similar to the modeling procedure of the simple overhung rotor in chapter 4.2.

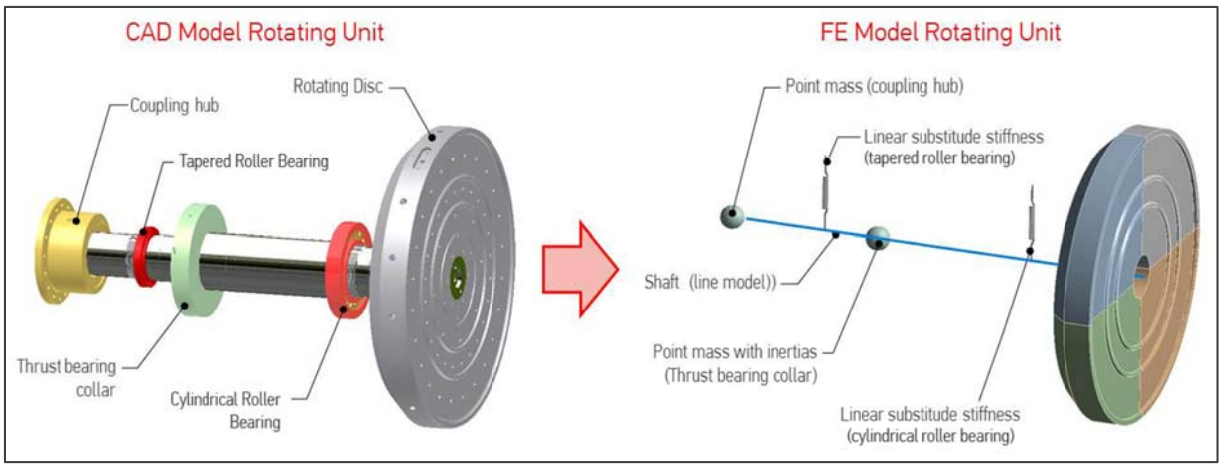

Figure 7.2: Transformation of the rotating unit from CAD-model to FE-model

The refiner shaft is modeled as a line model where each section has a different circular cross-section according to the geometric properties of the shaft. In doing so, the shaft can be discretized by using beam189 elements. The geometrical information of the different cross-section is assigned to the beam elements before the actual meshing procedure. The geometry of the rotor disc is imported as .step file from INVENTOR and meshed with solid186 elements. Refiner disc and shaft have the same material properties (steel; E=2.0 e^{11} N/mm^2; ρ=7850 kg/m^3; ν=0.3) and are connected through a rigid joint.

The influences of the coupling hub and the thrust collar of the thrust bearing, which are also parts of the rotating unit, are considered with mass elements, whereby inertias around all three coordinate axes are additionally defined for the thrust collar.

The support condition of the rotating unit can be implemented by joining the shaft to ground with two combi214 elements at the positions of the two radial bearings. Each element has stiffnesses defined for the two directions lateral to the shaft's main axis. These stiffnesses are a combination of the bearing stiffnesses provided by the manufacturer and the frame stiffnesses derived from the FE model of the support frame. Using linear stiffnesses for the frame as opposed to the entire model of it is feasible and leads to significant advantages regarding simulation time. In ANSYS

Workbench, the combi214 element is assigned to a longitudinal spring by using commands. The stiffness properties given for the cylindrical roller bearing and the tapered roller bearing are summarized in Table 7-1.

	Cylindrical Roller Bearing[29]	**Tapered Roller Bearing**
Vertical Stiffness [N/m]	2.56 e^9	6.0 e^9
Horizontal Stiffness [N/m]	5.4 e^8	6.0 e^9

Table 7-1: Bearing properties provided by manufacturer

As described in chapter 5.1, rolling element bearings do not have a constant stiffness for the entire circumference. The stiffness of the bearings depends to a high degree on the applied load and the bearing clearance. Table 7-1 shows a significant higher stiffness rate in vertical direction for the cylindrical roller bearing. This difference results because the weight of the rotating unit distributes the static load to the lower half of the bearing and eliminates the bearing clearance as illustrated in Figure 5.3. For the tapered roller bearing a simply isotropic stiffness is assumed as the bearing is pre-stressed. This assumption is acceptable because the superposition principle is applicable for the radial force and the axial force of the pre-load. The resulting force eliminates the complete radial clearance and all rolling elements contribute to the load transmission.

The stiffness data for the support frame is obtained by applying a general force at the bearing positions in the FE model and measuring the resulting displacements. Out of the linear relationship between $F = K \cdot U$, the stiffness can be calculated. The frame is modeled with a young's modulus of $E_{frame} = 1.7$ e^{11} N/mm^2 for cast iron.

[29] One-sided bearing clearance of 110µm

Frame Stiffnesses out of Finite Element Model	
Horizontal Stiffness Feed End Bearing [N/m]	6.1 e^8
Vertical Stiffness Feed End Bearing [N/m]	8.5 e^8
Horizontal Stiffness Drive End Bearing [N/m]	1.2 e^9
Vertical Stiffness Drive End Bearing [N/m]	3.1 e^9

Table 7-2: Frame stiffness out of finite element model

As all linear substitute stiffnesses for the bearings and the frame are available, the combined stiffness can be calculated. Therefore the springs are connected in series as illustrated in Figure 7.3. The resulting combined stiffnesses for the feed end (FE) and the drive end (DE) bearing are shown in Table 7-3.

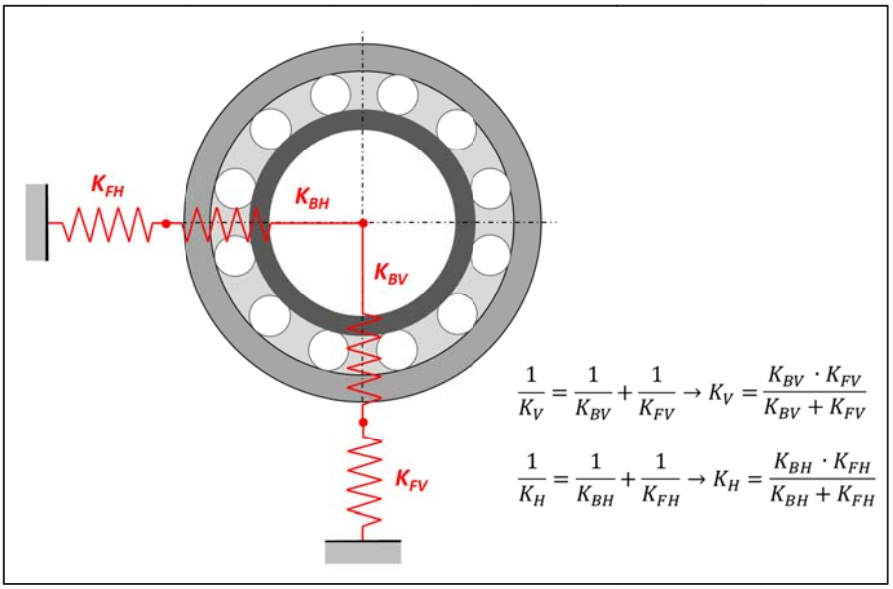

Figure 7.3: Combining of bearing and frame stiffness

Combined Bearing Stiffnesses	
Horizontal Stiffness Feed End Bearing **FE_H**[N/m]	2.86 e^8
Vertical Stiffness Feed End Bearing **FE_V** [N/m]	6.38 e^8
Horizontal Stiffness Drive End Bearing **DE_H** [N/m]	1.0 e^9
Vertical Stiffness Drive End Bearing **DE_V** [N/m]	2.04 e^9

Table 7-3: Combined bearing stiffnesses

After the combined bearing stiffnesses are defined for the combi214 elements, the geometry is meshed and the kinematical border conditions are defined. In case of the refiner model, the displacements along the rotating axis are constrained. Subsequently the rotordynamic analysis can be started. Thus, commands have to be added to the modal analysis for the computation of eigenfrequencies for different rotational speeds and the Stationary Reference Frame has to be activated.
The course of the first four eigenfrequencies of the rotating unit is displayed in the Campbell Diagram in Figure 7.4.

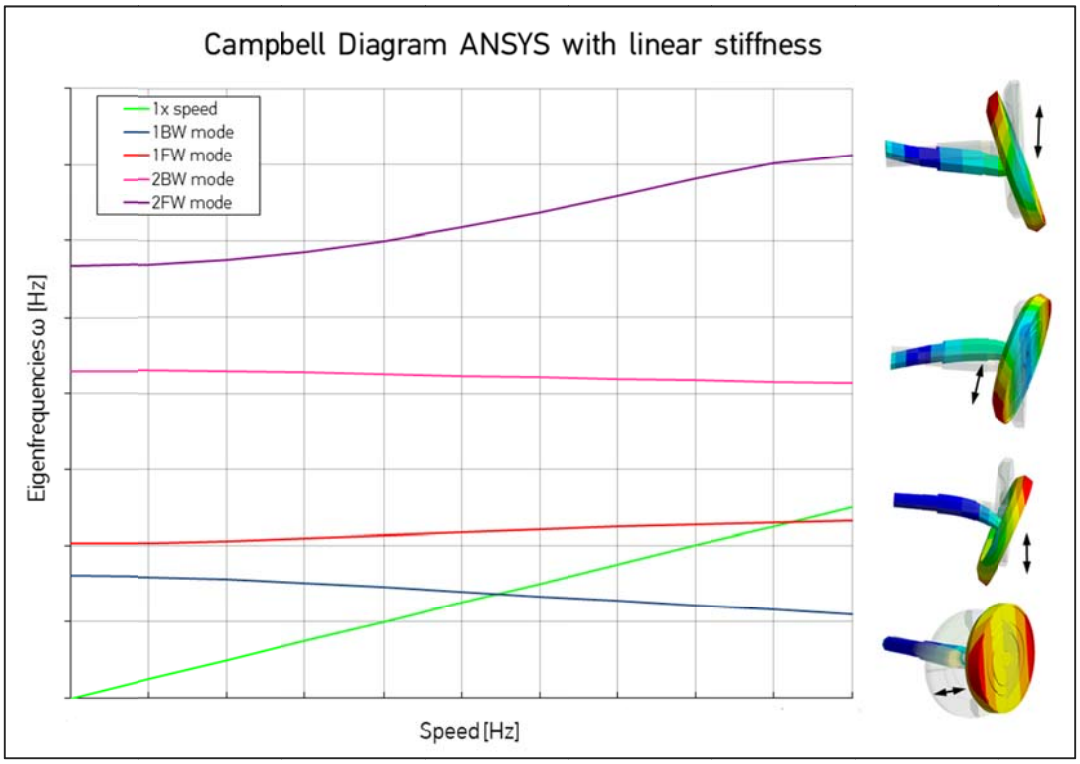

Figure 7.4: Campbell Diagram of first 4 eigenmodes out of ANSYS modal analysis

7.1.2 Analysis in ADAMS

In order to perform a multibody analysis of the rotating unit in ADAMS the flexible structure of the shaft has to be integrated in the MBS environment. The rotor disc can be considered rigid and only the mode shapes of the flexible shaft are needed.

Hence, the rotor shaft is modeled in ANSYS Classic the same way as in ANSYS Workbench. A line model is created and the cross-section information is assigned through beam189 elements. Before the ANSYS-ADAMS interface is used to create the modal neutral file (.mnf), which contains the free-free eigenmodes of the structure, the interface nodes have to be defined. It is important to specify all points where other parts are acting, forces are applied and constrains are set. For the examined refiner, these points are the center of the refiner disc, the center of the thrust collar, both points where the FE- and DE-bearing are acting and the connection to the coupling hub. For the computation of the .mnf-file the number of eigenmodes to extract is set to 20 and it has to be assured that no forces and constraints are defined. The resulting file of the flexible shaft can then be easily imported in ADAMS and is automatically aligned in the x-y-z global coordinate system as it was modeled in ANSYS. In order to consider all dynamic properties of the flexible body, the inertia modeling of the part must be set to "Full Coupling". Due to the modeling with beam elements, the shaft appears as line model.

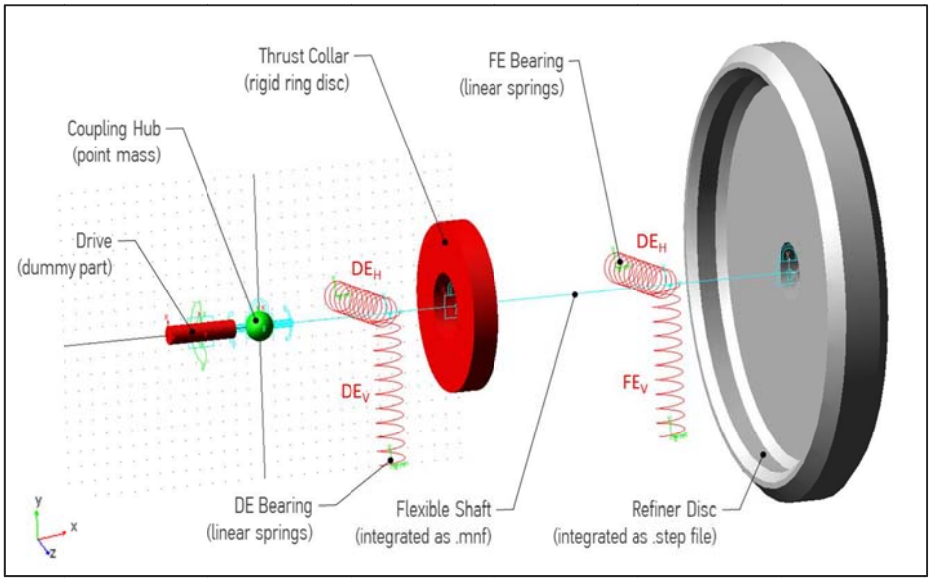

Figure 7.5: MBS-Model of the rotating unit with linear bearings stiffness

Figure 7.5 shows the MBS model of the rotating unit with linear bearing stiffnesses. The steps listed in the following describe the modeling process:

- After the flexible shaft is integrated as .mnf-file, the refiner disc is implemented as .step-file. For the correct positioning of the disc, the disc's center marker is aligned with the foremost interface node and rigidly joined to the flexible shaft. By assigning material properties to the geometric part, the corresponding mass and inertias are calculated automatically by the program.
- Next, the thrust collar is modeled according the geometric data as a rigid ring disc and connected through a fixed joint to the designated interface point.
- The bearing constraints are realized via linear springs with constant bearing stiffnesses according to Table 7-3. They act between the interface nodes and ground markers.
- The coupling hub is modeled as a simple sphere with the same defined mass of half the coupling as in ANSYS.
- The actuator for the rotating motion is a dummy part without mass and inertias, and connected to ground by a revolute joint. The rotating motion is transferred from the drive to the shaft by a constant velocity joint.
- Despite the coupling between the shaft and the actuator, a rotational velocity initial condition (IC) has to be defined for the flexible body so that the rotating motion of the shaft follows the motion of the actuator with little settling time. This condition basically sets the rotating motion to the same initial rotational speed of the actuator.
- For simplification reasons, a general variable containing the desired rotational speed in Hertz is determined and assigned to the drive and the shaft's IC.

- The support effect of the thrust bearing must not be neglected. Therefore a point motion is applied to the interface node of the thrust collar, which constrains the movement in direction of the rotation axis.

The MBS Campbell-Diagram is acquired through a stationary run-up, whereby an eigenvalue computation is started for each velocity step. Figure 7.6 displays the resulting diagram in comparison to the obtained results from the FE-Simulation.

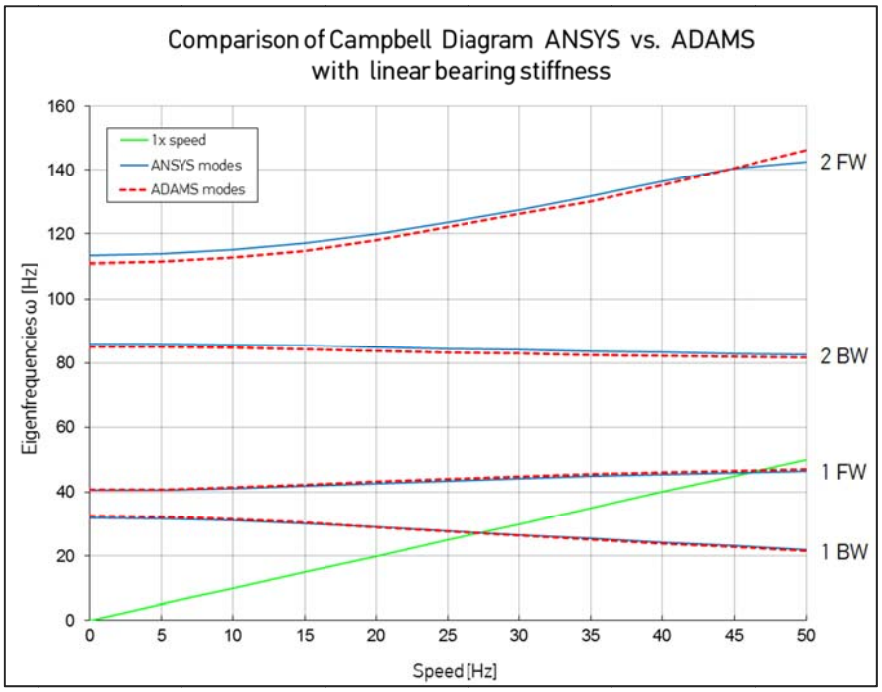

Figure 7.6: Comparison of Campbell Diagram ANSYS vs. ADAMS

Through the assessment of the Campbell Diagrams resulting from frequency analysis in ANSYS and in ADAMS it can be concluded that the dynamic behavior of the models is identical. Only the 4th mode of the rotating unit shows a slight difference but as the operating speed only crosses the first and second mode, the small shift is from little significance.

One very important note in relation to the computation of the linear modes for rotordynamic problems in ADAMS must be made at this place. The gyroscopic effects

of the overhung structure only occur when the FORTRAN solver is used. Even though the C++ solver is very powerful in the time domain it does not include the gyroscopic effect in the eigenfrequency characteristic correctly.

Simulation Settings for Eigenvalue Computation in ADAMS		
Executable Solver	FORTRAN	
Dynamic Solver	GSTIFF I3	
	Error=$1e^{-2}$	Hmax=$1e^{-3}$
Step Size	0.01 s	

Table 7-4: Simulation settings for eigenvalue computation

As the equality of the ADAMS and ANSYS model in terms of dynamic behavior can now be guaranteed, the drive mechanism of the system will be modified to fit the real design condition in the next step. Because the coupling hub allows the shaft to move in direction of the rotating axis and the drive shaft can only transmit rotational motion and constrains the translational movements of the shaft's interface point for the current model, an alteration of the actuator is necessary. Thus, two massless, cylindrical parts are added to the system and coupled with a translational joint which allow the shaft to move back and forward.

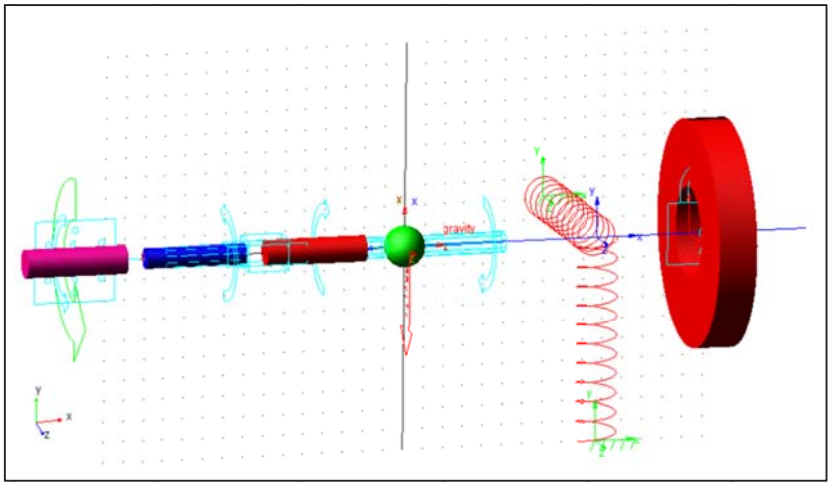

Figure 7.7: Modified actuator arrangement

In the new drive arrangement, illustrated in Figure 7.7, the pink cylinder with the rotating motion represents the drive shaft which transmits the rotational velocity to the blue cylinder via a constant velocity joint. The blue body in contrast is coupled with a translational joint to the red cylinder assuring adjustments in direction of the x-axis. At last, the red cylinder transmits the rotating motion to flexible shaft using a constant velocity joint.

Consequently to the system modification a new frequency analysis is essential. The analysis is performed exactly the same way as described earlier and Figure 7.8 contains the results compared to the previous model. The impact of the drive alteration shifts the first two eigenfrequencies slightly upwards, whereas the eigenfrequencies of the second mode pair are little lower in relation to the results of the model with the simple drive.

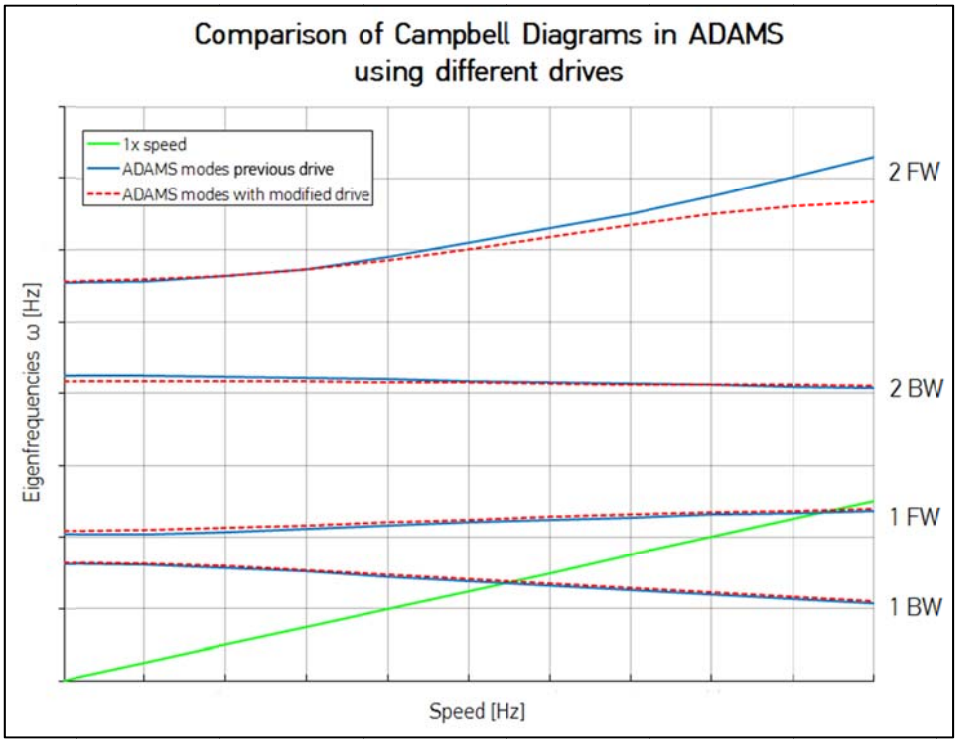

Figure 7.8: Comparison of Campbell Diagrams with different drives

The main purpose of using a MBS for the computation of the system's dynamic behavior is to take advantage of the calculation in the time domain. While critical speed ranges can be clearly identified in the frequency domain with the Campbell diagram by looking at the intersections between rotor speed and eigenfrequencies, the idea of an analysis in the time domain is to excite the systems natural frequencies through an additional unbalance. Thus, a very small unbalance is added to the refiner disc of model, which triggers the excitation of the eigenfrequencies during a run-up. The peak responses of the displacements of the interface node of the feed end bearing should indicate the critical speeds in the unbalance response plot.

Because the displacement amplitudes are very sensitive regarding the input energy of the unbalance weight and the damping of the flexible shaft, the unbalance weight has to be from low value and a damping function is required. These measures are necessary in order to obtain acceptable results and an efficient simulation time.

Simulation Settings for Unbalance Analysis		
Damping function of the flexible shaft	STEP(TIME,0,100,1,0)+ STEP(FXFREQ,1000,0.02,2000,1.0)	
Motion function for run-up	2*pi*rpm+2*pi*time	
Executable Solver	C++	
Dynamic Solver	HHT I3	
	Error=$1e^{-4}$	Hmax=$1e^{-5}$
Step Size	0.001 s	

Table 7-5: Simulation settings for unbalance analysis

The damping function noted in Table 7-5 is assigned to the flexible shaft and causes a strong damping of the initial displacement amplitudes due to the impacts of gravity and further damps all free-free natural frequencies of the shaft beneath 1000 Hz with a factor of 2% before it changes slowly to 50% at 2000 Hz. The motion function is

defined for the drive shaft and determines that with each second of simulation the rotational speed rises by 1 Hz. The general variable *rpm* holds the initial speed of the shaft and is set separately.

The results of the run up simulation are compared to the eigenvalue analysis in Figure 7.9. The frequency analysis leads to the identification of critical speeds at 2.0 and 3.46, whereas the unbalance weight excites the eigenfrequencies at 2.04 and 3.5. With a divergence of less than 2% to each other, both methods can be considered acceptable for the computation of critical speeds.

However, the quality of a simulation can only be determined by comparing its results to measurements. Hence, a vibration measurement on the refiner is carried out in the next chapter.

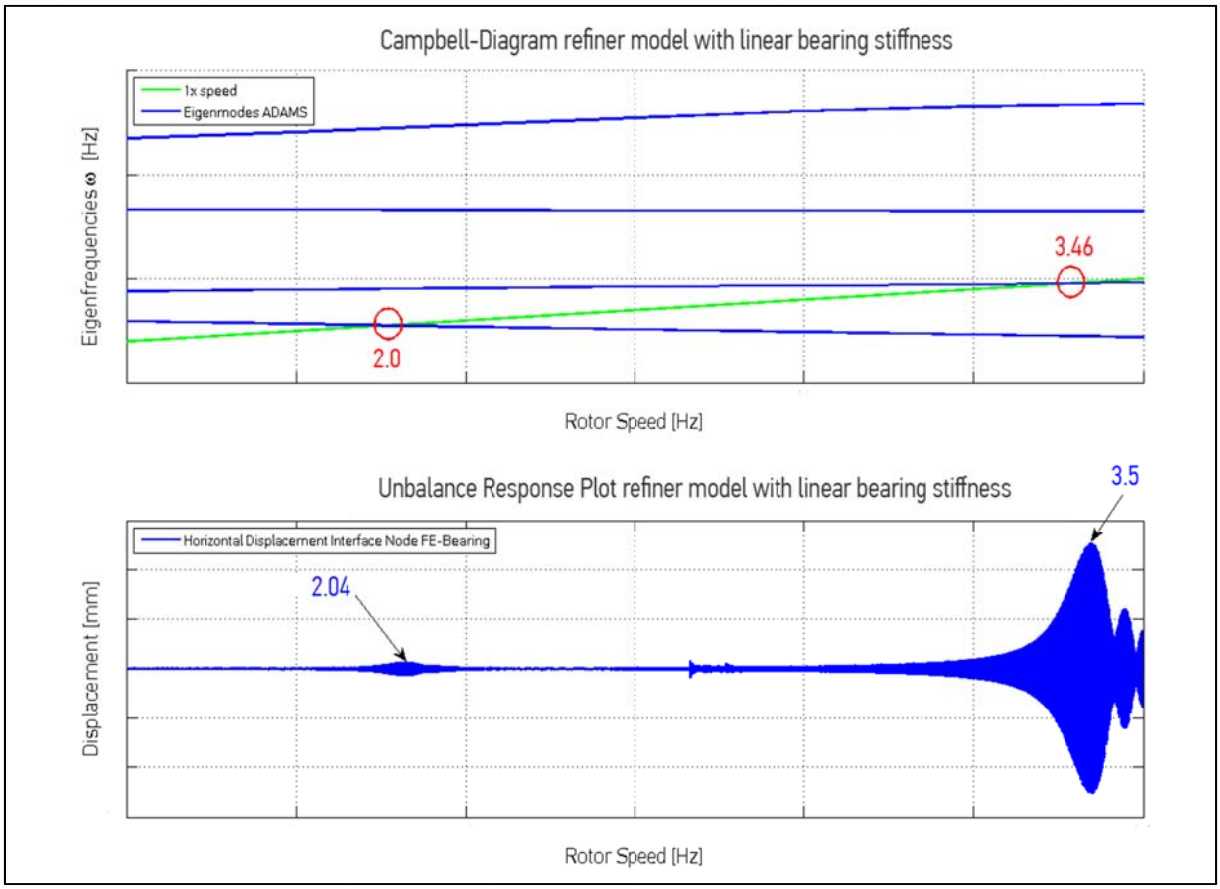

Figure 7.9: Comparison of Campbell diagram and unbalance response plot

7.2 Vibration Measurements on the Refiner

7.2.1 Measurement Procedure

Basis of the vibration analysis are two test runs with the refiner on the Andritz refiner test stand. Thereby the dynamic behavior is measured by:

- a stationary run-up test,
- a coastdown and
- a continuous operation run.

The accelerometer probes for the vibration measurements are mounted on four housing positions close to the DE- and FE-bearing. The vertical and horizontal accelerations are recorded independently for both bearings using a two-channel measurement. The signal of the rotational speed is detected by an optical incremental encoder pointing to the motor shaft. All measurement data is acquired with the CSI 2130 Machinery Health Analyzer from Emerson Process Management. The detected accelerations are automatically integrated and captured as effective velocities. All measurement data is captured for refiner configurations with and without main grinding plates mounted on the refiner disc. Because the simulation results are obtained without considering the weight of the main grinding plates, the focus lies on the related measurements.

As noted in chapter 6, vibration tests on rotating machinery require a run-up or coastdown test. In order to perform the run-up test, the rotating speed of the refiner is slowly increased via frequency converter and the accelerations are detected at each incremental step. The coastdown test is performed directly after the run-up, by turning of the motor power at the highest measured run-up speed. Through coasting to standstill the rotors' unbalance excites all frequencies and resonance frequencies can be detected. Further, order analysis techniques are used to analyze the vibration signals.

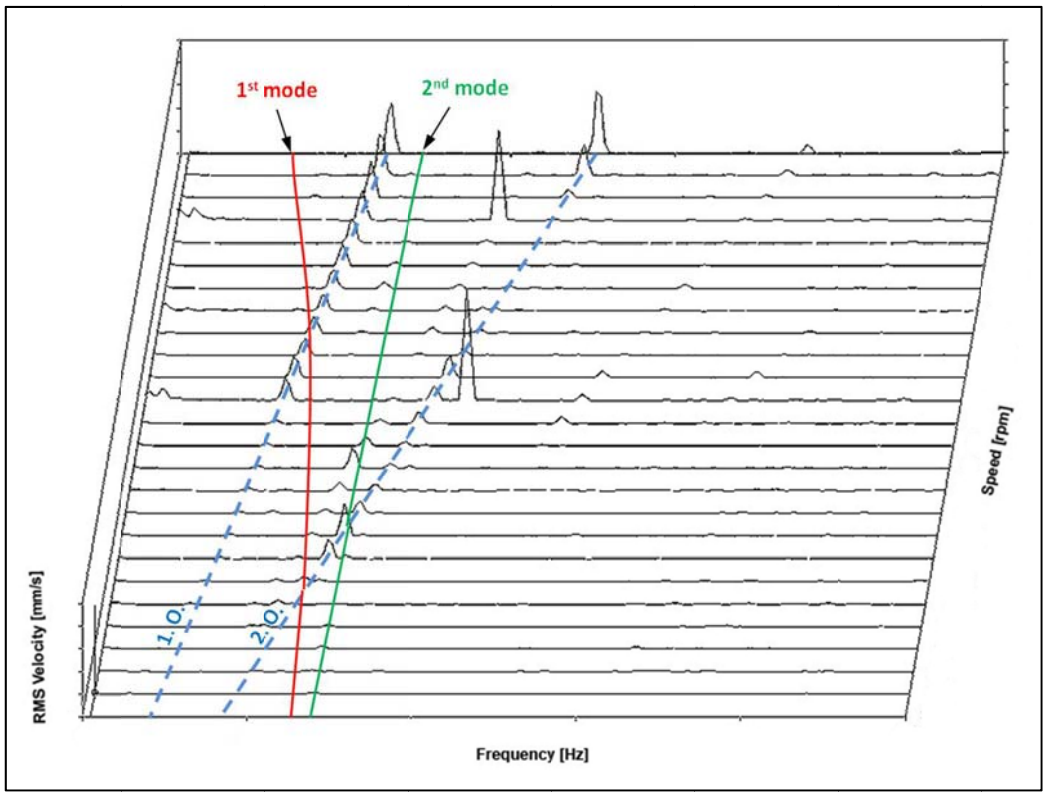

Figure 7.10: Waterfall plot of run up test with main plates

Figure 7.10 shows all measured spectra related to speed of the run-up test with main plates. It is a rough approximation of a waterfall diagram. 1st and 2nd order of the rotational speed can be clearly identified and are indicated in blue. The first order is the rotational speed and the second order is two times the rotational speed. Normally the first order is excited by the rotor's imbalance while misalignment excites 1st and 2nd order components. The red and green lines show the assumed development of 1st and 2nd mode.

Considerations regarding measurement procedure:

1. Previous data from run-up tests with other Andritz refiners with overhung design as well as various FE-Simulations of these machines show that the frequencies of the 2nd mode (vertical, FW) are higher than the operational speed of the refiner. Thus the rotor's unbalance will not excite the 2nd mode.

2. Due to the orthogonal anisotropic bearing stiffness of the refiner support, the whirl is always a superposition of a backward and forward motion. This means that there is no strict separation between forward and backward modes and each mode contains forward and backward components. As described in rotor dynamic theory unbalance will just excite the forward whirl, but due to the superposition the backward modes become also resonant.

Taking the two considerations into account, the focus of the 1st order analysis lies on the excitation of the first mode (horizontal, BW), which is indicated with the red line in Figure 7.10. A further obvious conclusion out of Figure 7.10 is that a 2nd order trace will cross the 1st and 2nd mode.

Unfortunately it is not possible to make a complete order analysis with the current licensed operating system on the CSI 2130, but it is possible to trace single order components for a coastdown. As a result the coastdown tests for the measurements with and without main plates are performed two times, first by observing the 1st order and second by observing the 2nd order.

7.2.2 Measurement Results

A review of run up and coastdown results leads to the interpretation that the coastdown results for 1st and 2nd order trace are more accurate and reliable than the run up results due to the continuity of the test. Hence, only results of the coastdown measurements will be shown in the following. It has to be noted that the coastdown measurement is only performed on the feed end bearing housing.

1st order Coastdown without Mainplates:

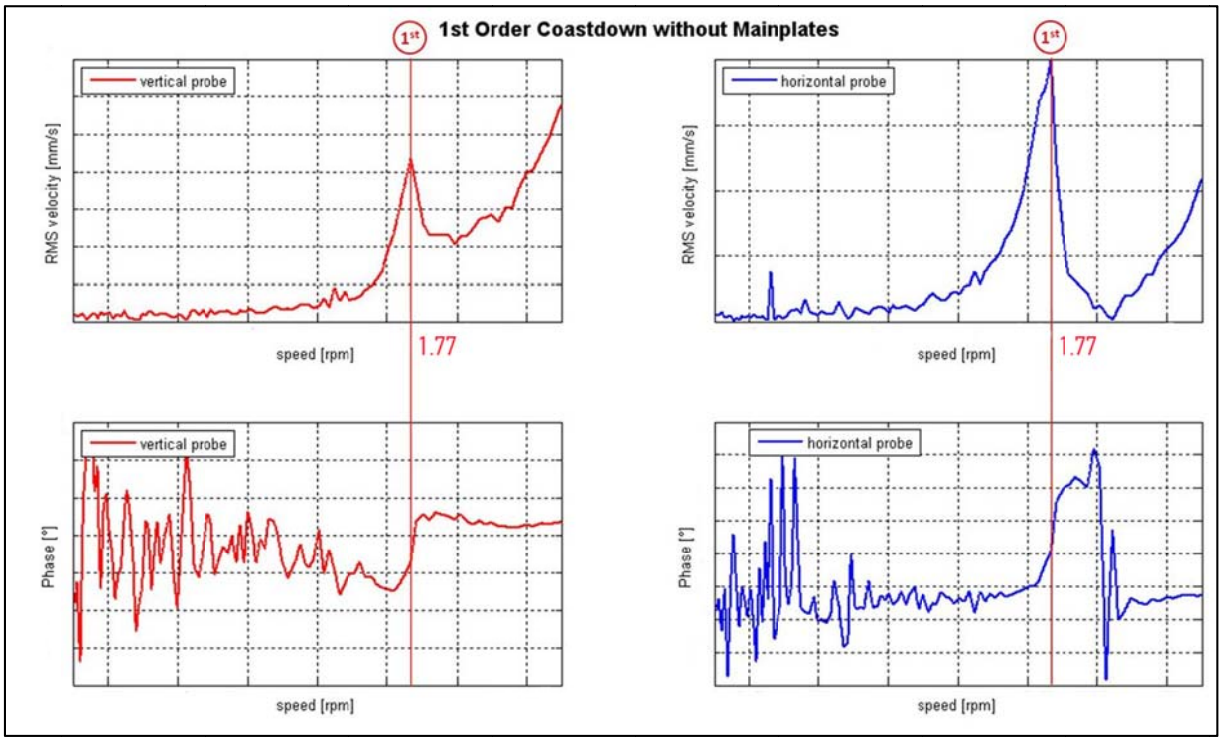

Figure 7.11: 1st order trace of coastdown without main plates

The 1st order trace of the coastdown without main grinding plates shows a significant resonance peak as well as a characteristic phase shift at 1.77 for both measurements. These are typical indicators for a resonance frequency. The comparison of the horizontal and vertical vibrations (see Figure 7.12) illustrates a higher horizontal amplitude, which is evidence for an horizontal (BW) mode.

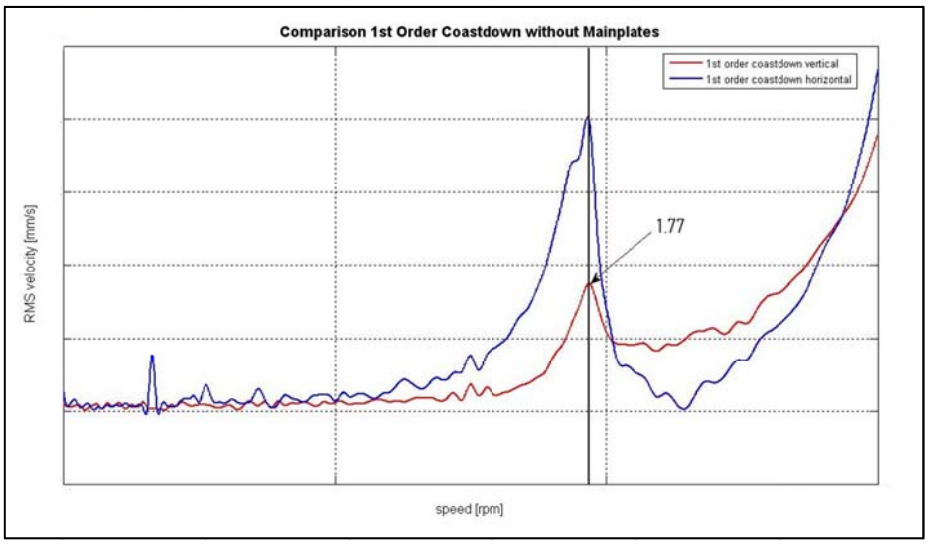

Figure 7.12: Comparison of vertical and horizontal amplitudes for 1st order trace

2nd order Coastdown without Mainplates:

The 2nd order trace shows several resonance peaks, whereat the 1st and 2nd rise will be analyzed in detail. Both resonance peaks at 0.91 and 1.29 have distinct phase shifts which are indicated in Figure 7.13.

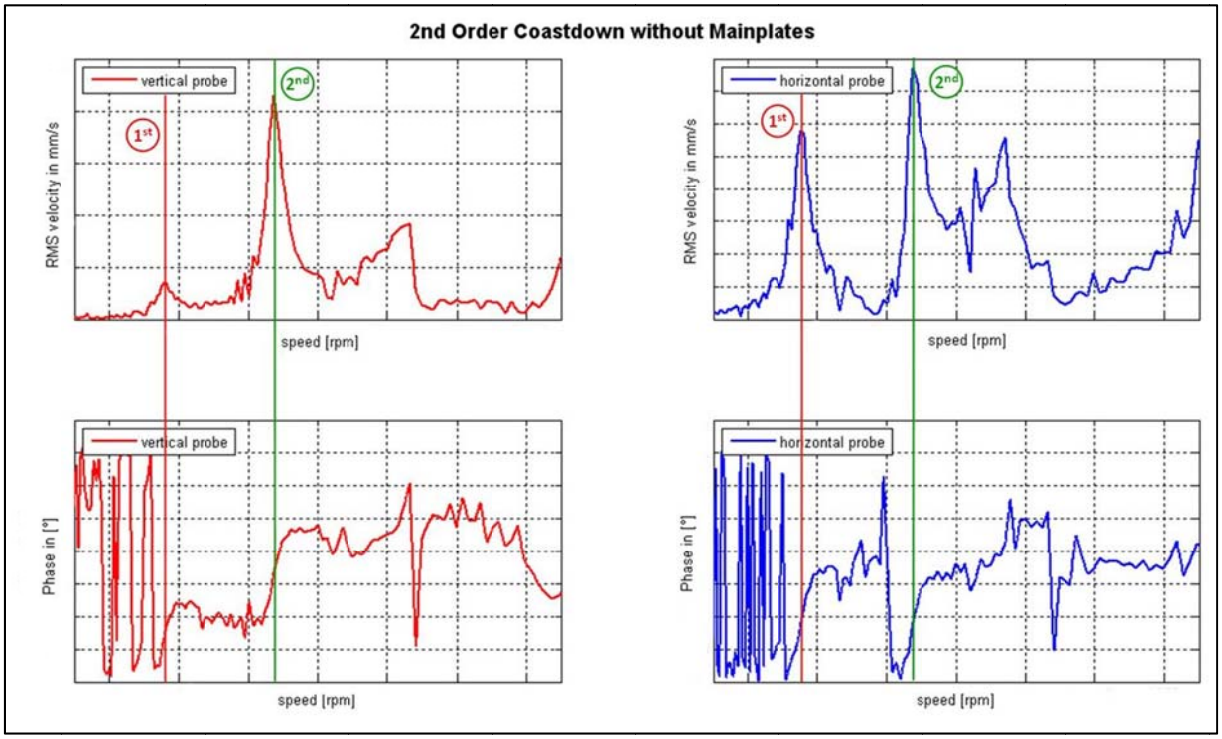

Figure 7.13: 2nd order trace of coastdown without main plates

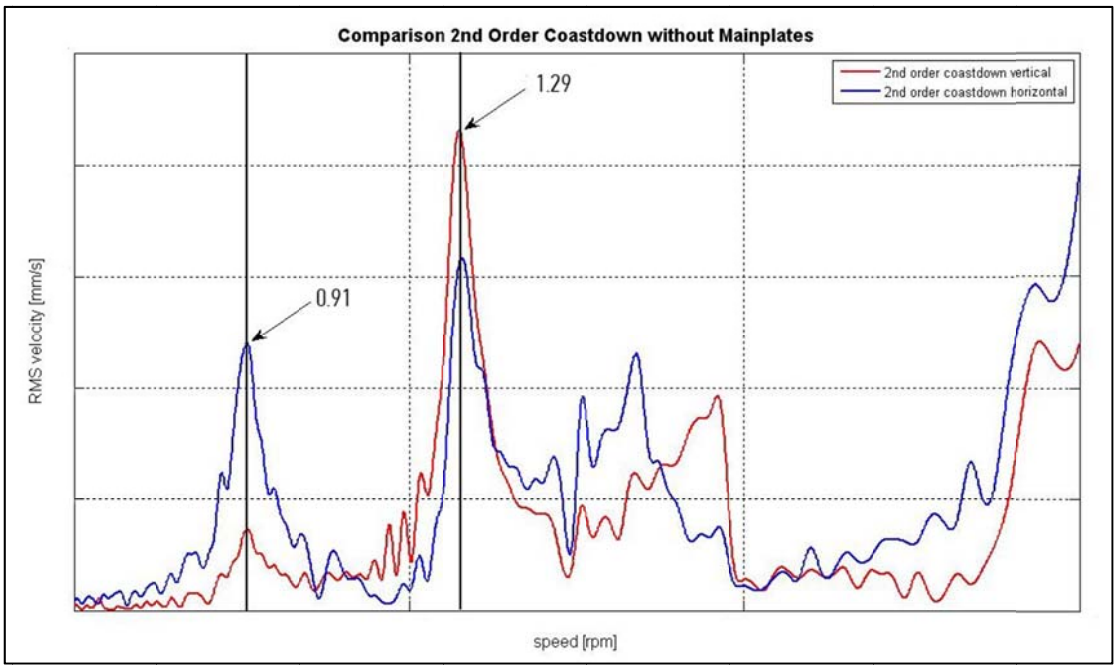

Figure 7.14: Comparison of vertical and horizontal amplitudes for 2nd order trace

The comparison of the horizontal and vertical vibrations (see Figure 7.14) illustrates a higher horizontal amplitude for the first resonance frequency and a higher vertical amplitude for the second. Regarding Figure 7.10 the first resonance frequency can be interpreted as the eigenfrequency of the 1st mode (horizontal, BW) and the 2nd is the eigenfrequency of the 2nd mode (vertical, FW). Because 2nd order means two times rotational speed, the 2nd order crosses the eigenfrequencies at 1.82 (2x0.91) and 2.59 (2x1.29).

7.2.3 Conclusions of Measurement Analysis

The order analysis of the measurements shows major divergences for the intersections of 1st and 2nd order with the first mode pair as compared to the results of the MBS model (Table 7-6).

		MBS model	Measurement	Error
1st order	Intersection 1st mode (horizontal, BW)	2.0	1.77	11.5%
	Intersection 2nd mode (vertical, FW)	3.46	-	-
2nd order	Intersection 1st mode (horizontal, BW)	2.23	1.82	18.34%
	Intersection 2nd mode (vertical, FW)	3.21	2.59	19.44%

Table 7-6: Comparison MBS results to measurements

In order to match the results of the MBS model to the measurement results, the linear substitute stiffnesses have to be adjusted. The best match is obtained with the values listed in Table 7-7.

	Original Stiffness Value [N/m]	Adjusted Stiffness Value [N/m]	Deviation [%]
Feed End Bearing FE_H	3.97 e^8	2.235 e^8	43.7
Feed End Bearing FE_V	1.56 e^9	5.2 e^8	66.66
Drive End Bearing DE_H	1.2 e^9	1.0 e^9	16.67
Drive End Bearing DE_V	2.33 e^9	2.24 e^9	3.86

Table 7-7: Adjusted stiffness values

Figure 7.15 illustrates the results of the frequency analysis with the modified stiffnesses. Due to safety issues it is not possible to run the refiner with a speed close to the excitation of the 1st vertical mode and therefore no measurement data for intersection of 1st order and 1st vertical mode is available. Thus, the analysis of the Campbell diagram projects that the 2nd critical speed is around 2.70.

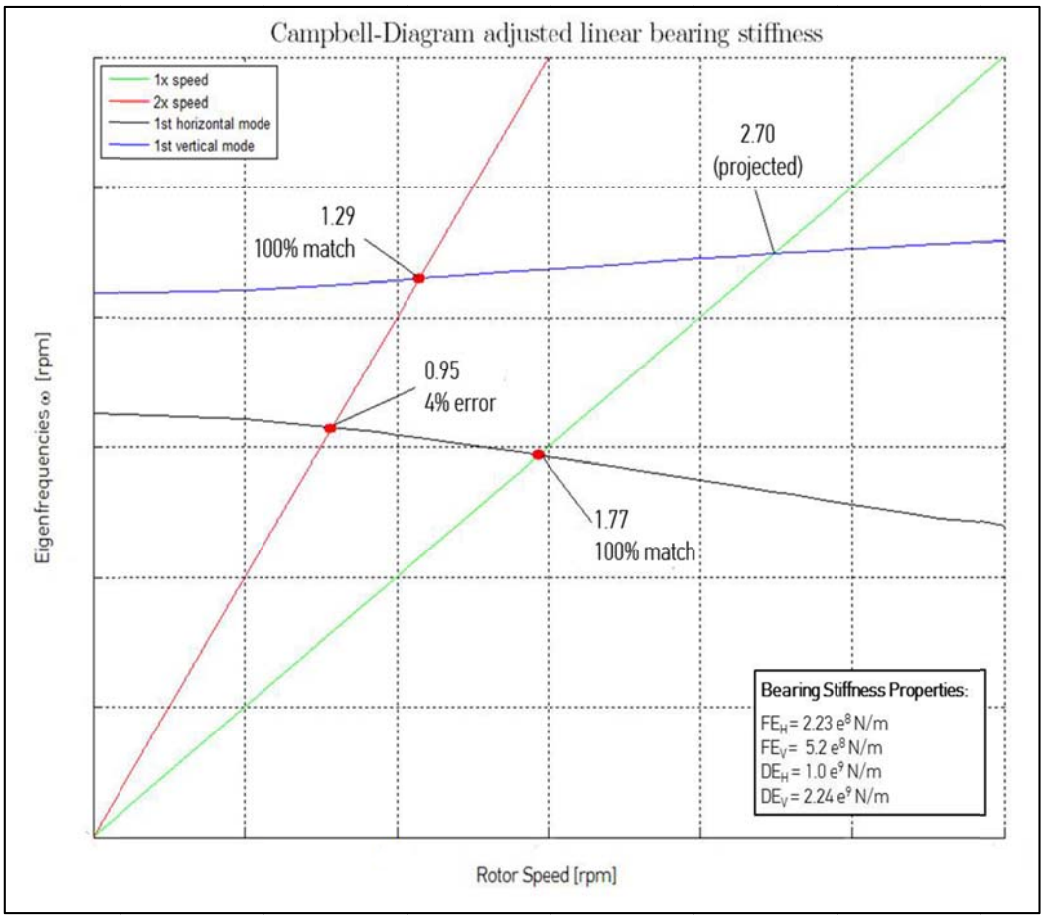

Figure 7.15: Campbell diagram of MBS model with adjusted linear bearing stiffness

Since the deviation in combined bearing stiffness values is unacceptable, the application of using linear substitute stiffnesses must be reconsidered. The major reason why simulation and measurement differ to such a high degree is that the strong nonlinear behavior of the bearings is not included in the computation.

7.3 Simulation with ADAMS Bearing AT

The functional principle of ADAMS Bearing AT is already explained in chapter 5.3. This chapter is aimed to describe the application of the plug-in on the refiner model and to see how the integrated nonlinearities influence the results of the unbalance response in the time domain. As the major impact on the dynamics of the refiner model comes from the stiffness characteristic of the feed end bearing, only the cylindrical roller bearing will be modeled with Bearing AT and the drive end bearing will remain substituted with linear spring stiffnesses.

7.3.1 Modeling of the cylindrical roller bearing

At first, the CAD data of the bearing is downloaded from the bearing manufacturer's homepage. Out of that file, the major geometrical data can be extracted. The manufacturer's know how about specific geometrical parameters as the curvature of the rolling elements is kept secret.

A new roller property file ('.rpf') is created for the cylindrical roller bearing by going to Bearing AT in the menu bar and opening *Bearing AT* → *Roller Bearing* → *Preprocessing* → *Mesh.* Figure 7.16 shows an illustration of the required input parameters in order to build up a finite element mesh of the bearing.

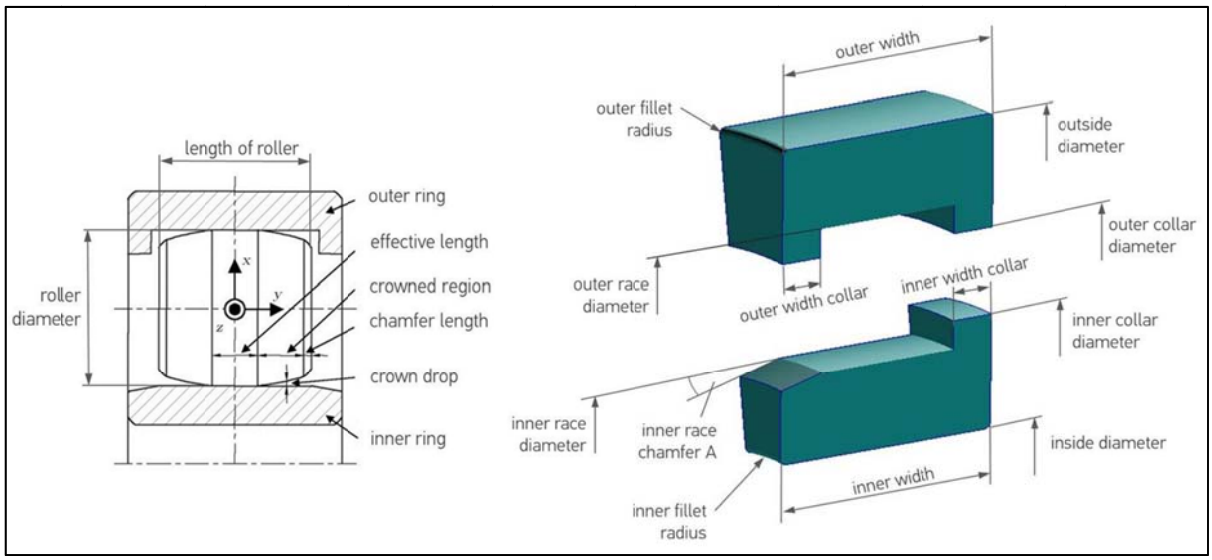

Figure 7.16: Illustration of Bearing AT input parameters for cylindrical roller bearings

The input mask is grouped in four registers: one for the roller element, two for inner and outer ring and the fourth for material data. Table 7-8 summarizes the necessary parameters and emphasizes if they are provided or the data has to be assumed.

	Parameter	Provided by CAD data
Roller Properties	Length of roller	yes
	Effective length	no/assumed
	Chamfer length	yes/uncertain if actual value is used
	Chamfer angle	yes/uncertain if actual value is used
	Roller diameter	yes
	Crown drop	no/assumed
	Number of rollers	yes
Inner Ring Properties	Inside diameter	yes
	Inner race diameter	yes
	Inner collar diameter	yes
	Inner width	yes
	Inner effective length	no/assumed
	Inner width collar	yes
	Inner crown drop	no/assumed
	Inner race chamfer A	yes/uncertain if actual value is used
	Inner fillet radius	yes/uncertain if actual value is used
	Inner contact angle	no/assumed

Outer Ring Properties	Outer collar diameter	yes
	Outer race diameter	yes
	Outside diameter	yes
	Outer width	yes
	Outer width collar	yes
	Outer fillet radius	yes/uncertain if actual value is used
	Outer contact angle	no/assumed
FE – Data	Young's modulus	no/assumed
	Poisson ratio	no/assumed
	Mass density	no/assumed

Table 7-8: Input parameters for cylindrical roller bearings

For the reason of short CPU-times, Bearing AT utilizes symmetry in modeling the contact problem between roller and ring for inner and outer race (see Figure 7.17). The contact angle for inner and outer race defines the size of the contact patch on the roller surface.

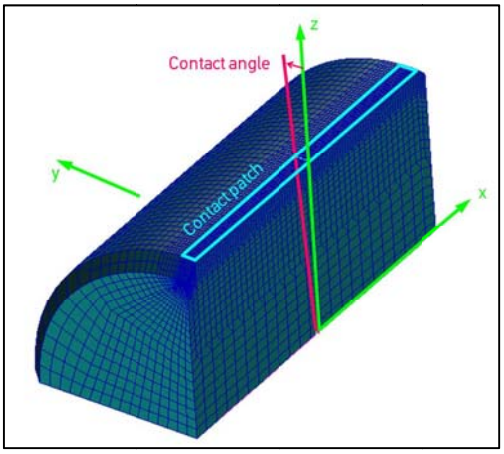

Figure 7.17: FE geometry of roller with defined contact patch

After all inputs are completed, the meshing is activated followed by a NASTRAN analysis.

In the next step, the compliance analysis is started with the selection of *Bearing AT* → *Roller Bearing* → *Preprocessing* → *Contact.* Figure 7.18 shows the input mask for the contact preprocessor and explains the variables for the inner ring with graphical illustrations.

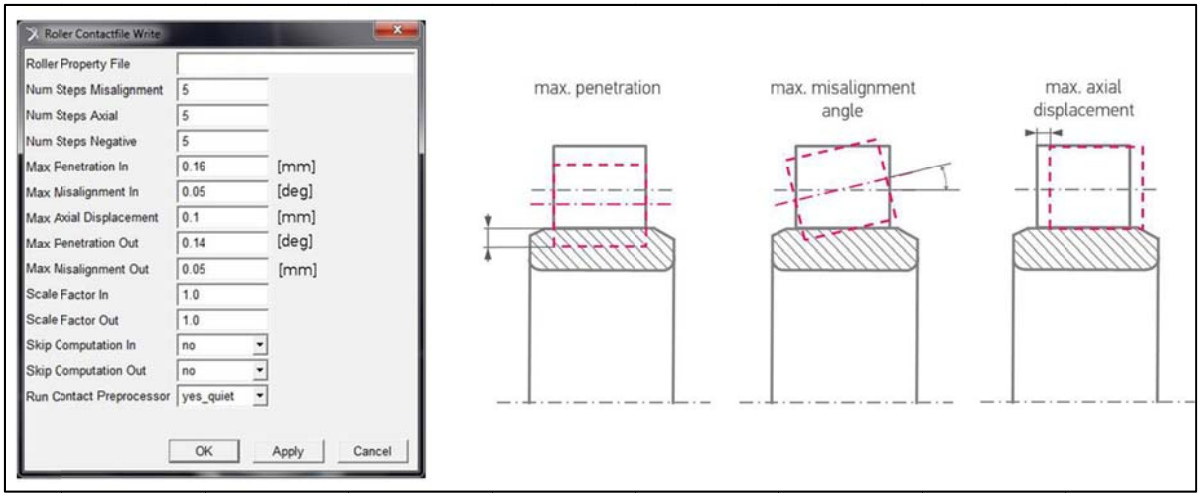

Figure 7.18: Input mask for contact preprocessor with graphical explanation

The contact processor takes the stiffnesses calculated in step 1 into account and builds up contact maps between the roller and the rings, which are used for interpolation in ADAMS. The user inputs a maximum penetration for inner and outer ring, which represents the overlap between the rigid roller and the rigid ring. Unless negative steps are defined, the roller is pushed 20 steps into the ring to the maximum value of penetration. If the roller has a slight misalignment, a contact between roller and ring would already exit at the initial step. So as to ensure that the calculation starts without contact, it is possible to define a virtual clearance by setting negative steps. In case of the examined bearing five negative steps are defined, leaving a total penetration of 25 steps in vertical direction. Furthermore, a maximum misalignment angle can be defined. As noted in the input mask in Figure 7.18, the contact maps for the misalignment are calculated in five steps. Consequently a misalignment angle of 0.05° means that all 25 vertical contact calculations are carried out for a misalignment of -0.05°, -0.025°, 0°, 0.025° and 0.05°. The same is valid for the maximum axial displacement of 0.01 mm. All 125 contact calculations are also performed for an axial displacement of -0.1 mm, -0.05 mm, 0 mm, 0.05 mm and 0.1mm. The compliance analysis for the outer and inner ring is in principle identical and the resulting contact

forces are stored in the *.rif file for the inner ring and the *.rof file for the outer ring. The "scale factor" for the inner and outer race corrects the computed contact force by their respective values. The option "yes" for "run contact preprocessor" ensures that the entire progress is reported on screen. All displayed output is stored in a *.log file. The contents of the log-file or the display of the compliance should be reviewed, because it allows validation of the selected definitions for the contact angles and for the penetration. The compliance analysis displays the contact map for each load step and the computed resulting contact forces.

```
... processing load step  6 =  0.00780 for beta =   5.0

    6  NXXXXXXXXXXXXXXXXXXXXXXX
    5  NXXXXXXXXXXXXXXXXXXXXXXX
    4  NXXXXXXXXXX---XXXXXXXXXX
    3  NXXXXXX-----------XXXXXXX
    2  NXXXXX-------------XXXXXX
    1  NXXXXX-------------XXXXXX

... processing load step  7 =  0.00910 for beta =   5.0

    6  NXXXXXXXXXXXXXXXXXXXXXXX
    5  NXXXXXXXXXXXXXXXXXXXXXXX
    4  NXXXXXXXX-------XXXXXXXXX
    3  NXXXXXX-----------XXXXXX
    2  NXXXX--------------XXXXX
    1  NXXXX--------------XXXXX
```

Figure 7.19: Contact map

The contact map in Figure 7.19 shows the state of grids in the contact patch, where "X" means no contact, "-" means contact and "N" indicates that contact of the roller falls outside the race surface.

When the maximum penetration is reached, the contact processor reports the resulting forces and their curve-fitted values. At the end of all contact computations, the *rif and *rof files are created for use by ADAMS.

As soon as the previous modeling steps are completed successfully, the roller bearing element can be integrated in ADAMS. Thus, a rigid shaft part is needed on which the roller bearing is acting. Although a flexible shaft already exists it is

necessary to build a massless, rigid dummy shaft for the roller bearing. The center marker of that part has to be aligned according to the bearings coordinate system to assure a correct position. This means the z-axis of the center marker (CM) has to point in the direction of the rotating axis. Additionally, the CM is aligned concurrent to the feed end interface node. After preparing the model for the implementation, the user has to open: *Bearing AT* → *Roller Bearing* → *Element* → *New.*

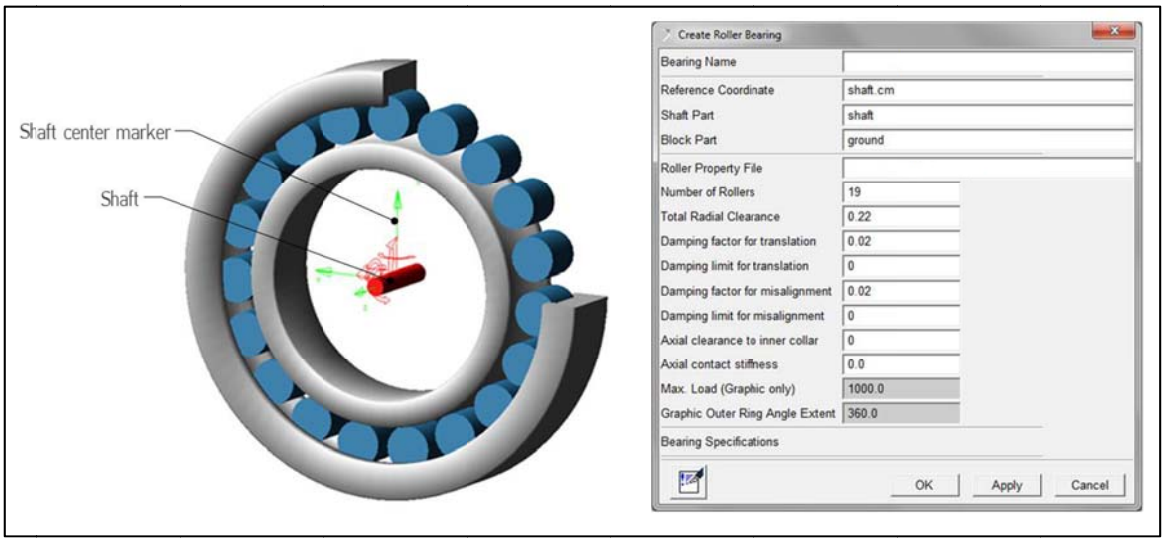

Figure 7.20: Implementing the cylindrical roller bearing in ADAMS

Bearing AT allows the user now to define name, reference frame, shaft part and block part. Temporarily ground will be set as block part because a supplementary model of the frame will be added later, which takes the linear frame stiffness into account. Next, the created roller property file is specified and all afore calculated and defined values are assigned to the bearing. Now it is possible to adjust the number of rollers compared to the preprocessing input and to add the total radial clearance. In case of the implemented bearing a C3 clearance is defined, which is around 220 µm. Damping is considered with a 2% factor and set for translation as well as misalignment. All entered values for the creation of the cylindrical roller bearing are displayed in Figure 7.20.

7.3.2 Integration of Supplementary Frame Model

Through the direct attachment of the bearing to ground, vertical and horizontal stiffness are much higher when compared to the model with linear substitute stiffnesses (chapter 7.1). Hence, the frame stiffness has to be considered in the model. This can be achieved by creating an auxiliary body in form of a circular ring around the bearing and joining it to ground with linear springs (Figure 7.21). Whereat the springs get the linear frame stiffness assigned and the new part functions as block part for the bearing. Since only lateral movements of the block part are allowed, the translational DOF in direction of the rotation axis as well as all rotational DOFs are constrained by applying a point motion to the part's center marker.

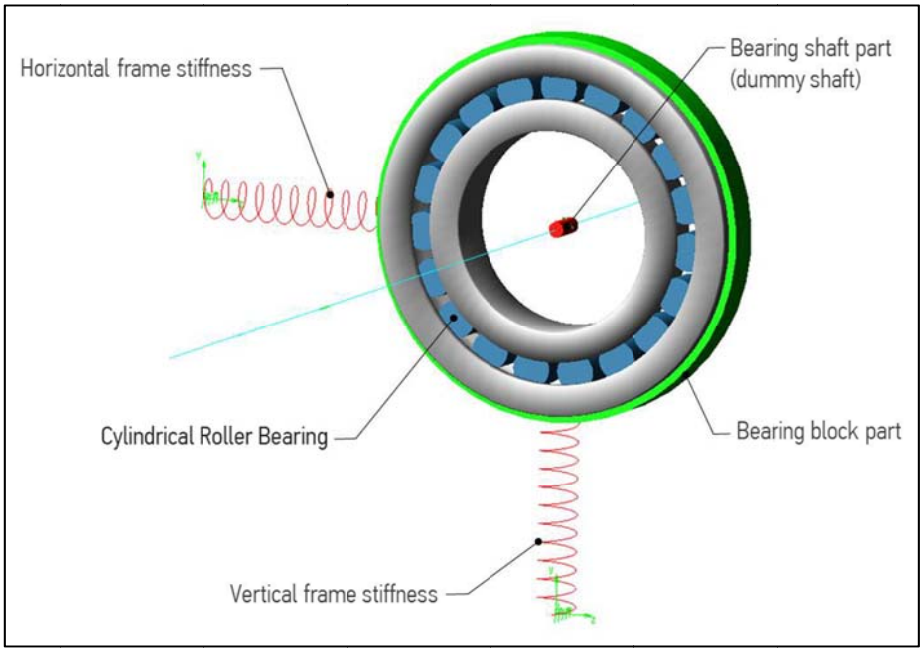

Figure 7.21: Supplementary frame model

7.3.3 Run-up Simulations with integrated Cylindrical Roller Bearing

Figure 7.22 shows the final MBS model in which the cylindrical is implemented and the linear frame stiffness is considered.

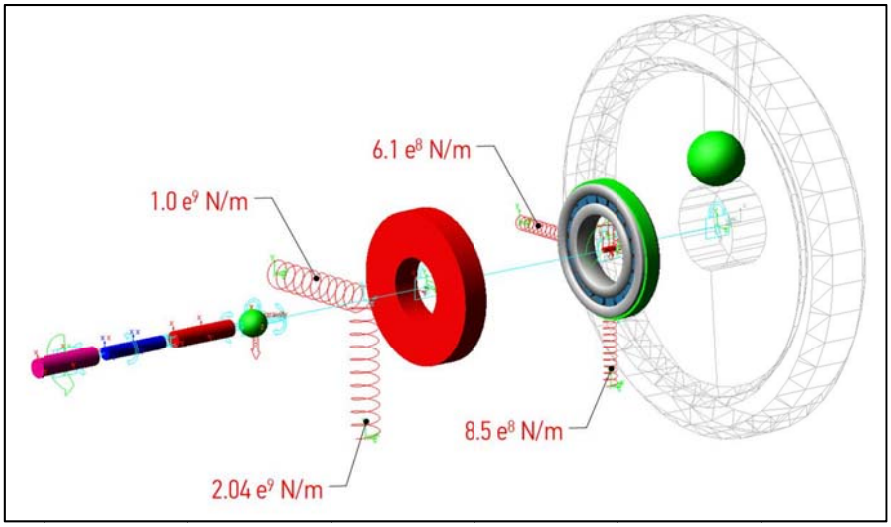

Figure 7.22: Final MBS model of the refiner with the cylindrical roller bearing

By performing the same run-up simulation as described in chapter 7.1.2 with the identical settings for the flexible shaft, DE-bearing and the unbalance, ADAMS computes the following unbalance response plot:

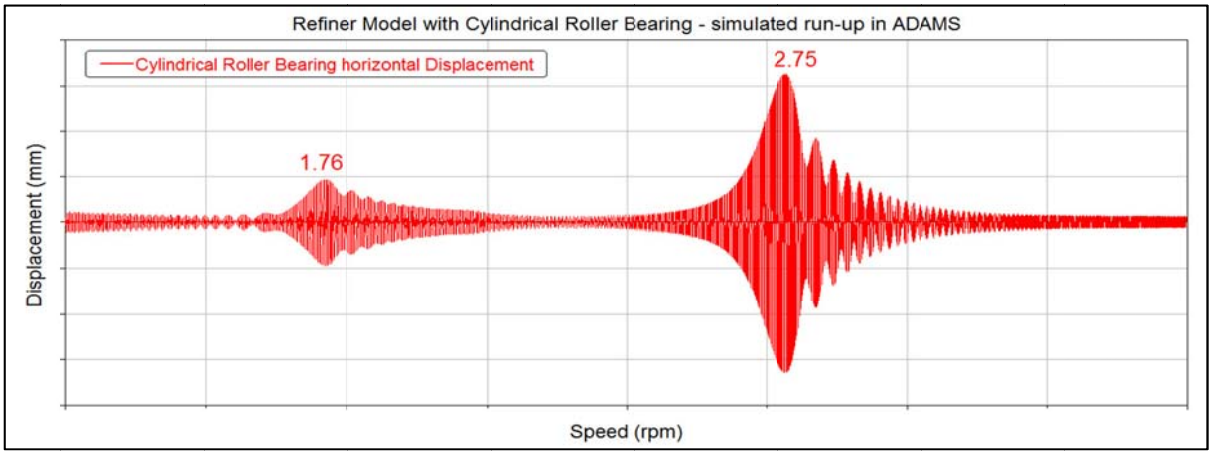

Figure 7.23: Unbalance response plot of final MBS model

	1st critical speed	2nd critical speed
Measurement results (Figure 7.15)	1.77	2.7 (projected)
Model with cylindrical roller bearing	1.76	2.75
Deviation	**0.62 %**	**1.7 %**

Table 7-9: Comparison of critical speeds with adjusted frame stiffness

The run-up simulation indicates clearly two regions of peak resonances (

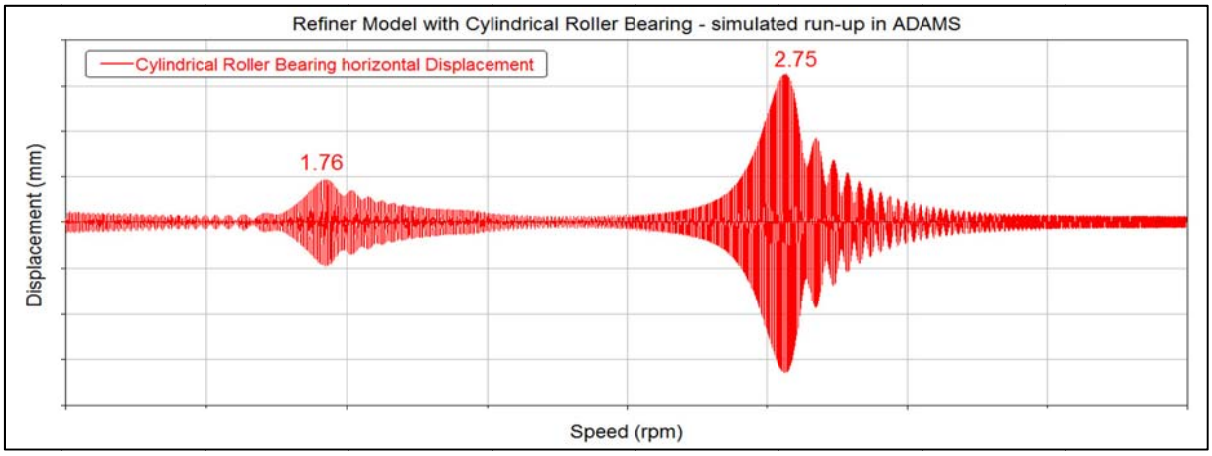

Figure 7.23), the first one at 1.76 and the second at 2.7. A comparison of the acquired results with the measurement data reveals very little deviation. As Table 7-9 shows, the 1st critical speed only differs to 0.62 % and the 2nd critical speed to 1.7%. A notable weakness of this comparison is that the 2nd critical speed from the measurements results is actually a projected value, obtained by computation with adjusted linear substitute stiffnesses. These findings implicate that the nonlinear stiffness characteristic of the cylindrical roller bearing is very well implemented through ADAMS Bearing AT.

8 Summary

The purpose of the research was to determine the effect of nonlinear stiffness distribution and clearance in roller bearings on the dynamic behavior of rotating machinery. In the course of the research two different simulation approaches were deployed to compute the natural frequencies and critical speeds of an Andritz refiner. Furthermore, vibration measurements were carried out on the machine to evaluate the simulation results.

As the modal FEA is the usual method of choice at Andritz, it was used first to investigate the refiner's rotating unit in the frequency domain. Therefore the bearing behavior was linearized with substitute stiffness values provided by the bearing manufacturer. The subsequent comparison of the resulting critical speeds and the resonance frequencies identified by an order analysis of the measurements revealed a significant deviation. As a consequence, the rotor-bearing assembly was modeled in the multibody simulation environment MSC/ADAMS. A model test with the same linear substitute stiffness applied instead of the bearings leaded to the same results as the FE-computation. The main reason for choosing the MBS as second simulation approach was the application and assessment of the newly developed bearing subroutine Bearing AT. This new feature enabled a complete modeling of the complex contact mechanics of the refiner's feed end bearing, which has the most impact on the systems' natural frequencies. By performing a run-up simulation in the time domain, the results from the measurements could be matched.

9 Conclusion

The critical speeds identified with ADAMS using the Bearing AT plug-in enhance the understanding of the impact of bearing nonlinearities on simulation results. Taken together, the results of the transient run-up simulations suggest that it is possible to project the excitation speeds of natural frequencies through an unbalance response analysis in the time domain because acquired measurement results were matched with the performed computations. Arguably, the utilization of a projected 2nd critical speed adds uncertainty to the comparison of measurement and simulation. Nevertheless, the fact that the correctly modeled nonlinear bearing contact maps as well as the integrated clearance lead to significant lower critical speeds as in the FE-simulation with substitute stiffnesses, and actually comply with test-run data, provides confidence in the new simulation technique. Comparing the modeling effort between the currently used rotordynamic analysis in ANSYS and the MBS approaches in ADAMS it obviously can be said that modeling and simulation in ADAMS is more time consuming.

Finally, two limitations to this pilot study need to be acknowledged. Firstly, the referenced measurement points were only attained by using order traces. For the elimination of this weakness the testing of the machinery should be performed again with an order analysis. The results in form of a color map and a waterfall plot would be a better confirmation, whether or not the simulation results are from good quality. Secondly, the new simulation results were only verified for one machine. In order to gain further confidence in the MBS simulation procedure, comparisons between measurement and simulation data of at least one additional refiner is necessary. It is strongly recommended that the impact of these factors is considered in future studies.

10 List of Figures

11 List of Tables

12 Bibliography

[1] Gasch, R., Nordmann, R. & Pfützner, H. (2006). *Rotordynamik*, 2nd ed. Berlin, Heidlberg, New York: Springer-Verlag.

[2] Genta, G. (2005). *Dynamics of Rotating Systems*. Torino, Italy: Springer-Verlag,.

[3] Krämer, E. (1993). *Dynamics of Rotors and Foundations*. Berlin: Springer-Verlag.

[4] Swanson, E., Powell, C.D. & Weissman, S. (2006). A practical review of rotating machinery critical speed and modes. *Sound and Vibration*, pp. 10 - 17.

[5] Nelson, F.C. (2007). Rotor Dynamics without Equations. *International Journal of COMADEM*, pp. 2-10.

[6] Ostermann, B. (2010) *Modeling Of High-Speed Refiner Rotors*. Bachelor Thesis.

[7] Kugler, S. (2010). *Das Prinzip der Virtuellen Arbeit und seine Anwendung in der Finiten Elemente Methode.* Ergänzungsskirptum für Mechanik II.

[8] McConville, J.B. & McGrath, J.F. (1998). *Introduction to ADAMS Theory*. MDI Report.

[9] Fotiu, P.A. (2009). *Mehrkörperkinetik*. Skriptum zur Vorlesung, FHWN.

[10] Wolauschegg, S. (2001). *Hybrides Fahrzeugmodell mit Kopplung von Mehrkörpersystem-Fahrwerk und Finite-Elemente-Karosserie zur Beschreibung des Phänomens "Zittern"*. Dipolomarbeit, TU Graz.

[11] Sopanen, J. (2004). *Studies of Rotor Dynamics using a Multibody Simulation Approach*. Phd. Thesis, Lappeenranta University of Technology.

[12] Harris, T.A. & Kotzalas, M.N. (2001). *Rolling Bearing Analysis*, 4th ed.: Wiley.

[13] Tiwari, M., Gupta, K. & Prakash, O. (2000). *Dynamic Response of an Unbalanced Rotor Supported on Ball Bearings.* Journal of Sound and Vibration, 238, p. 757-779.

[14] Tiwari, M., Gupta, K. & Prakash, O. (2000). *Effect of Radial Internal Clearance of a Ball Bearing on the Dynamics of a Balanced Horizontal Rotor.* Jornal of Sound and Vibration, 238, p. 723-756.

[15] Kappaganthu, K. & Nataraj C. (2011). *Nonlinear modeling and analysis of a rolling element bearing with a clearance.* Department of Mechanical Engineering, Villanova University, USA.

[16] Mourad, D., Titouche, N.E., Djaoui, M. & Mohammed, O. (2008). *The Calculation of Ball Bearing Nonlinear Stiffness Theoretical and Experimental Study with Comparisons.* Journal of Engineering and Applied Sciences.

[17] Fritz, F., Basler, A. & Seemann, W. (2009). *Simulation of High-Speed Ball Bearings with MSC/ADAMS.* PAMM Proc. Appl. Math. Mech. 9, p. 115-116.

[18] Hamrock, B.J. & Anderson, W.J. (1983). *Rolling-element bearings.* NASA reference publication; 1105.

[19] Kolerus, J. & Wassermann, J. (2008). *Zustandsüberwachung von Maschinen.* Renningen: Expert Verlag.

[20] Hochrainer, M. (2010) *Modale Analyse, Modales Testen.* Skriptum zur Vorlesung, FHWN.

[21] Felippa, C.A. (2004). *Introduction to Finite Element Methods.* Lecture Notes, University of Colorado.

[22] Schönborn, K. (2011). *Rotordynamische Analysen mit ANSYS.* CAD FEM Information.

[23] Uchtmann, K. & Wirth, R. (1999). Maschinendiagnose an drehazhlveränderlichen Antrieben mittels Ordnungsanalyse. *Antriebstechnik*, no. 5, pp. 44-49.

Appendix

Matlab Code for Analytical Solution of the simple Overhung Rotor:

```
%%%%%%%%%%%%%%%%%%%%  Parameters  %%%%%%%%%%%%%%%%%%%%
% Material Data
E=210e9;                  %Pa
v=0.3;
roh=7850;                 %kg/m^3

% Shaft
ls=1.50;                  %m
ds=0.1;                   %m
I=(ds/2)^4*pi*0.25;       %m^4

% Rotor
dr=1;                     %m
hr=0.1;                   %m
mr=(dr/2)^2*pi*hr*roh;    %kg

% Bearing Positions
l=1;                      %m
c=0.5;                    %m

%%%%%%%%%%%%%%%%%  Inertias and Stiffnesses  %%%%%%%%%%
Jp=0.5*mr*(dr/2)^2;               %kgm^2
Ja=1/12*mr*(3*(dr/2)^2+hr^2);     %kgm^2

k11=12*E*I*(l+3*c)/(c^3*(4*l+3*c));             %N/m
k12=-6*E*I*(2*l+3*c)/(c^2*(4*l+3*c)); % =k21    %N/m
k22=12*E*I*(l+c)/(c*(4*l+3*c));                 %N/m

%%%%%%%%%%%%%%%%%%%%  Solving the DAE  %%%%%%%%%%%%%%%%

W=0:10:3000;   %Vector of shaft speeds in rpm
W=W*2*pi/60;

for i=1:length(W)
     syms w;
     eigenfreq(i,:)=solve(mr*Ja*w^4-mr*Jp*W(i)*w^3-(k22*mr+k11*Ja)*w^2 ...
     +k11*Jp*W(i)*w+(k11*k22-k12^2),'w');
end

%%%%%%%%%%%%%%%%%%%%%%%%  Plot  %%%%%%%%%%%%%%%%%%%%%%%%

speed=W*30/pi;

figure
hold on
title('Comparison of Eigenfrequency Analyses','FontWeight','bold');
plot(speed,speed/60,'g');
plot(speed,abs(eigenfreq(:,1))/(2*pi),'b')
plot(speed,abs(eigenfreq(:,2))/(2*pi),'b')
plot(speed,abs(eigenfreq(:,3))/(2*pi),'b')
plot(speed,abs(eigenfreq(:,4))/(2*pi),'b')
grid on
xlabel('Rotor Speed [rpm]')
ylabel('Eigenfrequencies \omega  [Hz]')
axis([0 3000 0 150]);
hold off
```

Code for Rotordynamic Modal Analysis in ANSYS Classic:

```
!############ Modal Analysis (Omega Steps) ############
/solu
antype,modal          !modal analysis
modes = 6             !request 6 modes
steps = 50
omega_max = 3000*3.14159/30

modopt,qrdamp,modes,,,on    !Use the QRDAMP eigensolver and specify complex eigensolutions
coriolis,on,,,on            !Stationary Reference Frame is activated

!############ calc ############
*do,i,1,steps
       n = (i-1)*(omega_max/(steps-1))
       omega,n,,,0
       mxpand,6,,,on
       solve
*enddo
finish

!############ Plot Campbell Diagram ############
/post1
plcamp,on,1,rpm,1
```

Code for Unbalance Response Analysis in ANSYS Classic:

```
!############ Harmonic Analysis (Unbalance Response) ############
/SOLU
antype,harmic
omega,0
synchro,,ROTOR
nsubst,500
harfrq,,50          !implicitly defines OMEGA for Coriolis calculation
kbc,1
dmprat,0.1
cmomega,ROTOR,100
coriolis,on,,,on    !Stationary Reference Frame is activated
solve
fini

!############ Unbalance Response Plot ############
! output: amplitude at front end bearing as a function of the frequency
/POST26
nsol,2,2,U,Y,UY
nsol,3,2,U,Z,UZ
realvar,4,2,,,UYR
realvar,5,3,,,UZR
prod,6,4,4,,UYR_2
prod,7,5,5,,UZR_2
add,8,6,7,,UYR_2+UZR_2
sqrt,9,8,,,AMPL1
plvar,9
fini
```